Quantitative Imaging of Protein and Lipid Metabolism using Stimulated Raman Scattering Microscopy

Xi Xu

A dissertation

submitted in partial fulfillment of the

requirements for the degree of

Doctor of Philosophy

University of Washington

2024

Reading Committee:

Dan Fu, Chair

Joshua Charles Vaughan

Albert Folch

Program Authorized to Offer Degree:

Chemistry

University of Washington

Abstract

Quantitative Imaging of Protein and Lipid Metabolism using Stimulated Raman Scattering Microscopy

Xi Xu

Chair of the Supervisory Committee:
Dan Fu
Department of Chemistry

Protein and lipid metabolisms play critical roles in cellular function, and their dysregulation is associated with a range of diseases. Novel techniques for visualizing and quantifying protein and lipid metabolic activities can provide valuable insights into their underlying mechanisms. Stimulated Raman scattering (SRS) microscopy is a powerful label-free quantitative optical technique that enables the mapping of molecular distributions in inhomogeneous biological specimens, such as cells and tissues, by probing their intrinsic vibrational frequencies.

This dissertation presents advancements in implementing multi-channel SRS microscopy and its applications for quantifying several cellular activities related to protein and lipid metabolism. Specifically, it describes accurate measurements of single-cell growth rates and drug uptake in both two-dimensional and three-dimensional cell environments, classification of lipid

molecules in tissues affected by nonalcoholic fatty liver disease, and detection of oxidation products of polyunsaturated fatty acids during lipid peroxidation-induced cell ferroptosis.

These advancements in SRS microscopy offer significant potential for understanding the complex mechanisms that regulate protein and lipid metabolic activities and developing targeted treatments for various diseases.

TABLE OF CONTENTS

LIST OF FIGURES

LIST OF TABLES

ACKNOWLEDGEMENTS

The first time I stood in the laser room, Dan was showing me the lab. I looked at Bryce and Elena working intently at the table, their hands moving with a quiet confidence among all the shiny and mystical optics. I had no clue what anything was, yet had a feeling that I could see myself there, becoming one of them.

The next morning, I came back. It was 8 a.m., and I was excited but barely awake, fumbling through drawers for something Ben had asked me to find—a post, not knowing what a post was. What followed was a journey of learning and growth, made possible by the tremendous mentorship, support, and encouragement from Dr. Dan Fu, Dr. Andy Hill, Dr. Ben Figueroa, Dr. Andrew Francis, Dr. Bryce Manifold, and Elena Thomas. They not only taught me science but shaped the scientist I've become.

This journey has been long, but not nearly long enough to fully express my gratitude. I had countless good stories and memories during my days and nights in the lab and offices, surrounded by close friends that I love and feel grateful for.

I was incredibly fortunate to have Dan as my PI. There are too many things to thank him for: the early days when he walked me step by step through OPO alignment and troubleshooting, the Zoom calls during quarantine where he patiently guided me to use the electronics, and the brainstorming sessions whenever I was stuck with my projects. Most of all, I thank him for being a friend I could talk to when I felt separated and dissociated from my family as an international student. Dan's determination and passion for science are something I hope to carry with me in my future career.

To the best Fu Tang Clan, you have my full gratitude and love. Ben Figueroa, toast to our adventures in both U Village and San Francisco that lightened even the most challenging days. Bryce and Allison Manifold, you always have the perfect wine for every occasion. Rachel Hu, your sweet notes and encouragement meant more than words can say. Erin Dunnington, Emily Rathbone, and Zach Ellsworth, the OG members of the most exclusive Lab Gorls club, thank you for your endless love and companionship despite my dreadful contribution to the trivial nights. Chisa Zensho, your amazing laughter always lightens my heart, and I enjoy our ride home together. Jon Kim and Gordon “Chicken” Chiu, thank you for our happy memories during the Chicago trip. Harrison Hu, for your “incredibly incredible” jokes. Thomas Ro, I miss you singing Phantom of the Opera in the lab while turning my glass rods. To Ryan Owens and Ulises Perez for our friendships and delightful memories in the bars. And to Brian Wong, Rawbert Espinoza, and Sarah Ransom, thank you for the fun times and conversations in the lab.

I joked that I was the most unattached person on this side of the Earth. But it was never true. I have friends who became family here in Seattle. Abby Jiang, my sweetest roommate, thank you for your companionship and our heartfelt conversations. Faye Teng, Shuo Wang, Allen Yang, Jillian Zhao, Jack Zhang, Henry Qian, Weidi Tang, and Min Pan, you have been my closest family here. Bobby Wan, Jasmine Zhou, Jiaying Yang, and Jerry Ji, thank you for the dinners, skiing trips, and laughter-filled days. Coco Zhu, for our wonderful times in San Diego and at Tig.

To my committee members, Dr. Joshua Vaughan, Dr. Albert Folch, Dr. Sarah Keller, and Dr. Dustin Maly, your support, suggestions, and constructive feedback shaped not only my work but my growth as a scientist.

I am deeply grateful to my collaborators, without whom some of my projects would not have taken flight. Dr. George Ioannou, Sr. Sum Lee, and Christopher Savard, your expertise in the

NAFLD, as well as your professional curiosity and perseverance, inspired me. Dr. Libin Xu, Noelle Reimers, and Angela Guo, thank you for your insights and passion for the lipid peroxidation project. I am excited to see the future of this project.

Lastly, and most importantly, I thank my parents, Yaqing Li and Zhenghai Xu, and my brilliant friend, Yue Liu, for being my biggest supporters and unwavering foundation at home. Your love and belief in me made me the luckiest person.

CHAPTER 1. INTRODUCTION

1.1 BASICS OF PROTEIN AND LIPID METABOLISMS

Protein and lipid metabolisms are fundamental to the functioning of cells, playing essential roles in their structural integrity[1], energy production[2], growth and proliferation[3,4], and various signaling pathways[5–7]. Proteins are large, complex molecules that serve as the building blocks for cellular structures, enzymes, and signaling molecules.[8] These molecules are composed of amino acids, which are linked together by peptide bonds, forming polypeptide chains that fold into intricate three-dimensional structures. Protein metabolism can be divided into two processes: protein synthesis (anabolism) and protein degradation (catabolism). Protein synthesis is the process of assembling amino acids into polypeptides directed by the genetic information encoded in messenger RNA (mRNA). This process is tightly regulated and occurs in the ribosomes, consuming energy in the form of adenosine triphosphate (ATP).[9] On the other hand, protein degradation involves the breakdown of polypeptides into individual amino acids, during which energy is released and can be reused.[10]

Lipids are another major class of biomolecules that are crucial for cellular function. They are involved in forming cell membranes, storing energy, and acting as signaling molecules.[1,11,12] Lipid metabolism is divided into lipid synthesis (lipogenesis) and lipid breakdown (lipolysis).[13,14] Lipogenesis includes the synthesis of fatty acids and their subsequent conversion into triglycerides, which are stored in adipose tissue as an energy reserve.[13] Lipolysis is the process during which triglycerides in cell lipid droplets are hydrolyzed into free fatty acids and glycerol, which can then be utilized for energy production through beta-oxidation.[15]

Dysregulation in these protein and lipid metabolic processes is associated with the onset and progression of a wide range of diseases, including cancer, metabolic syndromes such as obesity and diabetes, and neurodegenerative disorders like Alzheimer's and Parkinson's disease.[16–19] For instance, dysregulated protein synthesis and degradation can lead to the pathology of various diseases and are tightly coupled with tumor growth and resistance to chemotherapy.[20–24] Similarly, altered lipid metabolism can lead to excessive lipid accumulation in tissues, contributing to conditions like nonalcoholic fatty liver disease (NAFLD) and atherosclerosis.[25–28] Understanding the underlying mechanisms of protein and lipid metabolisms and how their regulation is altered in pathological conditions can provide essential insights into disease progression and facilitate the development of targeted therapeutics.

Researchers have employed various techniques to investigate and quantify protein and lipid metabolism, each with its advantages and limitations. One of the most commonly used methods is mass spectrometry (MS)-based metabolomics, which allows for the identification and analysis of a wide range of metabolites.[29–31] MS provides highly sensitive and accurate measurements of proteins and lipids, but it often requires extensive sample preparation, including extraction and purification, which can disrupt the native state of biological samples. Additionally, conventional MS techniques are destructive, meaning that the sample cannot be reused for further analysis. Another major limitation is the lack of spatial information, making it difficult to determine the localization of metabolites within cells or tissues.[30] To address this challenge, mass spectrometry imaging (MSI) has been developed, which provides spatial information with less extensive sample preparation.[32] The typical spatial resolution of MSI ranges from approximately 5 to 200 micrometers, depending on the specific technique used.[32,33] For instance, Matrix-Assisted Laser Desorption/Ionization (MALDI) typically achieves a resolution of around 10-50 micrometers, while secondary ion mass spectrometry (SIMS) can achieve finer resolutions, down to 1-5 micrometers.[34–36] Despite these improvements, the spatial resolution is often not sufficient for detailed subcellular localization of metabolites, especially in heterogeneous biological samples where finer spatial resolution is crucial for understanding metabolic dynamics.[37,38]

Fluorescence microscopy is another widely used technique for studying protein and lipid metabolism.[39–42] Various fluorescent probes have been designed to bind to specific proteins or lipids of interest, enabling their visualization in live cells.[43–45] This technique provides high spatial resolution and allows for real-time imaging of metabolic processes. However, fluorescence microscopy has several limitations, notably the need for exogenous labels, which can interfere with normal cellular function, and photobleaching, which limits the duration of imaging. Moreover, not all metabolites can be labeled effectively, and the labeling process may alter the biochemical properties of the molecules of interest.[46]

Nuclear magnetic resonance (NMR) spectroscopy is a nondestructive technique for studying protein and lipid metabolism in intact tissues.[47–49] NMR provides detailed information about the chemical structure of metabolites and can be used to monitor metabolic changes over time in vivo.[50] However, NMR has relatively low sensitivity compared to other techniques, such as MS, which limits its capability to detect low-abundance metabolites.[51] Additionally, NMR requires large sample volumes and, therefore, is less suitable for studying small or heterogeneous biological samples.[52]

Isotope labeling is another approach frequently used to study metabolic pathways.[53,54] By incorporating stable isotopes, such as carbon-13 (^{13}C), nitrogen-15 (^{15}N), or deuterium (D), into metabolic precursors, researchers can trace the incorporation of labeled atoms into downstream metabolites and gain insights into fluxes in specific metabolic pathways.[55–57] Isotope labeling is often combined with MS or NMR to detect labeled metabolites.[58–61] Although this technique yields valuable information on metabolic pathways, it is often complex and time-consuming, requiring specialized equipment and technical expertise. Additionally, careful validation is necessary to ensure that introducing labeled precursors does not alter normal metabolic activity, which could potentially influence the results.

Overall, comprehensive visualization and quantification of protein and lipid metabolism at the molecular level remain challenging due to the complexity and heterogeneity of biological systems. Traditional analytical techniques often require extensive sample preparation, lack spatial information, or involve the use of labels that can perturb normal cellular function. Biological tissues are composed of diverse cell types, each with distinct metabolic activities, which makes it difficult to obtain a complete picture of metabolic dynamics using the abovementioned techniques. Therefore, there is a need for advanced imaging methods that can provide label-free, quantitative, and spatially resolved information about protein and lipid metabolism in intact biological samples. In recent years, vibrational spectroscopy-based imaging techniques, notably Raman imaging, have shown tremendous potential for label-free visualization and quantification of different metabolic processes in a wide range of biological models. In the following section, we describe the principles of Raman scattering-based imaging techniques, specifically stimulated Raman scattering (SRS) microscopy.

1.2 RAMAN SCATTERING-BASED IMAGING TECHNIQUES

1.2.1 *Spontaneous Raman Scattering*

Vibrational spectroscopy is a powerful analytical tool that allows for the identification of molecules based on their unique vibrational signatures. When light interacts with a molecule, it may be reflected, absorbed, or scattered. Raman spectroscopy is a form of vibrational spectroscopy that measures inelastically scattered photons. Discovered in 1928, Raman scattering occurs when photons incident on a sample are scattered by molecular vibrations, resulting in either a loss or gain of energy.[62] This energy shift corresponds to a change in the wavelength of scattered light and can provide chemical and structural information about the molecule.

Raman spectroscopy is inherently a label-free, non-destructive, and non-invasive technique, making it ideal for biological analysis.[63] Unlike infrared spectroscopy, which suffers from a strong water absorption cross-section, Raman spectroscopy can be effectively used in aqueous environments such as cells and tissues. The excitation wavelengths used in Raman spectroscopy are typically below 1300 nm, minimizing water absorption and thus enabling the analysis of biological samples without interference.

However, Raman spectroscopy has limitations, particularly its low sensitivity. The typical Raman cross-sections are on the order of 10^{-30}-10^{-23} cm^2, which is several orders of magnitude lower than those of fluorescence or infrared spectroscopy.[64,65] This low sensitivity results in weak signals, long acquisition times, and limited chemical specificity due to background scattering from other molecules. The invention of lasers in the 1960s enabled higher irradiance, improving the practical implementation of Raman spectroscopy by providing higher-intensity light sources for excitation. However, the inherently limited signal of spontaneous Raman scattering still presented challenges, especially for imaging applications in biological systems.

1.2.2 *Coherent Raman Scattering (CRS)*

To overcome these limitations of spontaneous Raman scattering, coherent Raman scattering (CRS) techniques were developed. CRS is the nonlinear analog of spontaneous Raman scattering and relies on the coherent excitation of molecular vibrations, significantly enhancing its signal intensity.[66] As a result, CRS offers faster imaging capabilities and orders-of-magnitude higher sensitivity than spontaneous Raman scattering.

CRS is a third-order process that involves two synchronized laser pulses, referred to as pump and Stokes, with frequencies ω_p and ω_p, respectively. When the frequency difference between these two pulses ($\omega_p - \omega_S$) matches a vibrational frequency (Ω) within the molecule, it induces a vibrational coherence, commonly resulting in two possible Raman scattering outcomes: coherent anti-Stokes Raman scattering (CARS) or stimulated Raman scattering (SRS). Figure 1.1 shows the Jablonski diagrams of CARS and SRS energy transitions.

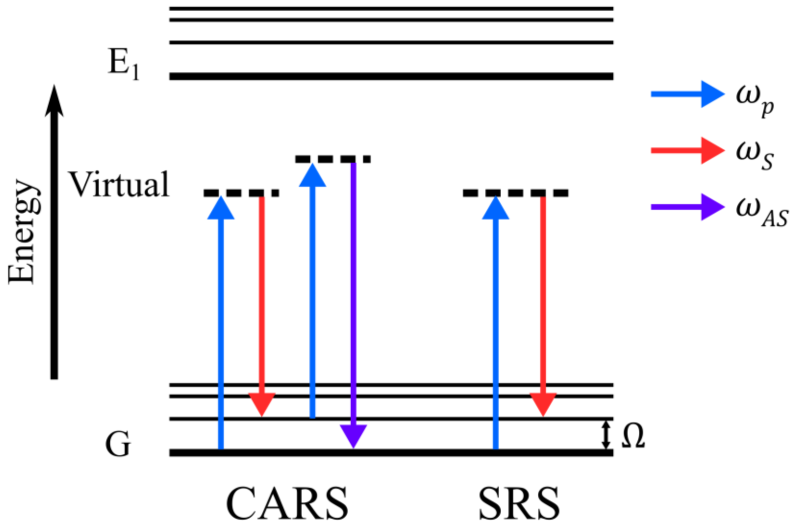

Figure 1.1. Energy level diagram of coherent anti-Stokes Raman scattering (CARS) or stimulated Raman scattering (SRS).

1.2.3 *Coherent Anti-Stokes Raman Scattering (CARS)*

CARS is a four-wave mixing process in which two photons from a pump laser (ω_p) and one photon from a Stokes laser (ω_S) interact with the sample coherently to generate a new photon at a higher energy, called the anti-Stokes photon ($\omega_{AS} = 2\omega_p - \omega_S$).[67] The intensity of the CARS signal depends on the third-order nonlinear susceptibility, which has both a resonant and a non-resonant component. The resonant component corresponds to the molecular vibration being probed, while the non-resonant component arises from other electronic contributions within the sample. The presence of the non-resonant background can interfere with the resonant CARS signal, leading to spectral distortions. Additionally, the CARS signal is quadratic with respect to the concentration of the target molecule, making quantification challenging.[67,68]

1.2.4 *Stimulated Raman Scattering (SRS)*

SRS microscopy, a more recent advancement in CRS, addresses the limitations of CARS and has emerged as a powerful, label-free method for mapping molecular distributions by probing intrinsic vibrational frequencies of biomolecules in cells and tissues. In SRS, when the photon energy difference between the pump and Stokes beams matches the vibrational frequency of a specific molecular bond (Ω), the molecular transition rate is enhanced by stimulated excitation. Unlike CARS, SRS does not generate new photons of a different frequency and is therefore free from the non-resonant background; instead, the intensity of the existing pump and Stokes beams are modulated. Specifically, the coherent excitation of a molecular vibration leads to a loss in the pump beam (stimulated Raman loss, SRL) and a gain in the Stokes beam (stimulated Raman gain, SRG).[69] Mathematically, the SRL (ΔI_p) and SRG (ΔI_S) can be expressed as:

$$\Delta I_p \propto -N\sigma_{Raman} I_p I_S;\ \Delta I_S \propto N\sigma_{Raman} I_p I_S$$

where

- N is the number of molecules in the excitation volume.
- σ_{Raman} is the molecular Raman scattering cross-section of the molecule being probed.
- I_p and I_S are the intensities of the pump and Stokes beams.

These expressions demonstrate that the SRS signal is influenced by factors such as the molecular properties, concentration of the molecules, and characteristics of the excitation beams. These relationships highlight several advantages of SRS, including a strictly linear relationship between signal intensity and sample concentration, making it ideal for quantitative analysis. Additionally, SRS microscopy provides vibrational spectra that are nearly identical to those obtained from spontaneous Raman scattering, with only slight peak broadening due to the laser pulse duration and bandwidth.

Another crucial component of SRS is the modulation transfer method used to detect the SRS signal.[70,71] In typical SRS microscopy setups, the intensity of the pump or Stokes beam is modulated at a high frequency (10-40 MHz), and the resulting modulation in the transmitted or scattered beam is measured using high-frequency phase-sensitive lock-in detection techniques. Lock-in detection allows for the selective measurement of the modulated SRS signal while rejecting unmodulated background noise, significantly enhancing the signal-to-noise ratio and enabling shot-noise-limited sensitivity. This is particularly beneficial when working with biological samples with strong autofluorescence or scattering that can obscure the SRS signal.

Unlike fluorescence-based imaging, which requires labeling with fluorescent dyes or proteins and is limited by photobleaching and phototoxicity, SRS microscopy enables the visualization of endogenous biomolecules without external perturbation. The near-infrared laser sources used in SRS are less likely to cause photodamage compared to ultraviolet or visible lasers, making it a suitable choice for live cell imaging and other biological studies. This label-free capability is particularly advantageous for studying metabolic processes, as it allows researchers to observe real-time dynamics in living cells and tissues without altering their natural state. Furthermore, SRS microscopy offers rapid imaging speeds, making it suitable for capturing dynamic metabolic processes, while providing chemical specificity that allows for the identification of various biomolecules, such as lipids, proteins, and nucleic acids, based on their unique vibrational signatures. Thus, SRS microscopy offers a unique opportunity to study biological processes in their native environment, making it particularly suitable for studying protein and lipid metabolic activities.

1.3 ADVANCEMENTS IN SRS MICROSCOPY FOR METABOLIC STUDIES

SRS microscopy has been widely applied to study both protein and lipid metabolism in cells and tissues, offering valuable insights into various biological environments. In protein metabolism, SRS has enabled direct visualization of protein synthesis and degradation in cancer cells and live tissues, facilitating the study of protein-related biological processes in diverse environments.[72–74]

SRS has also been extensively used to study lipid metabolism, providing crucial insights into cellular and whole-organism metabolic regulation. One major area of focus has been lipid droplet dynamics, where SRS enables real-time visualization and quantitative analysis of lipid storage and mobilization in live cells.[75–81] Furthermore, SRS microscopy allows for detailed analysis of lipid profiles. Specifically, hyperspectral SRS imaging has been used to quantitatively map and trace different lipid species in the Caenorhabditis elegans and mice models, enabling researchers to differentiate between lipid molecules such as triglycerides, cholesterol, and phospholipids.[82–85] These insights into lipid composition under different metabolic conditions are invaluable for understanding lipid metabolism at a molecular level.

In cancer research, SRS has played a significant role in uncovering metabolic alterations associated with cancer progression. For instance, SRS microscopy has revealed that the aberrant accumulation of cholesterol ester in prostate cancer contributes to cancer progression[86], while other studies have demonstrated that pancreatic cancer cells exhibit a significantly higher glucose utilization rate for lipid synthesis than healthy cells[87]. These findings highlight how altered lipid metabolism supports cancer growth and survival, offering potential targets for therapeutic interventions. Additionally, SRS allows researchers to track fatty acid uptake and metabolism in live cells, providing insights into how cells metabolize dietary fats.[88,89] This approach is particularly valuable for studying conditions such as cardiovascular disease and diabetes, where lipid metabolism plays a central role.

Collectively, these diverse applications highlight the potential of SRS microscopy to offer valuable insights into protein and lipid metabolic activities, ranging from subcellular dynamics to whole-organism metabolic regulation. Despite these advancements, several challenges remain that impede the broader application of SRS in metabolic studies. First, the narrower spectral coverage of SRS compared to spontaneous Raman scattering restricts the ability to capture the full vibrational spectrum of complex molecules. Traditional SRS microscopy using picosecond pulses can only probe a single Raman transition at a time, requiring sequential laser wavelength tuning for hyperspectral imaging.[70,90–92] While picosecond laser systems offer excellent spectral resolution, the need for wavelength tuning reduces imaging speed, making it challenging to capture rapid, dynamic metabolic processes in real time. Various approaches, such as spectral focusing, spectral dispersion, modulation multiplexing, and Fourier transform SRS, have been explored to improve imaging speed without sequential tuning[93–98], with spectral focusing being the most commonly adopted due to its ease and robustness of implementation[95–97,99]. However, these methods remain constrained by the modest spectral bandwidth of femtosecond lasers, which is typically around 100-300 cm^{-1}, limiting their ability to differentiate between chemically similar compounds.

Second, accurate quantification in SRS is often hindered by tissue scattering, which can cause substantial signal attenuation and distortion, as well as cross-phase modulation-induced background, which introduces non-resonant artifacts that obscure Raman signals. These issues are particularly pronounced in heterogeneous tissues, where scattering properties vary spatially, making reliable quantification challenging. Ratiometric analysis using hyperspectral information from two separated Raman bands is an effective solution to these problems. By simultaneously capturing information from both resonant and reference bands, ratiometric analysis can correct for variations in scattering, thereby improving quantification accuracy. In addition, ratiometric analysis is particularly important to quantify the relative abundance of different molecular species and gain insights into metabolic changes. For instance, by simultaneously imaging the C-H stretching vibration and the C-D stretching vibration, researchers can distinguish between labeled and unlabeled molecules, enabling precise quantification of metabolic activities. However, typical femtosecond SRS systems allow the acquisition of information in only one vibrational band at a time, whether in the high wavenumber regions (C-H stretching, O-H stretching), the C-D/cell silent region, or the fingerprint region. Collecting information from multiple bands requires wavelength tuning, which is time-consuming and hence unsuitable for fast dynamic studies. Moreover, sequential tuning may introduce issues such as drift in laser power or sample movement, further complicating the quantification accuracy. Therefore, advancements that enable simultaneous multi-band acquisition are essential for improving the robustness and speed of SRS quantification in metabolic studies.

1.4 DISSERTATION OVERVIEW

This dissertation presents several advancements in SRS microscopy to address key challenges in studying protein and lipid metabolism. First, we constructed a dual-OPO system that generates two tunable femtosecond pulses. By combining the dual-OPO outputs with an additional femtosecond pulse, we developed a unique dual-band SRS microscopy system capable of simultaneously acquiring hyperspectral SRS image stacks in two arbitrary vibrational frequency bands. This approach improves spectral coverage and image acquisition speed by at least 2-fold, without issues associated with sequential wavelength tuning, such as sample movement and laser drift. As a result, the reproducibility and reliability of spectral analysis are significantly enhanced. The detailed characterization of this system is reported in Chapter 2. The versatility of this system is demonstrated through its application to study fatty acid metabolism, cellular drug uptake, and lipid unsaturation levels in tissues.

Subsequently, Chapters 3 and 4 describe the application of multi-band SRS microscopy for measuring single-cell growth rates in two-dimensional (2D) and three-dimensional (3D) cell cultures. Intratumoral heterogeneity is a major factor contributing to drug resistance in cancer treatments, and the ability to monitor cell growth at the single-cell level provides valuable insights into drug-cell interactions. By using deuterium-labeled amino acids, we developed a label-free ratiometric SRS approach to quantify cell growth rates with high sensitivity, providing a faster and higher content measurement than traditional assays.

We further expand this technique by combining single-cell growth measurements with intracellular drug uptake analysis to explore differences between 2D and 3D cell culture systems during cancer drug treatment. It is well known that 3D cultures more accurately replicate the tumor microenvironment compared to traditional 2D cultures, often exhibiting increased resistance to drugs. Our study combines three-band SRS imaging to investigate how drug penetration, uptake, and resistance differ between 2D and 3D cell cultures. This provides deeper insight into the mechanisms of drug resistance in 3D microenvironments, which is crucial for the development of effective cancer treatments.

The focus then shifts to applying SRS microscopy to study lipid metabolism in tissue samples. Nonalcoholic fatty liver disease (NAFLD) and its progression to nonalcoholic steatohepatitis

(NASH) involve complex lipid metabolic changes. Understanding the lipid composition and spatial distribution within the liver tissue can offer insights into the mechanisms driving disease progression. In Chapter 5, we employed our dual-band hyperspectral SRS microscopy to classify and quantify different lipid molecules in liver tissue sections from patients, correlating their distribution with disease progression. In conjunction with polarization microscopy, this approach allowed for the detailed investigation of lipid species, including cholesteryl esters and triglycerides, and provided new information on the association of birefringent crystals with NASH.

Finally, in Chapter 6, this dissertation examines lipid peroxidation during ferroptosis, a form of regulated cell death driven by the accumulation of lipid peroxides. Different exogenous lipids mediate ferroptosis differently. Experimentally characterizing different lipid peroxidation mechanisms and products in cells is vital for understanding this process. Using SRS microscopy, we explore the spectral and intensity changes caused by peroxidation of different lipids, providing experimental evidence for the formation of lipid peroxides and their intracellular localization during ferroptosis. These findings enhance our understanding of ferroptosis mechanisms and may facilitate therapeutic approaches for conditions involving oxidative stress.

Overall, this dissertation highlights advancements in SRS microscopy techniques and their applications for studying protein and lipid metabolism in both cellular and tissue contexts. By enhancing the capabilities of SRS microscopy and applying it to relevant biological problems, this work aims to deepen our understanding of metabolic processes and provide insights that may support the development of targeted therapies for various diseases.

CHAPTER 2. SIMULTANEOUS DUAL-BAND HYPERSPECTRAL STIMULATED RAMAN SCATTERING MICROSCOPY WITH FEMTOSECOND OPTICAL PARAMETRIC OSCILLATORS

The work presented in this chapter has been published in the following article[100]*:*

Xu, F. X.; Rathbone, E. G.; Fu, D. Simultaneous Dual-Band Hyperspectral Stimulated Raman Scattering Microscopy with Femtosecond Optical Parametric Oscillators. *J. Phys. Chem. B* **2023**, *127* (10), 2187–2197. https://doi.org/10.1021/acs.jpcb.2c09105.

2.1 INTRODUCTION

As described in the previous chapter, Raman spectroscopy is a non-destructive and non-invasive technique with a wide range of applications, from molecule identification to material characterization to biomedical imaging.[101] Because spontaneous Raman microscopy directly probes intrinsic vibrational modes of molecules in inhomogeneous biological specimens such as cells and tissues at the laser focus, it allows non-perturbative spatially resolved biochemical analysis.[102,103] However, it suffers from low signal and long acquisition time. Stimulated Raman scattering (SRS) microscopy addressed these drawbacks by employing ultrafast laser excitation and a high-frequency phase-sensitive detection system to increase imaging sensitivity and improve the acquisition speed substantially.[104,71,70] In an SRS process, two synchronized ultrafast lasers of different frequencies, referred to as pump and Stokes, coherently excite a specific vibrational transition that matches the photon energy difference. The SRS signal has a linear dependence on chemical concentration and therefore allows quantitative analysis of targeted molecules.

However, the application of SRS microscopy is hindered by its narrow spectral coverage compared to spontaneous Raman microscopy. Traditional SRS microscopy using picosecond pulses with a narrow bandwidth of <10 cm^{-1} can only probe a single Raman transition at a time. Laser wavelength tuning is required to achieve hyperspectral SRS imaging, i.e., acquiring a stack of SRS images at a range of different frequencies.[70,90–92] Although the picosecond laser-based SRS system offers excellent spectral resolution, the wavelength tuning limits the acquisition speed for an image stack. Meanwhile, power drifting or sample movement may occur during the wavelength tuning process, degrading the spectral fidelity. Different methods, such as spectral focusing, spectral dispersion, modulation multiplexing, and Fourier transform SRS, have been implemented to improve the imaging speed of hyperspectral SRS without needing sequential wavelength tuning.[93–98] The spectral focusing method is the most widely used method due to the ease and robustness of the implementation. It starts with two broad-bandwidth femtosecond laser pulses and stretches out the pulses to picoseconds to focus excitation into a single narrow Raman band.[95–97,99] Frequency tuning is achieved by translating a mechanical delay stage, significantly improving the tuning speed and reproducibility. Other methods use a pair of broadband and narrowband lasers to excite multiple Raman bands simultaneously. The difference in these methods is how the Raman frequencies are resolved. Spectral dispersion uses a grating to separate the broadband laser into different wavelengths, each one corresponding to one Raman band.[105,106] Modulation multiplex SRS uses a narrowband Stokes pulse and a broadband pump pulse divided into a series of wavelength bands, each modulated at a different frequency.[94,107] Fourier transform SRS resolves the broadband excitation light by its interferogram.[108] Regardless of the implementation method, they are all limited in spectral coverage due to the modest bandwidth of the femtosecond laser, which is typically around 100-300 cm^{-1}. The spectral coverage can be improved by using femtosecond lasers with larger bandwidth. One example of bandwidth broadening was demonstrated with a parabolic fiber amplifier, where the Stokes laser bandwidth is increased from 6 nm to 60 nm, enabling a spectral coverage of >600 cm^{-1}.[109] This broader range is important for distinguishing chemical compositions in the fingerprint region.[110,111]

In most SRS applications, it is not necessary to capture the entire Raman spectral range. However, collecting SRS images in two separate Raman spectral regions is valuable for background subtraction, ratiometric analysis, or high-accuracy chemical identification. Approaches toward this goal can be generally classified under two categories: one is to excite the target transitions sequentially and optimize the spectral tuning speed, and the other is to employ three laser pulses to probe two transitions concurrently. Ni et al. constructed a multi-window SRS imaging system using a widely tunable picosecond fiber laser with a wavelength tuning time of 5 ms.[112] However, the fiber laser-based SRS is susceptible to higher laser relative intensity noise and thus requires a complicated auto-balanced detection system to achieve a good SNR. Furthermore, acquiring SRS images at two Raman transitions simultaneously is more desirable to minimize laser fluctuation and sample variation. Heuke et al. achieved this goal with a three-beam system using narrowband picosecond lasers.[113] Their system enables the simultaneous acquisition of two SRS images at two arbitrary vibrational frequencies but still relies on laser wavelength tuning for collecting hyperspectral SRS images. They further developed a dual-vibrational frequency SRS imaging system utilizing a broadband pump and two narrowband Stokes beams. However, it only allows for the simultaneous detection of two Raman transitions within 100 cm^{-1} limited by the bandwidth of the pump beam.[114] Other approaches, such as two-color SRS using a polarization encoding scheme, also have a limited separation between the two targeted Raman transitions of around 100-300 cm^{-1}.[115–117]

Here, we present a spectral-focusing SRS imaging system capable of simultaneous acquisition of hyperspectral image stacks in two separate vibrational frequency regions, each with a spectral coverage of >300 cm^{-1}. Our system utilizes a femtosecond laser pulse as the Stokes beam and two femtosecond pump beams at different wavelengths generated by two synchronously pumped optical parametric oscillators to probe two desired vibrational frequency bands between 650 – 3280 cm^{-1}. We show the capability of dual-band SRS imaging in investigating fatty acid metabolism, drug uptake in cells, and lipid unsaturation in tissues. We also demonstrate the ability to perform broadband fingerprint SRS imaging by making a simple adjustment to our typical setup. We can achieve a spectral coverage of 1100 – 1800 cm^{-1} without wavelength tuning. Overall, our presented simultaneous dual-band hyperspectral SRS microscopy technique enables accurate ratiometric analysis and provides at least a two-fold increase in hyperspectral image acquisition speed without sacrificing image quality. To the best of our knowledge, this is the first reported SRS microscopy system that is capable of simultaneous dual-band hyperspectral SRS acquisition.

2.2 MATERIALS AND METHODS

2.2.1 *Cells culture*

The human lung adenocarcinoma cell line, A549 cells (ATCC), were maintained at 37°C in a humidified 5% CO_2 incubator and cultured in Dulbecco's modified eagle medium (DMEM, Gibco) supplemented with 10% fetal bovine serum (Hyclone) and 1% penicillin-streptomycin (Gibco). For fixed cell imaging, the cells were seeded on glass coverslips overnight and fixed with 4% paraformaldehyde (PFA) solution for 15 minutes.

2.2.2 *Fatty acid (FA) labeling*

To label A549 cells with fatty acids (FA) or deuterated FA, we first prepared FA/bovine serum albumin (BSA) stock solution by the following procedure: we dissolved 5 mg of FA in hexane and pH-neutralized with 1 M NaOH; evaporated the solution with dry nitrogen to produce FA salts; then added 1 mL of warm water to dissolve the salts, followed by 4 mL of warm 10%w/v BSA solution. The FA/BSA solution was supplemented into the DMEM cell culture medium to the desired concentration. After seeding the A549 cells on glass coverslips for 1 day, we incubated the cells in the FA-supplemented medium for 13 hours to perform fatty acid labeling.

For deuterated FA labeling, A549 cells were supplemented with 0.4 mM deuterated stearic acid (SA-d_{35}). After incubation, we fixed the cells and imaged them in the C–H region, 2800 – 3070 cm^{-1}, and the C–D region, 1970 – 2300 cm^{-1}.

For lipid unsaturation quantification, we supplemented A549 cells with 0.2 mM oleic acid (OA) or palmitic acid (PA). The cells were fixed before being imaged in the C–H region, 2800 – 3070 cm^{-1}, and the fingerprint region, 1400 – 1760 cm^{-1}.

2.2.3 *Kinase inhibitor treatment*

Lapatinib (Selleckchem) was dissolved in deuterated DMSO (DMSO-d_6) to make a 10 mg/mL stock solution. The stock solution was diluted with cell culture medium to 2 μM for drug treatment. A549 cells were seeded on coverslips for 1 day before being treated with 2 μM lapatinib for 29 hours. Control cells were treated with DMSO-d_6 only. After treatments, we washed the cells with phosphate-buffered saline and immediately performed live cell imaging in the C–H region, 2800 – 3070 cm^{-1}, and the fingerprint region, 1235 – 1665 cm^{-1}.

2.2.4 *Mouse adipose tissues*

Adipose tissues were dissected from a mouse carcass and stored in phosphate-buffered saline. The mouse tissues were imaged in the C–H region, 2800 – 3070 cm^{-1}, and the fingerprint region, 1400 – 1760 cm^{-1}.

2.2.5 *Dual-band SRS imaging*

The simultaneous dual-band SRS microscopy setup is shown in Figure 2.1A. The output of a femtosecond oscillator (Light Conversion FLINT-FL2) with a repetition rate at 77.2 MHz and a center wavelength at 1030 nm is split into two beam paths by a polarizing beam splitter (PBS). One beam serves as the Stokes beam for SRS imaging, and the other is directed into a homebuilt dual-output optical parametric oscillator (OPO) system (Figure 2.1B). In the dual-OPO system, the second harmonic generation (SHG) of the input laser is split into two pulse trains with a 50/50 nonpolarizing beam splitter (NBS) to pump the two tunable OPOs. OPO 1 has an emission wavelength range of 700 – 800 nm, allowing the excitation of vibrational modes from 2790 cm^{-1} to 4580 cm^{-1}. OPO 1 is typically set at 790 nm for SRS imaging in the C–H stretching region. OPO 2 has a broad tuning range of 770 – 965 nm, allowing the excitation of a wide range of vibrational frequencies from 650 cm^{-1} to 3280 cm^{-1}. The OPO emission spectra are shown in Figure 2.1D - E.

The two tunable OPO output beams are then combined by an 808 nm long pass (LP) dichroic mirror (Edmund Optics) and chirped to approximately 2 ps with high dispersion SF11 dense flint glass rods (GR, Newlight Photonics). The Stokes beam is modulated at 19.3 MHz with an electro-optical modulator (EOM, Thorlabs EO-AM-NR-C2) and chirped to approximately 2 ps using a grating stretcher (GS, LightSmyth). The three beams are combined with a 1000 nm short pass (SP) dichroic mirror (Thorlabs) and temporal overlapped using two motorized delay stages (DS, Zaber X-DMQ-AE and Thorlabs MCM3000). The overlapped pulses are sent into a homebuilt upright laser scanning microscope system equipped with a 40X water immersion objective (Nikon N40XLWD-NIR, NA = 1.15) and an oil immersion condenser (Nikon MEL41410, NA = 1.4). For simultaneous dual-band SRS imaging detection, the two pump beams are isolated using a 1000 nm SP filter, separated with an 808 nm LP dichroic mirror, and then detected by two amplified Si photodiodes (PD). The signals detected by both PDs are demodulated with a multi-channel lock-in amplifier (LIA, Liquid instruments Moku:Pro) at a time constant of 4 µs to generate 512 × 512 pixel SRS images with an estimated spatial resolution of around 400 nm. The pixel size was 0.39 µm/pixel. A delay stage controls the interpulse delay between the Stokes beam and the pump beams. As a result, the system allows us to collect hyperspectral SRS images at two desired vibrational frequency regions.

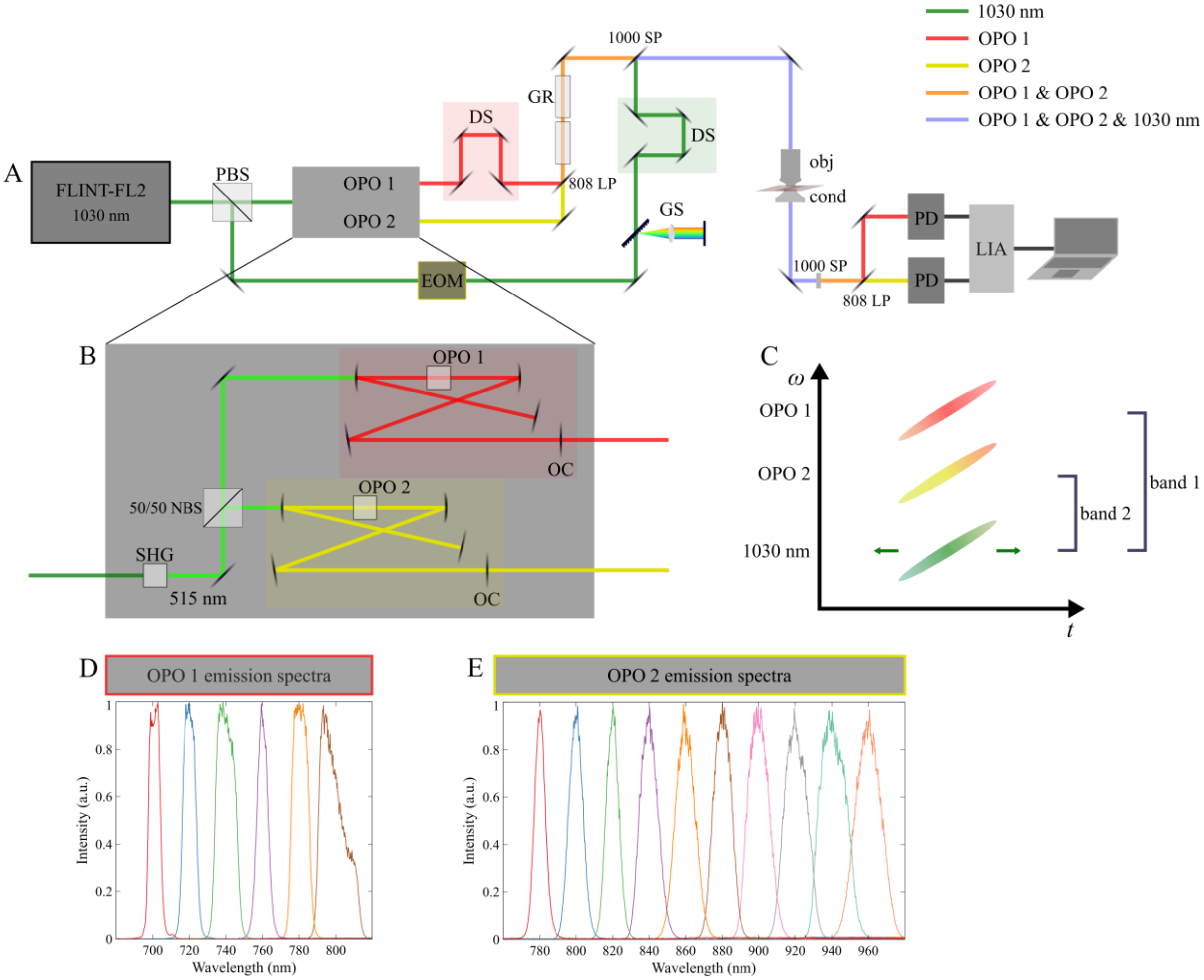

Figure 2.1. Schematic diagram of the simultaneous dual-band hyperspectral SRS microscopy system and spectral characteristics of the pump lasers. (A) Diagram of the SRS system pumped by a high-power femtosecond oscillator FLINT-FL2. PBS: polarizing beamsplitter; OPO: optical parametric oscillator; DS: delay stage; LP: long pass dichroic; SP: short pass dichroic; GS: grating stretcher; obj: microscope objective; cond: microscope condenser; PD: photodiode; LIA: lock-in amplifier. (B) Zoom-in diagram of the two homebuilt OPO systems. SHG: second-harmonic generation; OC: output coupler. (C) Diagram of the chirped Stokes and two pump beams and their probed SRS bands. Green arrows indicate the frequency tuning through spectral focusing. (D) Tunable emission spectra of OPO 1. (E) Tunable emission spectra of OPO 2.

2.3 RESULTS AND DISCUSSION

2.3.1 *Simultaneous C–D/C–H imaging for visualizing fatty acid uptake in cells*

We first applied simultaneous dual-band SRS microscopy to investigate fatty acid (FA) uptake and accumulation in cells. The FA transport in lipid droplets is an essential component of lipid metabolism in cells. FA/BSA solutions supplemented cell culture medium has been established for *in vitro* lipotoxicity models to monitor the cellular uptake of lipid molecules.[118] As cells grow in a deuterated FA-supplemented culture medium, they incorporate deuterated FA in membranes and lipid droplets. It has been verified that the alternation from non-deuterated FA to deuterated FA does not affect cellular activity; hence, deuterated FA is an ideal probe for studying cellular FA uptake.[119] Previous research has shown that combined with deuterium labeling, SRS microscopy can be used to explore and quantify FA uptakes in single cells and tissues.[82,120,79] To achieve accurate quantification of FA metabolism, it is important to image the sample at both the C–D and C–H regions concurrently to minimize errors caused by laser fluctuation, power variation, or focus drifting.

To visualize deuterated FA uptake in a cancer cell model, we treated A549 cells with SA-d_{35}. We set the OPO 1 output at 790 nm for C–H band imaging and tuned the OPO 2 output to 845 nm to probe the C–D region. Figure 2.2A - B show the representative SRS images of SA-d_{35} labeled A549 cells at 2105 cm^{-1}, the SA-d_{35} Raman peak in the C–D region, and at 2850 cm^{-1}, the lipid CH_2 stretching peak in the C–H region. We can observe the high FA accumulation in cell lipid droplets by taking the ratio between the two images, as demonstrated in Figure 2.2C. The relative rate of FA uptake is quantifiable at the single lipid droplet level based on their intensities in the ratiometric image. To generate the ratiometric image, we first created a cell mask by thresholding the C–H images, and applied the binary mask to the calculated ratiometric image to eliminate noisy pixels in the background regions. The SRS spectra in both the C–D and C–H regions were generated from two hyperspectral image stacks acquired simultaneously. The C–D spectrum of the selected cell lipid droplets matches the SRS spectrum of the pure SA-d_{35} sample, confirming the identity of accumulated lipids. The control cells, shown in Figure 2.2D - F, do not have visible signals in the C–D channel and the C–D/C–H ratiometric image. The C–D SRS spectrum of the highlighted control cell, shown in Figure 2.2G, validates that the control cells only have extremely low signal due to non-Raman background in the C–D spectral region.

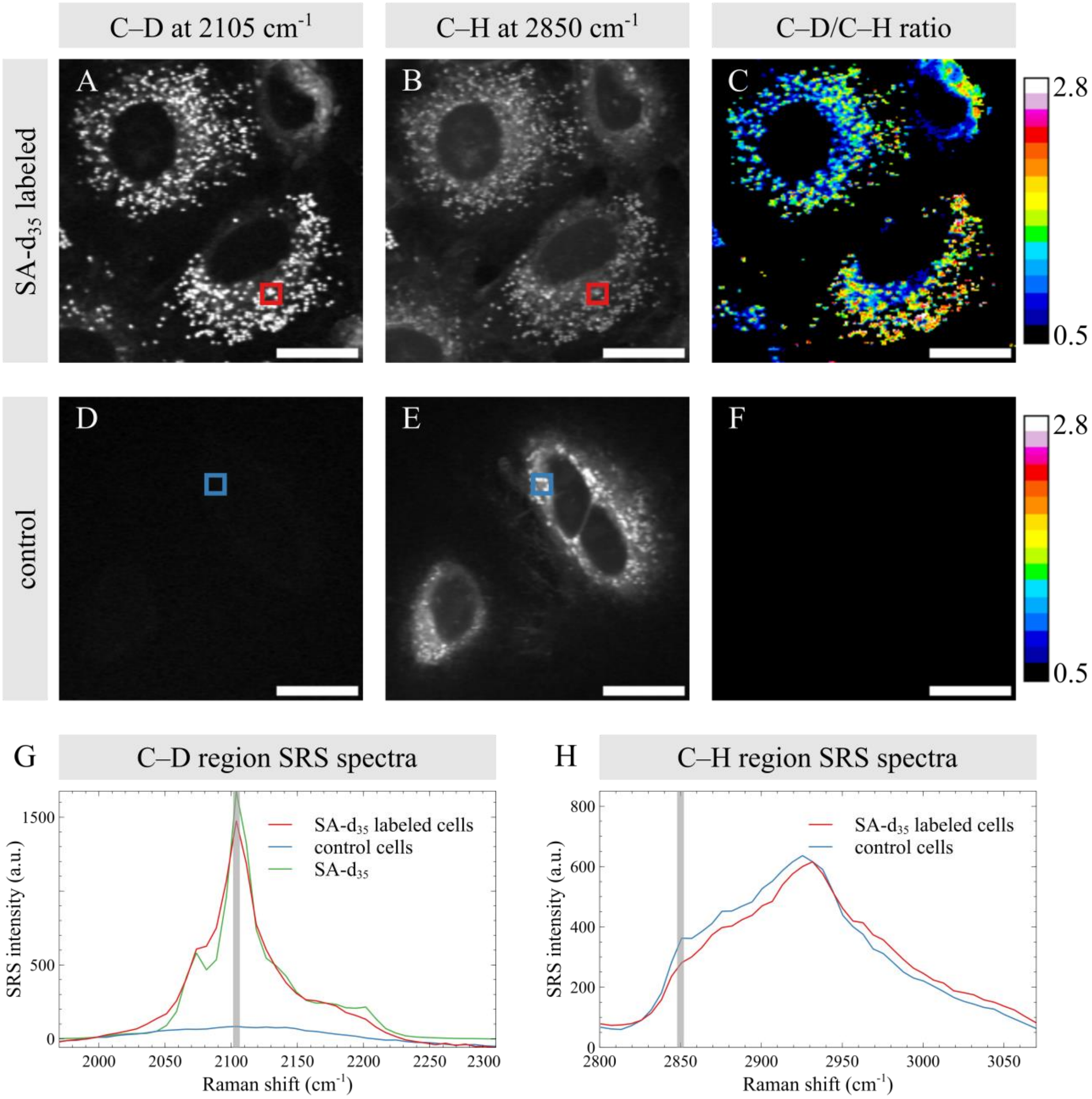

Figure 2.2. Representative SRS images and spectra of SA-d35 labeled and control A549 cells. (A-C) C–D, C–H, and C–D/C–H ratiometric SRS images of SA-d35 labeled cells. (D-F) C–D, C–H, and C–D/C–H ratiometric SRS images of control cells. (G-H) C–D and C–H region SRS spectra of selected cellular regions and pure SA-d35 sample. Pixel dwell time: 12.8 µs. Power: OPO 1 beam (790 nm) 40mW, OPO 2 beam (845 nm) 40 mW, and 1030 nm beam 100 mW. Scale bar: 20 µm.

2.3.2 *Fingerprint/C–H imaging for tracking intracellular drug uptake*

Hyperspectral SRS has been used to directly visualize and quantify drug uptake in live cells with submicron resolution and high sensitivity.[121,122] In order to obtain a high contrast from the drugs at a low concentration in cells, it is typically desirable to image at a drug peak that is distinct from the cell background. Tuning the laser wavelength to acquire additional cellular morphological information is necessary for a typical SRS setup. However, cell organelles such as lysosomes move rapidly during live cell imaging experiments. Therefore, simultaneous dual-band SRS detection is crucial to colocalize drug and cell organelles.

To validate the capability of visualizing intracellular drug uptake, we performed live cell dual-band SRS imaging on A549 cells treated with a cancer drug lapatinib. The OPO 1 output was at 790 nm to probe the C–H region for cellular morphology mapping. We set the OPO 2 output to 900 nm to excite the spectral region covering prominent lapatinib peaks in the fingerprint region. As shown in Figure 2.3G, the lapatinib solution has a prominent peak at 1368 cm^{-1} with a weaker shoulder at 1412 cm^{-1}. We selected the strongest peak at 1368 cm^{-1} for the ratiometric analysis. An example SRS image at this drug peak is shown in Figure 2.3A. By taking the ratio between the images at the lapatinib peak and the cell peak at 2930 cm^{-1} (Figure 2.3B), Figure 2.3C highlights the localization of drug accumulation in the cell. Based on the well-established lysosomotropic effect that the acidic environment in lysosomes protonates the weakly basic drugs and consequently enriches drug molecules[123], we postulate that the localization of high lapatinib buildup correlates with lysosome dense regions. The control cells showed no peak at 1368 cm^{-1} (Figure 2.3G). The cell signals in Figure 2.3D were contributed by the broad cell peak at 1480 cm^{-1}. The control cells' 1368 cm^{-1}/2930 cm^{-1} ratiometric image in Figure 2.3F has relatively low intensity, confirming that the high signals in the lapatinib-treated cells' ratiometric image are predominately due to accumulated drug molecules.

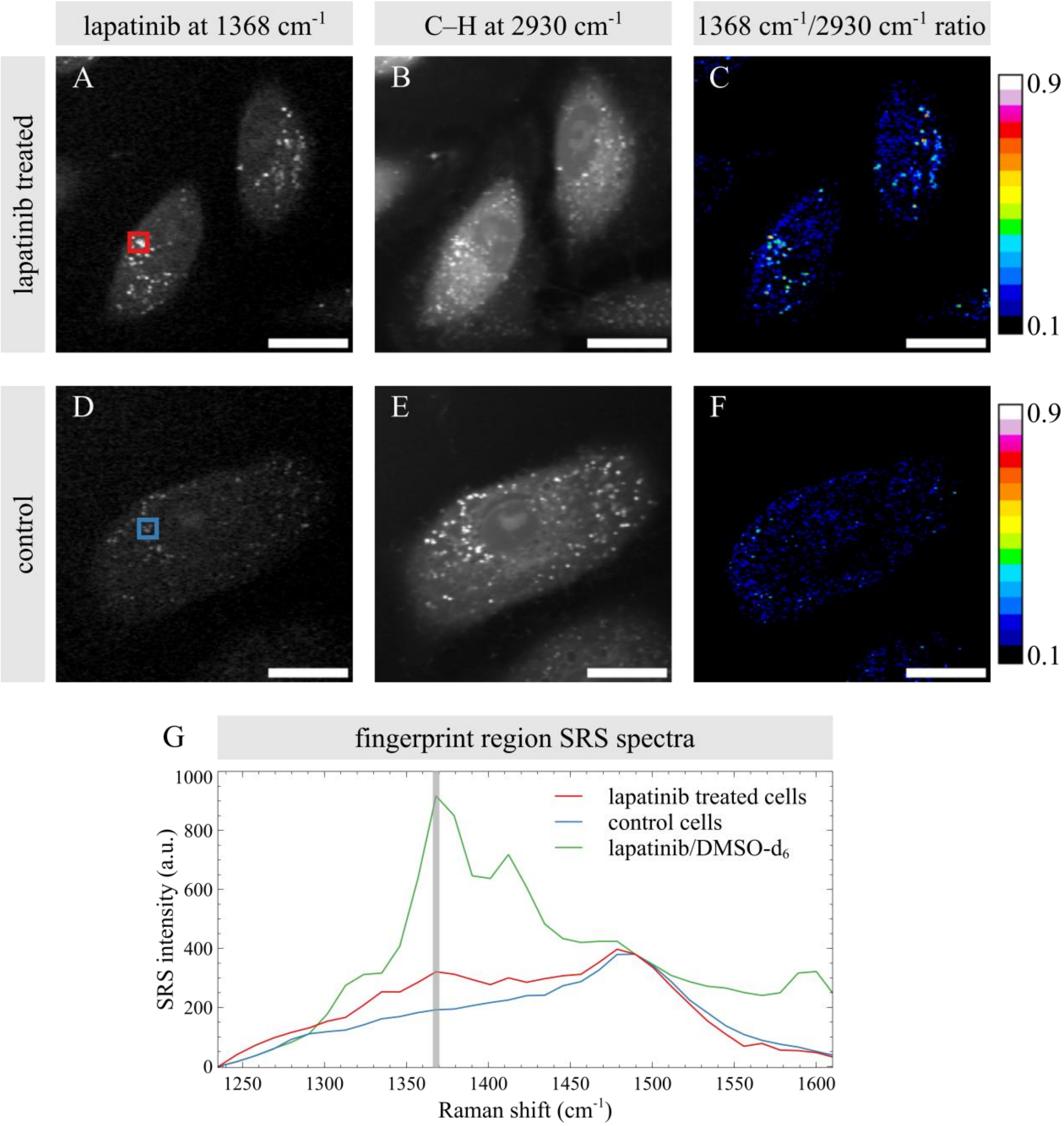

Figure 2.3. Representative SRS images and spectra of lapatinib-treated and DMSO-d6 vehicle control A549 cells. (A-B) SRS images at the lapatinib peak in the fingerprint region at 1368 cm-1 and cell peak in the C–H region at 2930 cm-1. (C) The 1368 cm-1/2930 cm-1 ratiometric image of the treated cells, highlighting the intracellular drug uptake. (D-F) The lapatinib peak, cell peak,

and ratiometric SRS images of a control cell. (G) The 1235 – 1665 cm-1 fingerprint SRS spectra of selected cellular regions and lapatinib stock solution. Pixel dwell time: 12.8 µs. Power: OPO 1 beam (790 nm) 40mW, OPO 2 beam (900 nm) 22.5 mW, and 1030 nm beam 100 mW. Scale bar: 20 µm.

2.3.3 *C = C/C–H imaging for quantifying lipid unsaturation in cells and tissues*

Next, we demonstrate the use of dual-band SRS imaging to determine lipid unsaturation. The unsaturation degree of lipid species has been suggested as one of the essential factors for metabolic syndrome.[124,125] For example, growing evidence indicates that monounsaturated fatty acids, such as oleic acid, can increase insulin sensitivity, while saturated fatty acids promote insulin resistance.[126,127] Raman techniques, including SRS microscopy, have been established as excellent tools for the quantitative determination of lipid unsaturation levels in biological samples by measuring the ratio between the quantity of carbon-carbon double bonds (C = C) within lipid acyl chains and CH_2 bonds.[124,80,128–134] Here, we utilized our dual-band SRS imaging system to explore the lipid unsaturation pattern in fatty acid-labeled cells and mouse adipose tissues.

To excite the Raman vibrational transition of lipid acyl chain C = C bond stretching at 1656 cm^{-1}, we tuned the OPO 2 output to 884 nm, while the OPO 1 output stayed at 790 nm to probe the strong CH_2 stretching mode at 2850 cm^{-1}. We show representative SRS images of A549 cells labeled with unsaturated oleic acid (OA) at the 1656 cm^{-1} C = C peak and 2850 cm^{-1} CH_2 peak in Figure 2.4A - B, respectively, and the corresponding images of cells labeled with saturated palmitic acid (PA) in Figure 2.4D - E. The 1656 cm^{-1}/2850 cm^{-1} ratiometric images enabled direct visualization of the distinct lipid unsaturation levels in FA-labeled cells as demonstrated by Figure 2.4C and G. It has been established that the ratio between the unsaturation peak in the C–H region at around 3015 cm^{-1} and the CH_2 stretching peak at 2850 cm^{-1} can be used to quantitatively identify lipid unsaturation level.[129] Therefore, we validated the 1656 cm^{-1}/2850 cm^{-1} ratiometric images by comparing it to the 3015 cm^{-1}/2850 cm^{-1} images (Figure 2.4D and H) and obtained consistent results. The lipid droplets in OA-treated cells have higher intensities in both ratiometric images, indicating a higher unsaturation level compared to PA-treated cells. The lipid droplet SRS spectra of cells under different treatments match the SRS spectra of pure fatty acids (Figure 2.4I and J). We note that lipid droplets in PA-treated cells have a small peak at 1656 cm^{-1}, which is dominantly contributed by protein amide signals from the cells due to the small size of droplets.

After validation and calibration for the 1656 cm^{-1}/2850 cm^{-1} SRS images, we performed ratiometric imaging on mouse fat tissues to explore the lipid unsaturation pattern of adipose cells. In the representative ratiometric image of mouse adipose tissues, Figure 2.4M, we observed that most large lipid droplets are close to saturated, whereas smaller lipid droplets have a higher unsaturation level. The unsaturation level in each of the imaged lipid droplets is relatively uniform. It is important to note that the outer ring of all lipid droplets appears to have a slightly higher unsaturation level, and this is most likely caused by the edge effect of the surrounding solvent spectrum mixed with the lipid spectrum.

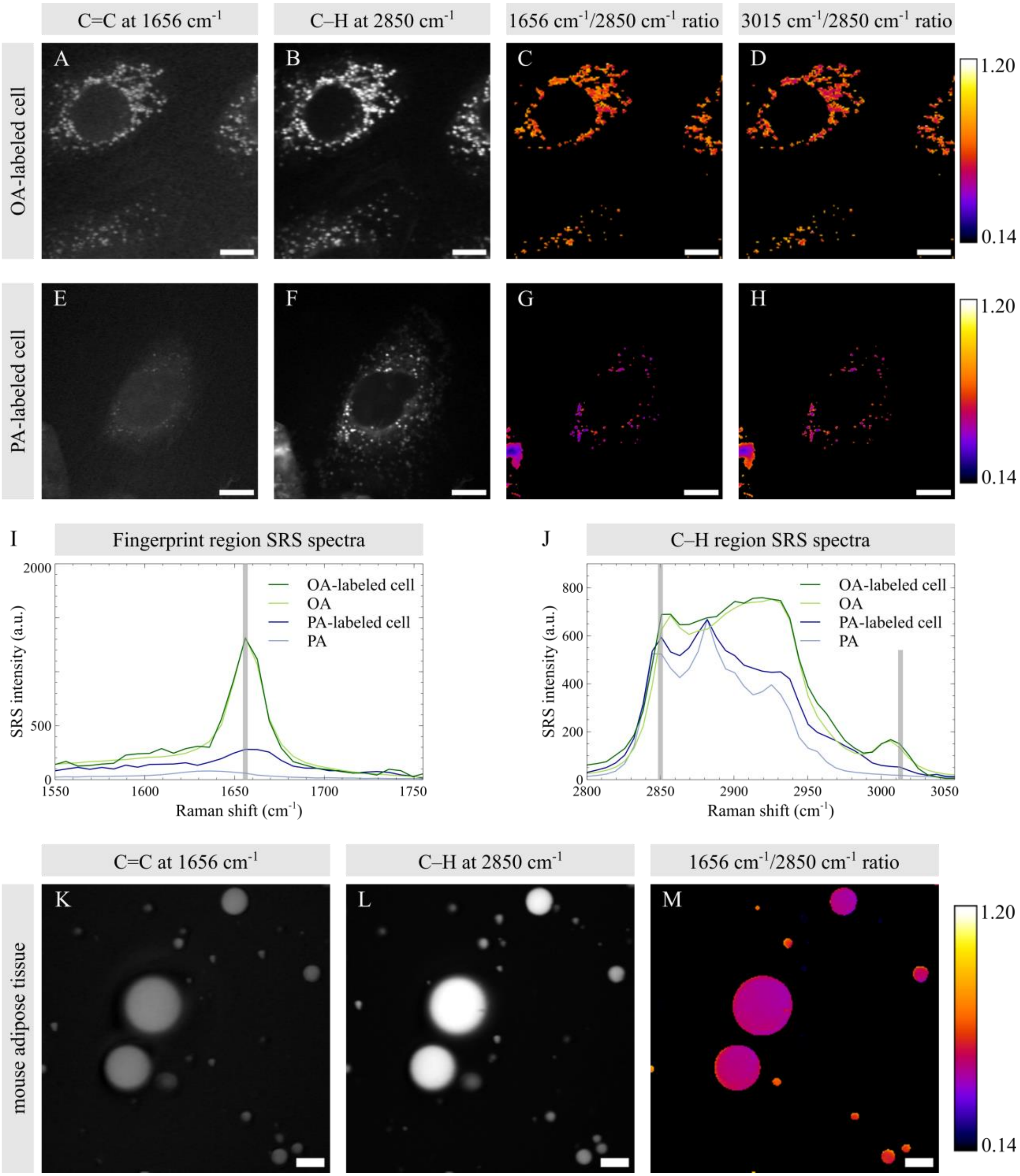

Figure 2.4. Representative SRS images and spectra of FA-treated A549 cells and mouse adipose tissue. (A-D) The C=C at 1656 cm^{-1}, C–H at 2850 cm^{-1}, 1656 cm^{-1}/2850 cm^{-1}, and 3015 cm^{-1}/2850 cm^{-1} ratiometric SRS images of A549 cells labeled with oleic acid. (E-H) Corresponding SRS and ratiometric images of A549 cells labeled palmitic acid. (I-J) SRS spectra of pure fatty acids and lipid droplets in fatty acid-labeled cells. (K-M) SRS images at 1656 cm^{-1} C=C peak,

2850 cm^{-1} C–H peak, and 1656 cm^{-1}/2850 cm^{-1} ratiometric image of mouse adipose tissues. Pixel dwell time: 12.8 µs. Power: OPO 1 beam (790 nm), OPO 2 beam (884 nm), and 1030 nm beam are all at 40 mW. Scale bar: 10 µm.

2.3.4 *Broadband fingerprint imaging with a dual-modulation scheme*

Lastly, we demonstrate broadband hyperspectral SRS imaging using the dual-band SRS microscopy system with a simple modification to the setup and careful selection of laser wavelengths. The schematic diagram of the modified system is illustrated in Figure 2.5. An additional EOM, indicated by the red arrow, is added to the OPO 1 beam path and modulates the OPO 1 output pulse at 10.3 MHz. The pulse scheme diagram in Figure 2.6A shows the interaction between the three laser pulses. Instead of using two photodiodes to detect both OPO pulses as in the regular dual-band imaging system, only one photodiode is used for the detection of the OPO 2 pulses, which acts as the Stokes for the OPO 1 beam and the pump for the 1030 nm beam. The multi-channel lock-in amplifier demodulates the Raman signals at two different frequencies. At 10.3 MHz, the SRS signals are in the spectral region between 1100 cm^{-1} to 1500 cm^{-1} probed by the OPO 1 pulse at 790 nm and the OPO 2 pulse at 884 nm; meanwhile, at 19.3 MHz, the SRS signals are in the spectral region of 1500 – 1800 cm^{-1} excited by the OPO 2 pulse at 884 nm and the 1030 nm beam. By concatenating the SRS hyperspectral images collected at the two frequencies, we can obtain SRS spectra with a wide spectral coverage of nearly 700 cm^{-1} in the fingerprint region.

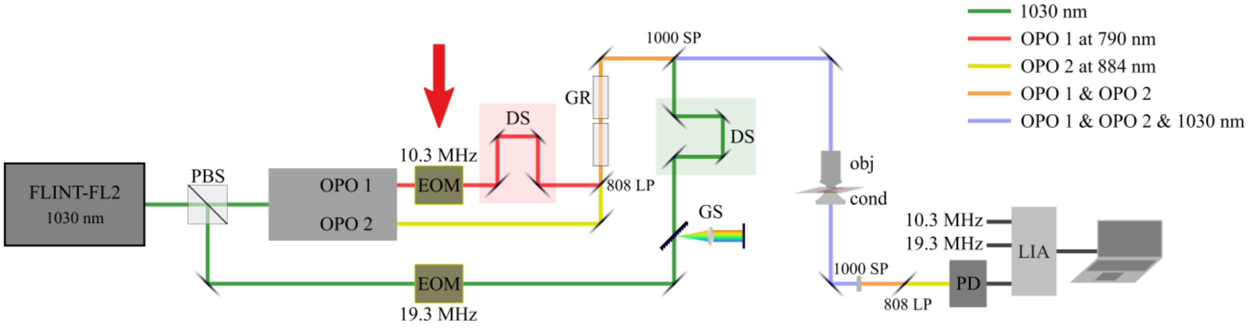

Figure 2.5. Schematic diagram of the modified dual-band SRS microscopy setup for broadband fingerprint region hyperspectral SRS imaging. The OPO 1 output pulse is modulated at 10.3MHz by an additional EOM (indicated by the red arrow). Only the OPO 2 pulse is detected and demodulated at two frequencies to retrieve SRS signals in two bands.

The 1100 – 1800 cm^{-1} fingerprint region contains abundant signature spectral information of major biomolecules, such as proteins, lipids, and DNA, and hence has been frequently used for cell state classification and cancer diagnosis.[135–137] To demonstrate the performance of fingerprint region imaging with our broadband hyperspectral SRS microscopy system, we first applied it to five pure liquids - nitrobenzene, benzonitrile, oleic acid, acetone, and toluene, and plotted the collected fingerprint region SRS spectra in Figure 2.6B. The spectral resolution is approximately 15 cm^{-1}, estimated as the full width at half maximum of the nitrobenzene 1346 cm^{-1} peak. The results match the spontaneous Raman spectra of those liquids in terms of peak positions and spectral shapes.[109,138,139] Relative peak intensities are slightly different due to the intrinsic limitation of the spectral focusing method: peaks near the two ends of the spectral coverage are weaker compared to peaks close to the center. We then performed broadband fingerprint region SRS imaging on fixed A549 cells. A representative SRS image at 1656 cm^{-1} and the fingerprint region SRS spectrum with main peak assignments are shown in Figure 2.6C - D, respectively. We note that the cell spectrum in the 1100 – 1500 cm^{-1} region is noisier than the other half due to weaker signals. Nevertheless, we can identify the expected cellular Raman peaks, primarily contributed by amide bands and C–H bending in proteins and lipids, in the acquired spectrum.

The dual-modulation configuration also allows hyperspectral SRS imaging at two separated vibrational frequency bands. The main advantage of this approach is that it enables the excitation of low wavenumber vibrations (<650 cm^{-1}), which is unattainable with the single-modulation configuration, limited by the OPO 2 tuning range. However, compared to the single-modulation approach, this method requires synchronized movements of two motorized stages for simultaneous hyperspectral stacks acquisition, which may decrease the acquisition speed. The dual-modulation approach can be optimized by implementing a delay stage in the OPO 2 beam path.

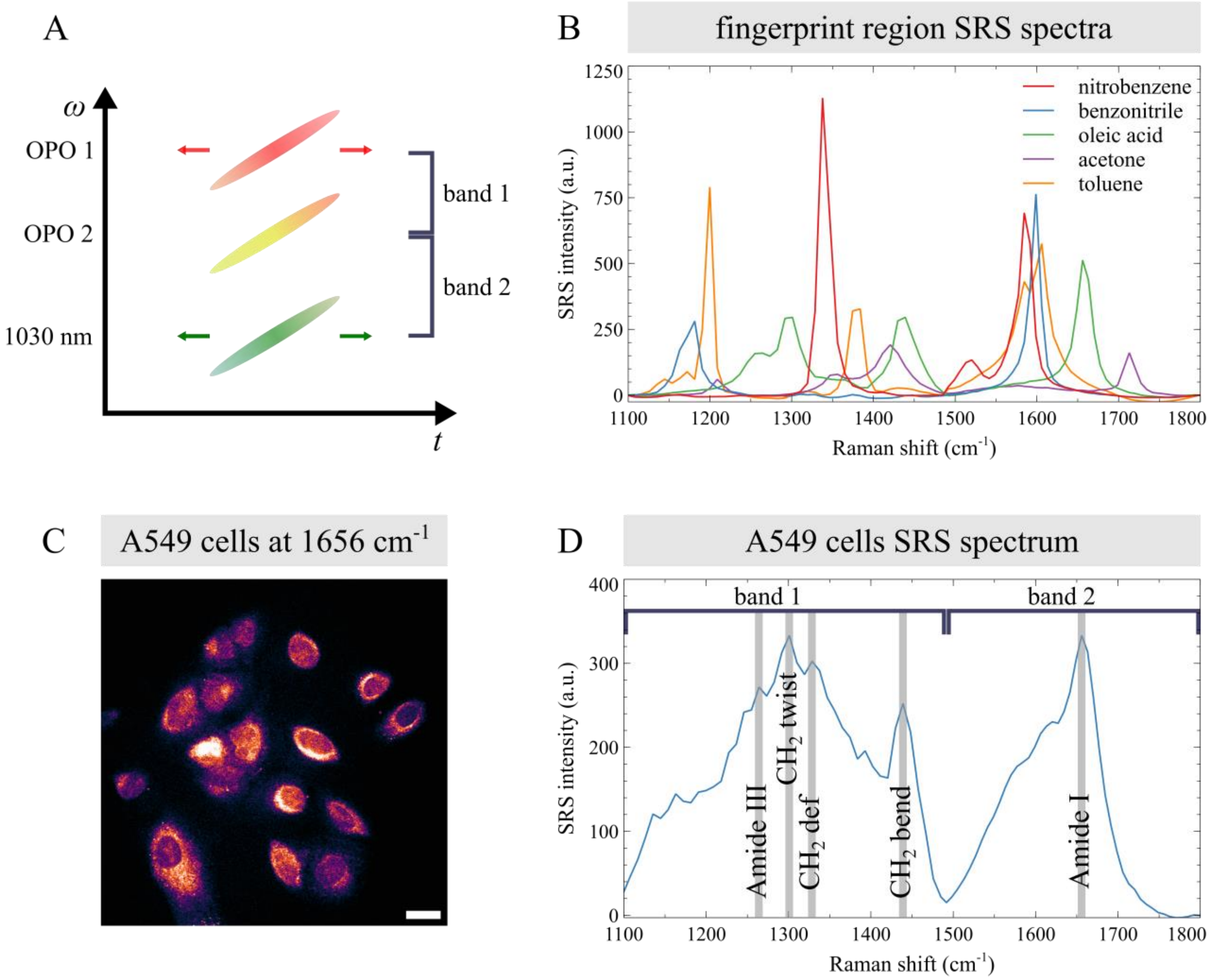

Figure 2.6. Broadband fingerprint region hyperspectral SRS imaging with modified dual-band SRS microscopy setup. (A) Diagram of the chirped beams and their probed SRS bands in the broadband SRS imaging system. (B) The 1100 – 1800 cm^{-1} fingerprint region SRS spectra of nitrobenzene (red), benzonitrile (blue), oleic acid (green), acetone (magenta), and toluene (orange). (C) Representative SRS image of A549 cells at 1656 cm^{-1} acquired with the modified dual-band SRS microscopy setup. (D) Average SRS spectrum of these cells. Pixel dwell time: 32 µs. Power: OPO 1 beam (790 nm) 26 mW, OPO 2 beam (884 nm) 40 mW, and 1030 nm beam 40 mW. Scale bar: 20 µm.

2.4 CONCLUSIONS

SRS microscopy has emerged to be a powerful method for biomedical imaging with high spatial and temporal resolution. The hyperspectral imaging capability enables quantitative biochemical analysis in cells and tissues. However, such analysis often requires ratiometric imaging and careful evaluation of background.[140] As a result, it is desirable to acquire SRS images at two separate spectral regions. Most existing hyperspectral SRS imaging methods have a limited spectral coverage of <300 cm^{-1}. We presented a dual-band SRS microscopy system that enables the simultaneous acquisition of hyperspectral SRS image stacks in two arbitrary vibrational frequency bands, between 650 – 3280 cm^{-1}. The laser system is comprised of two homebuilt tunable OPO systems pumped by the SHG output of a broadband femtosecond laser. The direct output of the femtosecond oscillator is the Stokes beam which interacts with the two synchronous pump beams from OPOs to probe two separate vibrational transitions. Both OPOs are tunable, allowing independent and flexible control of the Raman frequency range. The spectral focusing configuration allows us to perform simultaneous hyperspectral SRS imaging in the two vibrational regions without wavelength tuning. This leads to an improvement in the image stack acquisition speed by at least 2-fold without problems associated with sequential wavelength tuning such as sample movement and laser drifting, therefore increasing the reproducibility and reliability of spectral analysis.

In this work, we demonstrated selected applications of the dual-band hyperspectral SRS system, including visualizing and quantifying fatty acid accumulation, drug uptake in cells, and lipid unsaturation levels in tissues. These examples show the system's capability of acquiring quantitative chemical information in the fingerprint region or cell silent region with Raman tags, such as deuterium labeling and alkyne tags, while simultaneously obtaining high-fidelity morphological features from the C–H stretching region. In addition, it is possible to tune the OPOs to simultaneously excite the O–H and C–H stretching modes for cell density and tissue lipid and protein concentration measurements.[117,141] With the three-dimensional imaging capability of SRS, we can also extend this technique to 3D tissue and *in vivo* applications. Furthermore, we showed the potential of the system in broadband SRS imaging with a dual-modulation configuration, which allows rapid collection of rich spectral information of major biochemical constituents, including proteins, lipids, and DNA.

It is important to point out that our OPO wavelength tuning, especially of greater than 50 nm, requires power optimization and slight realignment. The spectral resolution in different vibrational regions also needs individual optimization by changing the length of glass rods in the OPO beam paths or translating the grating stretcher in the Stokes beam path. Fully automated laser optimization and pulse stretching adjustment would further improve the system's usability. For many applications, it is not necessary to acquire hyperspectral stacks across broad spectral regions. Collecting SRS images at selected wavenumbers can be more efficient. Currently, the delay adjustment is achieved with motorized stages. Faster delay adjustment using a galvanometer mirror in each arm can be implemented to achieve arbitrary discrete sampling of SRS spectra to accelerate the imaging process. Moreover, machine learning and deep learning can be incorporated to augment the imaging capability of our imaging system. For example, by employing a deep learning denoising architect for image processing, it is possible to shorten the image acquisition time.[142] It is also possible to retrieve spectrally-resolved SRS images from sparse SRS sampling or even convert them to specific organelle labeling using deep learning, which significantly increases imaging speed and specificity.[143–145] Overall, this technique provides a powerful platform for fast, quantitative ratiometric SRS analysis of biological specimens in various cell and tissue environments.

CHAPTER 3. MEASURING DRUG RESPONSE WITH SINGLE-CELL GROWTH RATE QUANTIFICATION

The work presented in this chapter has been published in the following article[146]*:*

Xu, F. X.; Wu, R.; Hu, K.; Fu, D. Measuring Drug Response with Single-Cell Growth Rate Quantification. *Anal. Chem.* **2023**, *95* (49), 18114–18121. https://doi.org/10.1021/acs.analchem.3c03434.

3.1 INTRODUCTION

Drug resistance is a primary obstacle to chemotherapy or other drug treatments for cancer, highlighting the importance of accurately evaluating cellular response to drugs during drug discovery and development.[147] However, the majority of existing drug response measurement techniques, such as cell viability assay and proliferation assay, have two main limitations. Firstly, these drug testing assays rely on bulk measurements and cannot resolve variations of single cells. Intra-tumoral heterogeneity is a significant contributor to drug resistance development, and the natural cell-to-cell variation resulting from genetic mutation or gene expression difference can lead to diverse cellular responses to drug treatments.[148–153] Therefore, techniques that can monitor and measure cell exposure and response to drugs at a single-cell level are crucial for investigating cancer cell-drug interactions. By analyzing the response of individual cells to drugs, researchers can better understand the heterogeneity within a population of cancer cells and develop new treatments that target specific subpopulations of cells.[154,155] The other limitation of most drug testing assays is that they only measure traditional pharmacometrics, such as half maximal inhibitory concentration (IC_{50}) or half maximal effective concentration (EC_{50}) values, which depend heavily on cell proliferation rate, assay duration, and growth condition, making it difficult to generalize and compare between different cell lines.[156] Such end-point cell response measurements also fail to provide information on the dynamic cellular changes or insights into the drug mechanisms of action.[157]

Cell growth, a tightly regulated process that plays an essential role in cell cycle progression and proliferation, can be used as an indicator of drug response, as suggested by previous research on single-cell growth rates. [3,158–163] Growth rate inhibition has been demonstrated as a more robust metric for cellular biochemical response to drugs than traditional metrics such as IC_{50} and EC_{50}.[156] However, techniques for accurately quantifying single-cell growth regulation and deregulation are limited. Two currently established methods have shown the ability to determine cell growth rates accurately.[164,165] One method relies on measuring cell buoyant mass using micro-electro-mechanical systems (MEMS) sensors. The single-cell buoyant mass is calculated as the product of cell volume and density difference between the cell and the fluid in the microfluidic system.[166,167] A high mass accuracy of 0.05% of cell buoyant mass has been achieved.[164] However, the requirement for the cells to be isolated and suspended significantly limits the system throughput to only 60 mammalian cells per hour.[168] The other technique of measuring cell growth rate relies on the determination of dry mass, the mass of all cellular components except water, using quantitative phase imaging (QPI).[169] The accuracy of QPI dry mass measurement has been reported to be <10 pg, or 1% of cell drymass.[164,170] However, the QPI techniques have only been applied to monolayer cell growth measurements. The limited capability of imaging isolated or monolayer cells hinders the quantification of cellular response to drugs in actual three-dimensional (3D) tissue environments.

Stimulated Raman scattering (SRS) microscopy is a powerful label-free chemical imaging technique with 3D subcellular spatial resolution.[69] It has demonstrated its great potential in visualizing protein and amino acids metabolism by combining with deuterium labeling in previous studies.[72,73,171,172] Specifically, Wei et al. reported that deuterium amino acids are generally non-perturbative to live cells and can be used for spatial mapping of newly synthesized proteomes in cells and tissues.[72,73] Miao et al. showed that deuterium-labeled glutamine enables imaging of protein aggregation in Huntington's disease.[171] Spratt et al. demonstrated the visualization of deuterated methionine incorporated into Drosophila tissue *in vivo*.[173] These applications collectively verified the qualitative capability of SRS microscopy in investigating protein and amino acid metabolism in cells and tissues both *in vitro* and *in vivo*. Furthermore, SRS microscopy has shown its capability in rapid antimicrobial susceptibility testing by measuring deuterium oxide (D_2O) metabolic incorporation at the single-bacterium level.[174–178] It is important to note that while both biosynthetic and uptake pathways can be used for deuterium labeling, quantitative analysis requires well-defined pathways with no or minimal competing reactions that depend on the cell microenvironment.

In this work, we leveraged the quantitative capability of SRS to further extend this technique for quantifying single-cell growth rates at high throughput by using selected deuterated amino acids as metabolic tracers. We chose three branched-chain essential amino acids, leucine, isoleucine, and valine (LIV), for deuterium labeling. Cell organisms cannot synthesize these essential amino acids endogenously and can only uptake them from the cell culture medium for protein synthesis. Moreover, these three amino acids are the most abundant in cell proteome, accounting for ~20% of all amino acids.[179] They all contain $–CD_3$ groups, which give well-defined Raman peaks around 2100 cm^{-1} and are chemically stable. As the cells grow in the cell culture medium supplemented with deuterated LIV (d-LIV), cells uptake the d-LIV and incorporate carbon–deuterium (C–D) bonds in their newly synthesized protein. As a result, the ratio between the deuterium-labeled proteins and the total unlabeled proteins accurately indicates the protein synthesis rate of each individual cell. With our ratiometric C–D/carbon–hydrogen (C–H) SRS imaging system, we simultaneously measured the C–D SRS signal from the deuterium-labeled proteins and the C–H SRS signal from unlabeled proteins to determine the cellular protein synthesis rate at a single-cell level. We demonstrate that this technique enables single-cell level drug testing for both 2D and 3D cells. The submicron resolution of SRS imaging allows us to closely examine the effects of different drugs on cell growth rate and morphology. We believe that our method is valuable for investigating cell-drug interactions in various types of cancer cell lines, tumor models, and patient-derived samples.

3.2 MATERIALS AND METHODS

3.2.1 *Simultaneous dual-band SRS imaging*

The simultaneous dual-band SRS microscopy setup has been reported in detail in Chapter 2.[100] Briefly, the output of a broadband femtosecond oscillator (Light Conversion FLINT-FL2) with a center wavelength of 1030 nm is split into two beam paths; one beam serves as the Stokes beam, and the other is used for pumping two tunable optical parametric oscillators (OPOs). The two synchronous OPO outputs serve as pump beams and interact with the Stokes beam to simultaneously excite two vibrational frequency bands. For C–D/C–H ratiometric imaging, we tuned the two OPO output wavelengths to 848 nm and 790 nm for simultaneous collection of SRS images at 2125 cm^{-1} and 2930 cm^{-1}, respectively.

The three synchronized laser beams were directed into a homebuilt upright laser scanning microscope system equipped with a 40X water immersion objective (Nikon N40XLWD-NIR, NA = 1.15) and an oil immersion condenser (Nikon MEL41410, NA = 1.4). For simultaneous dual-channel SRS imaging detection, the two pump beams are isolated and detected by two amplified

Si photodiodes (PD). The signals detected by both PDs are demodulated with a multi-channel lock-in amplifier (LIA, Liquid instruments Moku:Pro) with a time constant of 4 μs to generate 512 × 512 pixel SRS images with a pixel size of 0.39 μm/pixel. The system also allows us to collect hyperspectral SRS images at the two vibrational frequency regions by translating a motorized stage (Zaber X-DMQ-AE) that controls the interpulse delay between the Stokes beam and the pump beams.

For simultaneous C–D and C–H SRS imaging of cells and spheroids, 40 mW of C–D pump beam at 848 nm, 40 mW of C–H pump beam at 790 nm, and 150 mW of Stokes beam at 1030 nm were used. The average of 4 SRS images collected with a pixel dwell time of 3.2 μs was calculated for signal and ratio quantification.

3.2.2 *2D cell culture*

The human lung adenocarcinoma cell line, A549 cells (ATCC), were maintained at 37°C in a humidified 5% CO_2 incubator and cultured in Dulbecco's modified eagle medium (DMEM, Gibco) supplemented with 10% fetal bovine serum (Hyclone) and 1% penicillin-streptomycin (Gibco). For fixed cell imaging, the cells were seeded on glass coverslips overnight and fixed with 4% paraformaldehyde (PFA) solution for 15 minutes.

3.2.3 *3D spheroid culture*

The A549 cell line was first cultured in F-12K (Gibco) medium supplemented with 10% FBS (Hyclone) and 1% penicillin-streptomycin (Gibco) prior to the 3D spheroid culture. The cells were washed twice with PBS and detached from the dish with 0.25% trypsin (Gibco). The cells were centrifuged at 200 xg for 5 minutes at room temperature and resuspended in 5 mL medium. The cellular suspension was diluted to 10,000 cells/mL. The diluted cellular suspension was transferred into each well of the 96-well low-attachment culture plate (Corning) to achieve 2,000 cells/well. The culture plate was centrifuged at 200 xg for 3 minutes at room temperature and incubated at 37°C in a humidified 5% CO_2 incubator. The cell culture medium was exchanged to DMEM after 48 hours. The spheroids were fixed with 4% PFA solution for 20-30 minutes following drug treatment and deuterium labeling. The fixed spheroids were then transferred onto a microscope slide and sandwiched with glass coverslips using ~200-300 µm-thick tapes. Imaging of the spheroids was performed at a depth of 60 µm.

3.2.4 *Deuterium labeling*

Deuterated L-leucine-d_{10}, L-isoleucine-d_{10}, and L-valine-d_8 (Cambridge Isotope Laboratories) were supplemented into LIV-deficient DMEM medium (Boca Scientific) at a concentration of 0.8 mM. This concentration was chosen to match the concentrations of these amino acids in regular DMEM to achieve a full deuteration. To perform deuterium labeling, the cell culture medium was changed from the regular DMEM to the d-LIV supplemented medium, followed by incubation at 37°C for the desired labeling time.

3.2.5 *Drug treatment*

Gefitinib (Selleckchem), lapatinib (Selleckchem), paclitaxel (Sigma-Aldrich), and etoposide (Sigma-Aldrich) were dissolved in dimethyl sulfoxide (DMSO) to make 10 mg/mL stock solutions. The stock solutions were diluted with cell culture medium to the desired concentrations for drug treatment. A549 cells were seeded on coverslips for 1 day before being treated with the tested drug. Control cells were treated with DMSO only. Drug solutions were prepared using the d-LIV supplemented medium for deuterium labeling. After incubation, cells were immediately fixed for SRS imaging.

3.2.6 *MTT viability assay*

A549 cells were seeded in 96-well plates for 48 hours before incubation with drugs for 24 hours. After treatment, the cells were incubated with serum-free media and MTT reagent (Abcam ab211091) for 3 hours. We then added MTT solvent (Abcam ab211091) into each well after incubation and shook the plates on an orbital shaker for 15 minutes. The absorbance measurements were collected at 590 nm using a UV/visible microplate reader (Thermo Labsystems Multiskan Spectrum).

3.3 RESULTS AND DISCUSSION

We first validated that the deuterated amino acids do not induce toxicity to the cancer cells and the modification of LIV to their deuterated version does not affect cell growth rates. We performed the MTT cell viability assay on cells grown in regular DMEM and d-LIV supplemented DMEM for 24 hours and 72 hours. There was no statistically significant difference between the two groups for either incubation duration (Figure 3.1), which verified that the cell growth and proliferation rates were not altered by the replacement of the three amino acids.

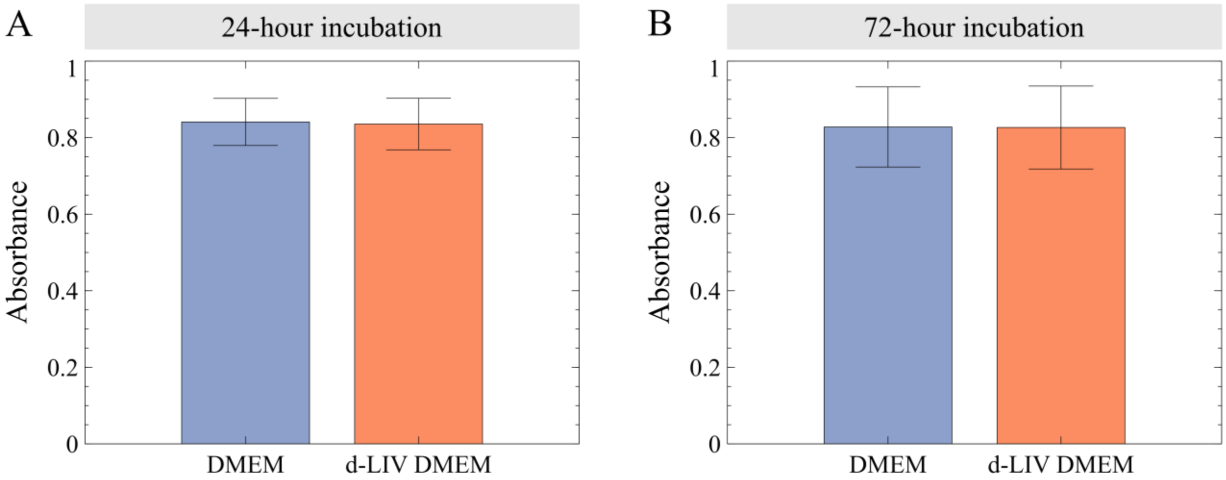

Figure 3.1. MTT assay absorbance measurements of A549 cells cultured in regular DMEM and d-LIV supplemented DMEM media for 24 hours (A, *n* = 16) and 72 hours (B, *n* = 24). There

is no statistically significant difference between the two groups with either 24-hour or 72-hour incubation.

The SRS spectra of the d-LIV solution at different concentrations in the 2000 – 2300 cm^{-1} vibrational frequency band are shown in Figure 3.2A. The three amino acids all have similar peaks in this cell-silent region of the Raman spectrum due to symmetric and asymmetric stretching of C–D bonds.[72] We selected the middle vibrational peak at 2125 cm^{-1}, indicated by the blue shaded line, for on-resonance C–D SRS imaging due to its highest signal intensity. To remove the non-Raman background signal arising from a cross-phase modulation process, we selected 2030 cm^{-1} (gray-shaded line) as the off-resonance frequency.[180] The background-corrected d-LIV solution SRS signal intensity showed a good linear dependence on the d-LIV concentration with an $R^2 = 0.9988$, as demonstrated in Figure 3.2B, which confirmed the high-accuracy quantification capability of SRS microscopy.

We then performed ratiometric SRS imaging on A549 cells grown in d-LIV supplemented culture medium for different time pulses from 0 hours (unlabeled) to 72 hours. To calculate the C–D/C–H SRS ratio of each cell, we first created cell masks by thresholding the C–H SRS image at 2930 cm^{-1}, the protein peak in the C–H stretching region, and segmenting adjacent cells with the watershed algorithm. The average C–H signals of each cell were calculated from the 2930 cm^{-1} SRS images, and the background-corrected C–D signals were calculated as $I_{\text{C–D}} = (I_{\text{on}} - I_{\text{on,bg}}) - (I_{\text{off}} - I_{\text{off,bg}})$, where $I_{\text{on,bg}}$ and $I_{\text{off,bg}}$ are non-cellular region background intensities at the on and off-resonance frequencies, respectively. The average C–D and C–H signals of each cell were then divided to generate the SRS ratio values. We plotted the C–D/C–H SRS ratios of cells labeled for different time pulses in Figure 3.2C. During the first 8 hours after the cells were exposed to the d-LIV supplemented cell culture medium, the average C–D/C–H SRS ratios increased linearly, as shown in Figure 3.2D, with an R^2 value of 0.9993. During this period, deuterated LIV amino acids replace the non-deuterated LIV amino acids as the cells grow and synthesize new proteins. After the cells grew in the d-LIV supplement medium for a while, deuterated LIV would replace both deuterated and non-deuterated amino acids, causing the C–D/C–H SRS ratio increase rate to slow down. Eventually, the C–D/C–H ratio in cells saturates at a level that matches the average fraction of the three amino acids in proteins. The C–D/C–H SRS ratio determined with A549 cells grown in the deuterium-labeled medium for 72 hours closely represents the saturation level, as the cells had proliferated for three generations.

The representative C–D and C–H SRS images of A549 cells labeled with d-LIV for 4 hours and 72 hours are demonstrated in Figure 3.2E, F, H, I with the same color contrast. The SRS spectra shown in Figure 3.2G validate that the C–D signal in cells corresponds to the incorporated d-LIV. Compared to the 4-hour d-LIV labeled cells, the 72-hour d-LIV labeled cells have a slightly lower C–H protein peak at 2930 cm^{-1}, as shown in Figure 3.2J. This signal decrease indicates the deuteration of the LIV amino acids.

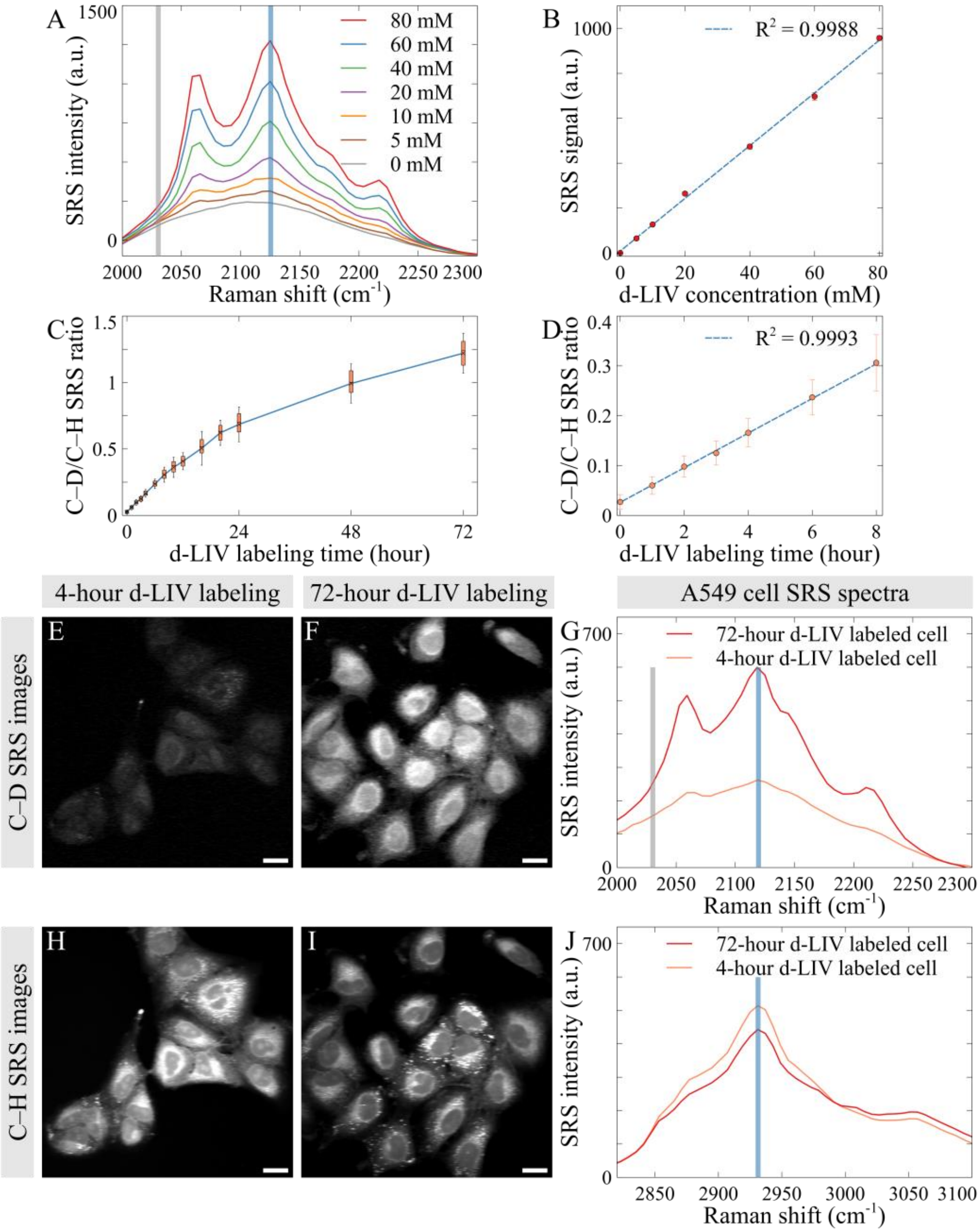

Figure 3.2. C–D/C–H ratiometric SRS imaging of d-LIV solution and A549 cells grown in d-LIV supplemented culture medium. (A) C–D region SRS spectra of d-LIV solution of different concentrations. (B) Linear regression of background-corrected d-LIV solution signal intensity at different concentrations with the R^2 value and standard deviations as error bars. (C) Single-cell C–D/C–H SRS signal ratios of A549 cells labeled with d-LIV for different time pulses. (D) Linear regression of average C–D/C–H SRS signal ratio of A549 cells labeled with d-LIV for short time pulses, 0 to 8 hours. (E-F) Representative background-corrected C–D SRS images of A549 cells labeled with d-LIV for 4 hours and 72 hours. (G) A549 cell SRS spectra in the C–D spectral region.

(H-I) Representative 2930 cm^{-1} C–H SRS images of A549 cells labeled with d-LIV for 4 hours and 72 hours. (J) A549 cell SRS spectra in the C–H spectral region. Scale bar: 20 µm.

With the simultaneous dual-band SRS imaging system, it takes less than 1 second to collect a pair of C–D and C–H SRS images. To improve the accuracy of cell signal measurements, we averaged 4 frames of SRS images to reduce the noise level. As a result, it takes 3.4 seconds to image one field of view, which on average captures >10 cells. This technique provides a method to perform fast, high-content drug testing by probing single-cell growth rate responses. To validate the drug testing performance of the system, we treated A549 cells with a targeted cancer drug, gefitinib (Gef), at varying concentrations from 0.2 µM to 300 µM for 24 hours. During the last 4 hours of the drug treatment, the cells were incubated in d-LIV supplemented medium with drugs for deuterium labeling. We measured the C–D/C–H SRS ratio >200 cells under each treatment condition (Figure 3.3A) and compared the results to the well-established MTT cell viability assay (Figure 3.3B). We observed that the trend of cellular response to the increasing concentration of Gef agrees well between the two methods. Drug-induced growth rate inhibition, in contrast to traditional pharmacometrics, such as IC_{50} and EC_{50} values, is largely independent of cell division rate, culturing condition, and assay duration, and therefore provides a more robust cell response measurement.[156] We calculate the drug concentration at which the cell growth rate is reduced by half (GR_{50}) to be 14.7 µM based on a sigmoidal fitting on the SRS measurements. The GR_{50} value is 18.8 µM when determined by the MTT assay using a method reported by Hafner et al.[156] It has been well-studied that gefitinib competes with ATP for binding to the kinase domain of epidermal growth factor receptor (EGFR) in cancer cells and consequently inhibits autophosphorylation and the activation of downstream signaling pathways, leading to inhibition of cell growth and induction of apoptosis.[181,182] The correlation between the GR_{50} values measured by our SRS method and the cell viability assay agrees with the gefitinib mechanism of action. It is important to note that, despite this correlation, cell growth rate and cell viability are two distinct measurements of cell behavior. Cell viability is a combined quantification of cell number and metabolism activity. Reduced cell viability could indicate either cell death or slower metabolism. In contrast, the SRS method dissects the measurement to solely quantify cell growth, which is a more targeted and precise marker for accessing drug efficacy.

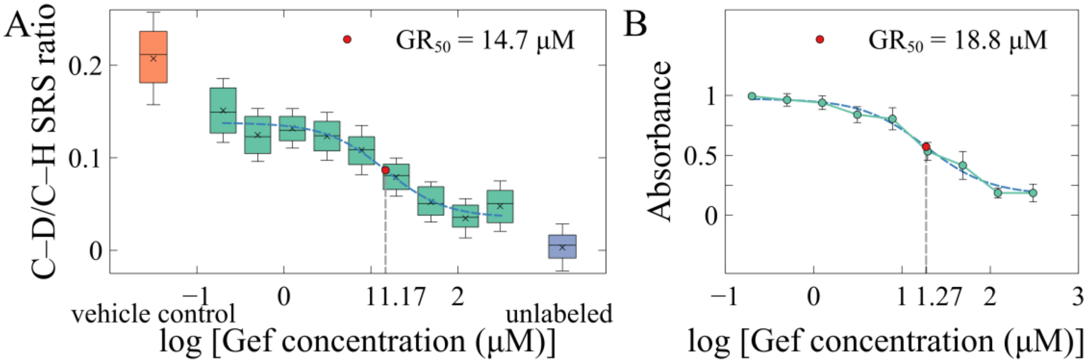

Figure 3.3. A549 cells were treated with different concentrations of gefitinib (Gef) for 24 hours. (A) C–D/C–H SRS ratios of A549 cells with 4-hour d-LIV labeling. Vehicle control: A549 cells treated with DMSO only. Unlabeled: untreated A549 cells grown in regular DMEM. (B) MTT cell proliferation assay absorbance measurements of A549 cells treated with Gef.

In drug discovery, it is desirable to have a drug testing technique with a short turnaround time. Most cell viability assays require 24 – 72 hours of incubation for reliable measurements. The cell growth rate provides a more sensitive response than cell proliferation, which can be used for rapid drug testing. We treated A549 cells with different types of drugs, including two kinase inhibitors, gefitinib and lapatinib (Lap), a mitotic inhibitor, paclitaxel (Pac), and a topoisomerase II inhibitor, etoposide (Eto), at varying concentrations for 12 hours with 4-hour d-LIV labeling and reported the SRS measurements as violin plots in Figure 3.4. All treatments show significant changes in the cell C–D/C–H SRS ratios with increasing drug concentrations. These results confirm that 12 hours is sufficient to quantify cellular response to drugs. It is possible to further shorten drug testing to 4 hours by simultaneously starting drug treatment and d-LIV labeling. In contrast to the bulk measurements provided by cell viability assays, the single-cell level growth rate quantification allows us to discover potential subpopulation differences in cell response under drug treatments. For instance, around half of the A549 cells dosed with 5 µM of Lap had largely reduced cell growth rates, while the other half maintained regular cell growth, as indicated by the large variation in their C–D/C–H SRS ratios in Figure 3.4A. This heterogeneity in cell responses could be a result of inadequate drug exposure or varying drug uptake, potentially leading to the development of drug resistance.

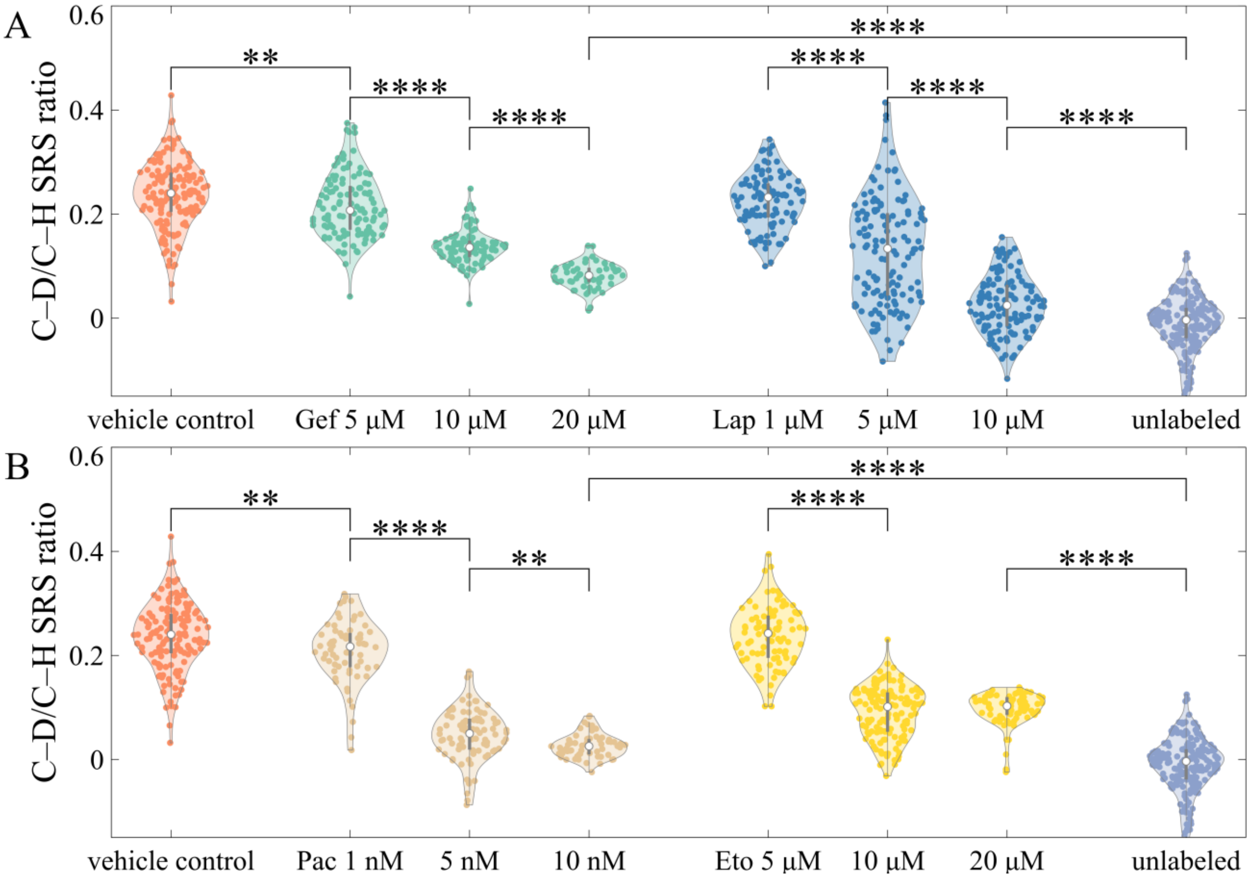

Figure 3.4. C–D/C–H SRS ratio of A549 cells treated with (A) gefitinib (Gef), lapatinib (Lap), (B) paclitaxel (Pac), and etoposide (Eto) of different concentrations for 12 hours with 4-hour d-LIV labeling. Significance: **: $p \leq 0.01$, ****: $p \leq 0.0001$.

Another valuable advantage of our technique compared to traditional bulk assay is that SRS microscopy enables visualization of cell morphology at a submicron resolution. Cell morphology contains rich information that can be used for classifying cell types and cell states.[183–186] By examining the morphology of A549 cells treated with 5 μM of Lap, we observed that approximately half of the cells exhibited apoptotic features such as shrinkage and rounding, while the other half maintained a healthy morphology. This heterogeneity in cell morphological changes aligns with the substantial variation in their growth rate measurements, indicating diverse population responses during this treatment. Moreover, morphological changes caused by drug treatment can provide insights into the drug mechanism of action. To illustrate the various morphological changes induced by different drugs, we show representative C–H SRS images at 2930 cm^{-1} of A549 cells treated with DMSO (Figure 3.5A) kinase inhibitor (Figure 3.5B), mitotic inhibitor (Figure 3.5C), and topoisomerase II inhibitor (Figure 3.5D).

Cell shrinkage was a prominent morphological feature of A549 cells after treatment with gefitinib, as shown in Figure 3.5B, which matches the previously reported morphological changes of cells dosed with protein kinase inhibitors.[187] When treated with paclitaxel, a mitotic inhibitor, a large portion of cells were rounded as they entered the mitosis (M) phase of the cell cycle, followed by a mitotic arrest.[188,189] We also observed blebbing of some cells, as indicated by red arrows in Figure 3.5C, which is likely an indication of cell necrosis induced by mitotic catastrophe.[190] Significant cell shrinkage and reduced signals from cell nuclei were found in A549 cells treated with etoposide, as demonstrated in Figure 3.5D. The cell nucleus signal loss is likely caused by the DNA fragmentation induced by etoposide, which targets DNA topoisomerase II activities.[191,192] These morphological features provide additional insights into single-cell drug response besides growth rate inhibition.

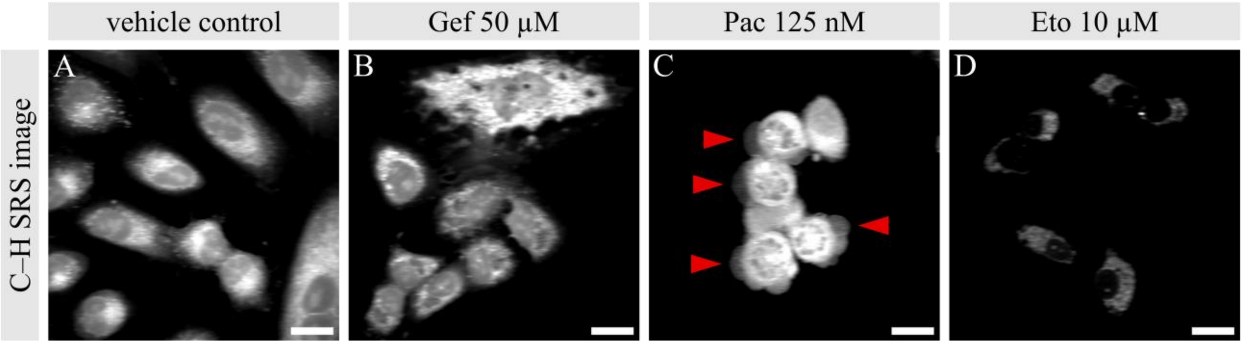

Figure 3.5. Representative 2930 cm^{-1} C–H SRS images of A549 cells treated with (A) DMSO as vehicle control, (B) 50 µM gefitinib, (C) 125 nM paclitaxel, or (D) 10 µM etoposide. Scale bar: 20 µm. Red arrows: cell blebbing.

Although 2D cell culture is widely used for fundamental biological and disease studies, it does not represent the complex microenvironment of actual tumor tissues.[193] Cells grown in a 3D environment exhibit different morphology, proliferation, differentiation, and cell-cell and cell-matrix interaction features compared to monolayer-cultured cells.[194,195] Growing evidence suggested that 3D cell culture systems are more reflective of the *in vivo* tissue environments and thus provide better models for drug screening studies.[196–198] Here, we demonstrate the capability of our ratiometric C–D/C–H SRS imaging system for quantifying the growth rates of 3D spheroid cells. The representative SRS images of an A549 spheroid labeled with d-LIV for 12 hours are shown in Figure 3.6A-B. In single-channel SRS images, the boundary of the spheroid has higher SRS signals than the inner region due to light scattering and sample-induced aberration.[199] This problem can be addressed with ratiometric SRS imaging by which the signal gradient is canceled out between the two channels. We can visualize the growth rate differences between cells in the same spheroid by generating the C–D/C–H ratiometric image, as demonstrated in Figure 3.6C. It is interesting to note that there are substantial growth rate variations within the spheroid, which suggest phenotypic differences that could lead to differences in drug response. We compared the growth rate difference of A549 cells in 2D monolayer culture versus 3D spheroid culture with 12-hour d-LIV labeling in Figure 3.6D and discovered that 3D cultured cells have lower growth rates. This result is consistent with previous studies showing that tumor cells have higher proliferation rates in 2D monolayers than in 3D, caused by their different gene and protein expression profiles.[196,200,201]

To evaluate the performance of ratiometric SRS imaging for drug testing in 3D cell environments, we treated the A549 spheroids with different concentrations of gefitinib, ranging from 2 μM to 100 μM, for 12 hours coupled with 12-hour d-LIV labeling. We report the single-spheroid C–D/C–H SRS ratios in Figure 3.6E. As the concentration of the drug increases, the average spheroid cell growth rate significantly decreases, reflecting the cellular responses to the treatments. A549 spheroids treated with a concentration higher than 100 μM started dissociating and shattering and therefore were not included in drug response quantification. We included the vehicle control and untreated spheroids to estimate the GR_{50} concentration of A549 spheroids treated with gefitinib for 12 hours as 104.8 μM, which is significantly higher than 2D cultured cells. Previous studies have shown that drug efficacy decreases in 3D cultured cells compared to 2D cells due to differences in various cellular factors, including cell survival pathways, EGFR and EMT-associated protein expression, HER-family drug target expression, and mTORC1 signaling activity.[202–204] These differences highlight the importance of developing techniques with the capability to quantify 3D cellular growth rates for investigating cell-drug interactions in complex multicellular environments.

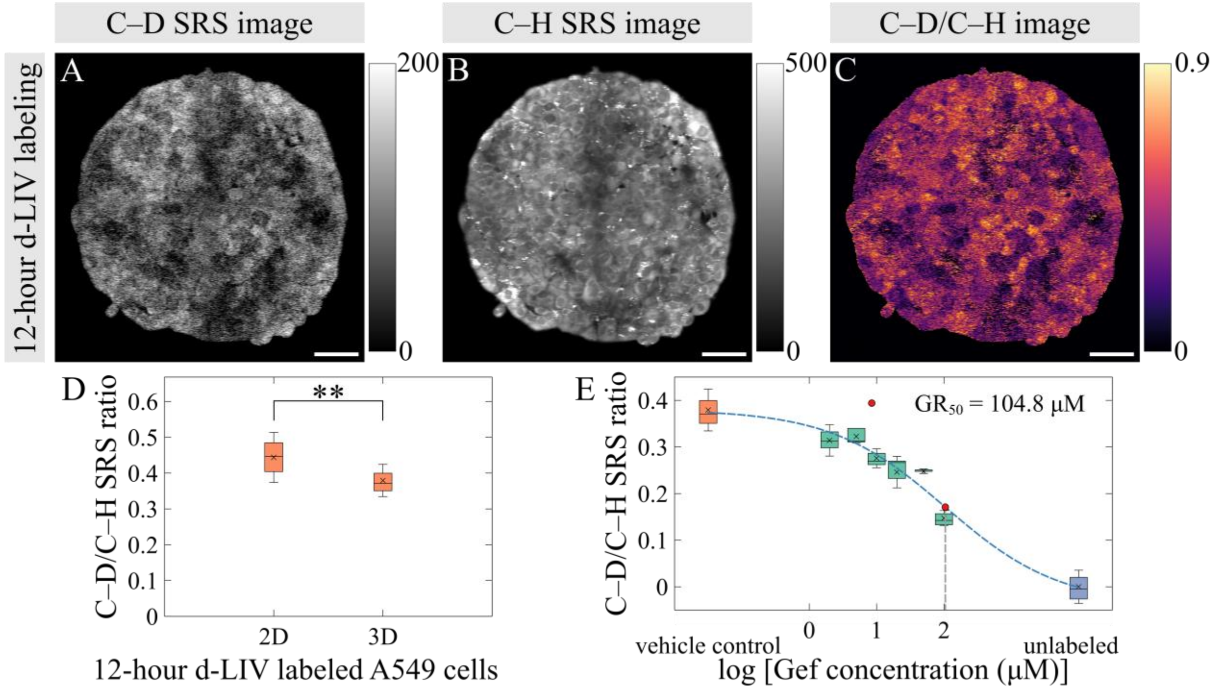

Figure 3.6. Representative (A) C–D, (B) C–H, and (C) C–D/C–H ratiometric SRS images of an A549 spheroid with 12-hour d-LIV labeling. (D) Growth rate comparison of A549 cells cultured in 2D versus 3D. Significance: **: $p \leq 0.01$. (E) C–D/C–H SRS ratio of A549 spheroid cells treated with different concentrations of gefitinib for 12 hours with 12-hour d-LIV labeling. Scale bar: 50 μm.

3.4 CONCLUSIONS

Intra-tumoral heterogeneity plays a vital role in drug resistance development during cancer treatments, suggesting the need to measure drug exposure and response at the single-cell level. In this work, we report a method for visualizing and quantifying cell-drug interaction by measuring cell growth rates using ratiometric SRS microscopy and deuterium labeling. We replace three essential amino acids, leucine, isoleucine, and valine, with their deuterated version in the cell culture medium and assess cell protein synthesis rates by quantifying the ratio between the number of incorporated C–D bonds and the total number of C–H bonds. A simultaneous dual-band SRS imaging system is employed to improve ratiometric analysis accuracy and image acquisition speed.

In this study, we validated the drug testing capability of our system by comparing cell responses to drug treatments measured with ratiometric SRS imaging to the well-established MTT cell viability assay. We also showed that the reported technique allows rapid drug response measurements with a short turnaround time of <12 hours. During drug testing with a high dosage, a portion of apoptotic cells was washed away during fixation, which leads to a biased measurement towards higher average cell growth measurement. This problem can be avoided by performing live cell SRS imaging at lower optical power at the sample. It is important to note that our method focuses on cell growth rate measurement, which is a critical and complementary metric to cell proliferation measurement. Our method can be combined with cell viability or proliferation assays for a more comprehensive characterization of cellular response to drugs. In addition, deep learning algorithms can be adapted to enhance the signal-to-noise ratio of collected SRS images to optimize drug response measurement sensitivity and accuracy.[142] Furthermore, deuteration of all amino acids has been reported to provide higher C–D SRS signals[73], which can shorten the deuterium labeling and drug treatment time. However, a high deuterium content in the cell culture medium can reduce cell viability and metabolic activity due to the kinetic isotope effect.[205] A careful assessment of the cytotoxicity effects of deuteration of all amino acids is crucial for accurately measuring cell growth rates. Moreover, the deuteration of non-essential amino acids may introduce variations in cell incorporation rates, as cells can synthesize these non-essential amino acids from other nutrients, potentially leading to inaccuracies in cell growth rate quantification.

The submicron resolution imaging capacity of ratiometric SRS microscopy provides single-cell morphological information in addition to the cell growth rate measurements. We compared cells treated with different types of chemotherapeutic drugs and demonstrated that the cell morphological changes deliver valuable insights into the drug mechanism of action. Leveraging morphological information, it is possible to examine drug response in co-cultured models by combining C–D/C–H SRS imaging with cell-type classification machine learning or deep learning algorithms.[206,207]

Lastly, the C–D/C–H ratiometric SRS imaging system is capable of quantifying cell growth in a 3D cellular environment. We note that the spheroids were imaged at a depth of 60 µm in this study. The imaging depth was limited by the tissue scattering and system sensitivity. Tissue-clearing methods can be utilized to greatly enhance the imaging depth and achieve a volumetric growth rate quantification of the entire spheroids.[208] The 3D imaging capability of our technique enables further studies of cell-drug interactions in the actual tumor environments. By switching to an epi-detection setup, we can potentially measure *in vivo* cell growth rate and drug response in live animals. Overall, our reported ratiometric SRS imaging system, coupled with deuterium amino acids labeling, provides a valuable tool for rapid high-content quantification of single-cell growth rate and visualization of cell morphological changes in various 2D and 3D cell and tissue environments. Monitoring cell-cell and cell-drug interactions in complex cell models or in vivo tumor models can provide deep insights into the drug resistance development mechanism in cancer treatment.

CHAPTER 4. ASSESSING DRUG UPTAKE AND RESPONSE DIFFERENCES IN 2D AND 3D CELLULAR ENVIRONMENTS USING STIMULATED RAMAN SCATTERING MICROSCOPY

The work presented in this chapter has been published in the following article[209]*:*

Xu, F. X.; Sun, R.; Owens, R.; Hu, K.; Fu, D. Assessing Drug Uptake and Response Differences in 2D and 3D Cellular Environments Using Stimulated Raman Scattering Microscopy. *Anal. Chem.* **2024**, *96* (36), 14480–14489. https://doi.org/10.1021/acs.analchem.4c02592.

4.1 INTRODUCTION

Two-dimensional (2D) monolayer cell culture has traditionally been used for biological studies and drug screenings in vitro due to its simplicity and cost-effectiveness. However, 2D cell cultures are insufficient for capturing the in vivo tumor response during drug treatment, and three-dimensional (3D) cell cultures offer more intricate and representative models.[210] Analogous to in vivo tissue such as tumors, proliferating, quiescent, and necrotic cells coexist within 3D spheroids.[196,211] Additionally, spheroids have been reported to have similar growth dynamics to solid tumors.[212,213] As a result, in recent years, 3D cell cultures have emerged as increasingly popular models for drug screening and cancer treatment.[214] The more complex cell-cell and cell-matrix interactions and nutrient and oxygen gradients in 3D microenvironments result in distinct cellular structures, metabolic activities, and gene expression profiles from 2D cells.[201,203,204,215,216] The differences between 2D and 3D cells can lead to varied cellular responses to drug treatments; specifically, it has been reported that 3D-cultured cells generally exhibit higher resistance to drugs.[196]

The molecular mechanisms underlying the increased resistance in 3D cells are not fully understood, yet several hypotheses have been proposed: the extracellular matrix and cell-cell interactions within the 3D microenvironment may create physical barriers that impede drug penetration[198,217]; nutrient and oxygen availability disparities may alter cellular metabolism and survival pathways[196,218,219]; different gene expression and activation of signaling pathways may promote cell survival and drug efflux[203,201,200]; and the higher cell heterogeneity and microenvironmental gradients may lead to a selection of more resistant cell populations[220,221] Various techniques, notably genetic, transcriptomic, and proteomic analyses, have been employed to dissect these complex mechanisms. These methods, including gene expression analysis, Western blot, and multi-omics approaches, collectively identified diverse gene expressions, signaling pathways, and metabolic processes, including EGFR and EMT-associated protein expression, HER-family drug target expression, and AKT–mTORC1 signaling, that are significantly different between 2D and 3D cells and are potentially associated with reduced drug efficacy in 3D.[202–204,222–228] While these techniques deliver essential insights into the potential causes of drug resistance evolvement, intracellular drug exposure within the complex 3D culture models, a key factor that determines heterogeneous cell response, has rarely been evaluated with existing techniques. Thus, it is crucial to integrate information gained from these methods with techniques that provide spatially resolved molecular profiling.

Existing techniques for directly measuring intracellular drug concentration in 3D environments are limited. Current studies largely depend on biochemical assays, which provide bulk measurements that may overlook variability in drug uptake between individual cells and their complex spatial interactions within spheroids.[229–231] Mass spectrometry imaging has also been utilized to map drug distribution in spheroids and tissues.[232–235] However, the method requires extensive sample preparation and cryosectioning, limiting its applications for live-spheroid imaging and cellular dynamic studies. The lack of precise 3D drug quantification could significantly hinder our understanding of in vivo drug efficacy. Typically, drug exposure within a tumor is assumed to be equivalent to plasma concentration; however, uneven or reduced drug exposure can lead to decreased treatment efficacy and the emergence of drug resistance.[236–238] Moreover, correlating drug concentration measurement with cellular response inhibition can be highly beneficial for understanding drug-cell interactions and resistance development mechanisms.

Recently, stimulated Raman scattering (SRS) microscopy has shown great potential in both directly quantifying intracellular drug uptake and measuring single-cell growth rate as an indicator of drug response.[146,239] In particular, Wong et al. leveraged the well-established lysosomotropic effect, in which the acidic environment in cell lysosomes protonates the weakly basic drugs and enriches drug molecules, and performed live cell hyperspectral SRS imaging in the fingerprint region to visualize and quantify drug uptakes in 2D-cultured cells.[239] However, the compatibility of this technique with 3D cells has not been explored. Due to light scattering, the quantification of drug concentration becomes a challenge. Meanwhile, as reported in the previous chapter, we employed deuterated amino acids, leucine, isoleucine, and valine (d-LIV), as tracers and measured the ratio of carbon–deuterium (C–D) SRS signal from deuterium-labeled proteins and the carbon–hydrogen (C–H) SRS signal from unlabeled proteins to determine the cell growth rate of 2D and 3D cells.[146] However, this method has only been applied to fixed cells.

In this work, we present a robust, noninvasive three-band SRS imaging method that integrates the measurements of drug uptake and cellular response of live cells across 2D and 3D microenvironments. By collecting SRS images in the C–D, C–H, and fingerprint spectral regions, we report the drug uptake and response differences between cells in 2D and 3D during drug treatments and closely examine the heterogeneous drug penetration and cell response patterns within 3D spheroids. Furthermore, by comparing different 3D spheroid culture methods, we explore the effects of extracellular matrix on drug delivery and cell growth inhibition. Overall, this work introduces a valuable tool for innovative experimental measurements of drug uptake and response differences between 2D and 3D cellular environments. It illuminates the intrinsic differences in the cellular response to drugs under different microenvironments and the contribution of limited drug penetration in 3D to drug resistance. Our findings offer empirical evidence to understand the complex mechanisms of drug resistance development in 3D cell models and have important implications in drug screening assay development as well as cancer therapies.

4.2 MATERIALS AND METHODS

4.2.1 *Three-band SRS imaging*

The hyperspectral SRS microscopy setup has been reported in detail in our previous work.[239] Briefly, a broadband femtosecond dual beam laser system (Spectra-Physics Insight DS+) outputs a wavelength-tunable beam (pump) and a fixed beam at 1040 nm (Stokes) at an 80 MHz repetition rate. The pump beam is chirped to approximately 3 ps with high-dispersion SF11 dense flint glass rods (GR, Newlight Photonics). The Stokes beam is modulated at 20 MHz with an electro-optical modulator (EOM, Thorlabs) and coupled into a 4-m polarization-maintaining Yb-doped fiber (YB1200-10/125 DC-PM, Thorlabs) for parabolic amplification[109], then chirped to approximately 3 ps using a grating stretcher (GS, LightSmyth). The two beams are combined with a 1000 nm short pass (SP) dichroic mirror (Thorlabs) and temporally overlapped using a motorized delay stage (DS, Zaber X-DMQ-AE).

The synchronized laser beams are directed into a home-built upright laser scanning microscope equipped with a 40× water immersion objective (Nikon N40XLWD-NIR, NA = 1.15) and an oil immersion condenser (Nikon MEL41410, NA = 1.4). The pump beam is isolated with a 1000 nm SP filter (Thorlabs) and detected by an amplified Si photodiode (PD). The signal is then demodulated with a lock-in amplifier (LIA, Zurich Instruments H2FLI) with a time constant of 4 μs to generate 512 × 512-pixel SRS images. For SRS imaging of live cells and spheroids, 40 mW of the pump beam at 800 nm for C–H, 858 nm for C–D, and 912 nm for fingerprint region, and 90 mW of the Stokes beam were used.

4.2.2 *2D cell culture*

The human lung adenocarcinoma cell line, A549 cells (ATCC), was maintained at 37 °C in a humidified 5% CO_2 incubator and cultured in Dulbecco’s modified Eagle's medium (DMEM, Gibco) supplemented with 10% fetal bovine serum (Hyclone) and 1% penicillin-streptomycin (Gibco). Cells were seeded at 200,000 cells per coverslip and incubated for 48 hours before drug treatment and deuterium labeling.

4.2.3 *3D spheroid culture*

For scaffold-free spheroid culture, the A549 cell line cultured in DMEM supplemented with 10% FBS and 1% penicillin-streptomycin prior to the 3D spheroid culture was washed twice with PBS and detached from the dish with 0.25% trypsin (Gibco), then centrifuged at 200 × g for 5 min at room temperature and resuspended in medium. The cellular suspension was diluted and transferred into each well of the 96-well low-attachment culture plate (Corning) to achieve 2000 cells/well. The culture plate was centrifuged at 200 × g for 3 min at room temperature and incubated at 37 °C in a humidified 5% CO_2 incubator for 48 hours before drug treatment and deuterium labeling.

For scaffolded extracellular matrix spheroid culture, A549 cellular suspension was counted and diluted to 400,000 cells/mL. Matrigel (Corning) was stored under -20°C and thawed under 4°C overnight prior to use. A one-to-one ratio of Matrigel and diluted cellular suspension was mixed, and 35 μL of the mixture was transferred onto the center of a coverslip. The Matrigel and cell mixture was prepared on an ice block. The coverslip was then inverted so that the Matrigel and cell mixture was at a hanging drop orientation and incubated in a 37°C humidified 5% CO_2 incubator for 30 mins to allow polymerization. Then the coverslip was flipped back, and the Matrigel droplet was cultured with the immersion of DMEM in the incubator for 2-3 weeks before drug treatment and deuterium labeling, during which the culture medium was replaced every 2 days.

4.2.4 *Deuterium labeling for single-cell growth rate measurement*

Deuterated L-leucine-d_{10}, L-isoleucine-d_{10}, and L-valine-d_8 (d-LIV, Cambridge Isotope Laboratories) were supplemented into the LIV-deficient DMEM medium (Boca Scientific) at a concentration of 0.8 mM. This concentration matches the concentrations of these amino acids in regular DMEM to achieve full deuteration. To perform deuterium labeling, the cell culture medium was changed from the regular DMEM to the d-LIV-supplemented medium, followed by incubation at 37 °C for the desired labeling time. Specifically, 2D-cultured cells were labeled with d-LIV for 6 hours before SRS imaging, and 3D-cultured spheroids were d-LIV labeled for 24 hours.

4.2.5 *Single-cell and single-spheroid growth rate quantification*

Chapter 3 reported details on measuring single-cell growth rates with ratiometric SRS imaging.[146] Briefly, d-LIV-labeled cells were imaged at 2125 cm^{-1} in the C–D region to quantify their newly synthesized deuterium-labeled proteins and at 2930 cm^{-1} in the C–H stretching region to measure their total unlabeled proteins. In addition, SRS images at 2030 cm^{-1} were collected as the off-resonance frequency to remove the non-Raman background signal in the C–D SRS images. For 2D-cultured cells, we generated cell masks by thresholding the C–H SRS image and segmenting adjacent cells with the watershed algorithm. For 3D cells, each spheroid was manually segmented using its C–H SRS image. The cell and spheroid masks were then used to calculate C–D/C–H SRS ratios as growth rate measurements.

4.2.6 *Drug treatment for intracellular drug uptake measurement*

Lapatinib (Selleckchem) and paclitaxel (Sigma-Aldrich) were dissolved in dimethyl sulfoxide (DMSO) to make 10 mg/mL stock solutions. The stock solutions were diluted with cell culture medium to the desired concentrations for drug treatment. Control cells were treated with DMSO only. Drug solutions were prepared using the d-LIV-supplemented medium for deuterium labeling. For both 2D and 3D cells, the drug treatment time was 24 hours.

4.2.7 *Intracellular drug uptake quantification*

Details on measuring single-cell drug uptake with fingerprint region hyperspectral SRS imaging have been previously reported.[239] Briefly, live A549 cells and spheroids treated with lapatinib were imaged at the 1300 – 1600 cm^{-1} spectral band, which captures the cell peak at 1450 cm^{-1} and lapatinib peaks. The single-cell or single-spheroid SRS spectrum was extracted with cell or spheroid masks generated from C–H SRS images as described above. A spectral unmixing algorithm was then performed using the lsqr function in MATLAB to determine the linear combination coefficients of cell, lipid droplet, drug, and background solvents. In the previous work, the absolute concentration was determined by comparing the drug signal to calibration. In the presence of light scattering in 3D spheroids, the intracellular drug uptake was quantified as the calculated coefficient of the drug component divided by its cell signal intensity at 1450 cm^{-1}. This normalization step is necessary to remove the contribution of light scattering-induced intensity loss.

4.3 RESULTS AND DISCUSSION

We first validated the capability of measuring both intracellular drug uptake and growth rate inhibition of the same cells in 2D using our three-band SRS imaging system. We selected A549 cells, a non-small-cell lung cancer cell line, as the cell model for this study. We treated the cells with lapatinib (Lap), an FDA-approved tyrosine kinase inhibitor (TKI) for both the epidermal growth factor receptor (EGFR) and human epidermal growth factor receptor 2 (HER2), at varying concentrations for 24 hours. The molecular formula and structure of lapatinib are shown in Appendix A Figure A.1. The SRS images in three different vibrational bands, fingerprint, C–D, and C–H regions, were acquired for 150-300 cells for each treatment. We performed hyperspectral SRS imaging in the 1300 – 1600 cm^{-1} spectral band to quantify the single-cell drug uptake. Representative SRS images and spectra of cells treated with 5 μM of lapatinib were shown in Figure 4.1A-B. Lapatinib has 4 distinct peaks, at 1325, 1360, 1390, and 1535 cm^{-1}, that are well-separatable from the 1450 cm^{-1} cell peak in this region. We detected strong drug signals at its most prominent peak in the imaged spectral region, at 1360 cm^{-1} (Figure 4.1A left), consistent with previous reports that the drug is highly enriched in lysosomes to reach a detectable range.[121,239] However, the drug concentration is not quantifiable from this single SRS image as signals from cells also contribute to this frequency (Figure 4.1B). Leveraging the linear dependence of the SRS signal on chemical concentration, we apply a linear least-squares algorithm on cell spectra to unmix the cellular and drug compositions. To correct for signal variation induced by light scattering, we quantify single-cell intracellular drug uptake by normalizing the drug coefficient to the 1450 cm^{-1} cell peak, resulting from CH_2 deformation of protein and lipid. We plotted 2D cell drug uptake as a function of lapatinib concentrations in Figure 4.1C. We note that the unit of the lapatinib uptake measurement is normalized intensity of the drug/cell ratio. The 2D cells were dosed with up to 10 μM lapatinib only, as higher drug concentrations dramatically diminished cell viability. Overall, as the drug dosage increases, the measured intracellular drug uptake increases as expected, confirming the sensitivity of our method. To confirm that the normalization by 1450 cm^{-1} does not bias results, we also normalized the drug coefficient to the C–H stretching peak at 2930 cm^{-1} and obtained the same trend, as demonstrated in Appendix A Figure A.2A. Although both cell peaks at 1450 cm^{-1} and 2930 cm^{-1} can be used for the normalization, light scattering is wavelength-dependent, and therefore, it is more desirable to use the 1450 cm^{-1} peak despite its higher noise since the same wavelength is used for excitation of the peaks in the fingerprint region.

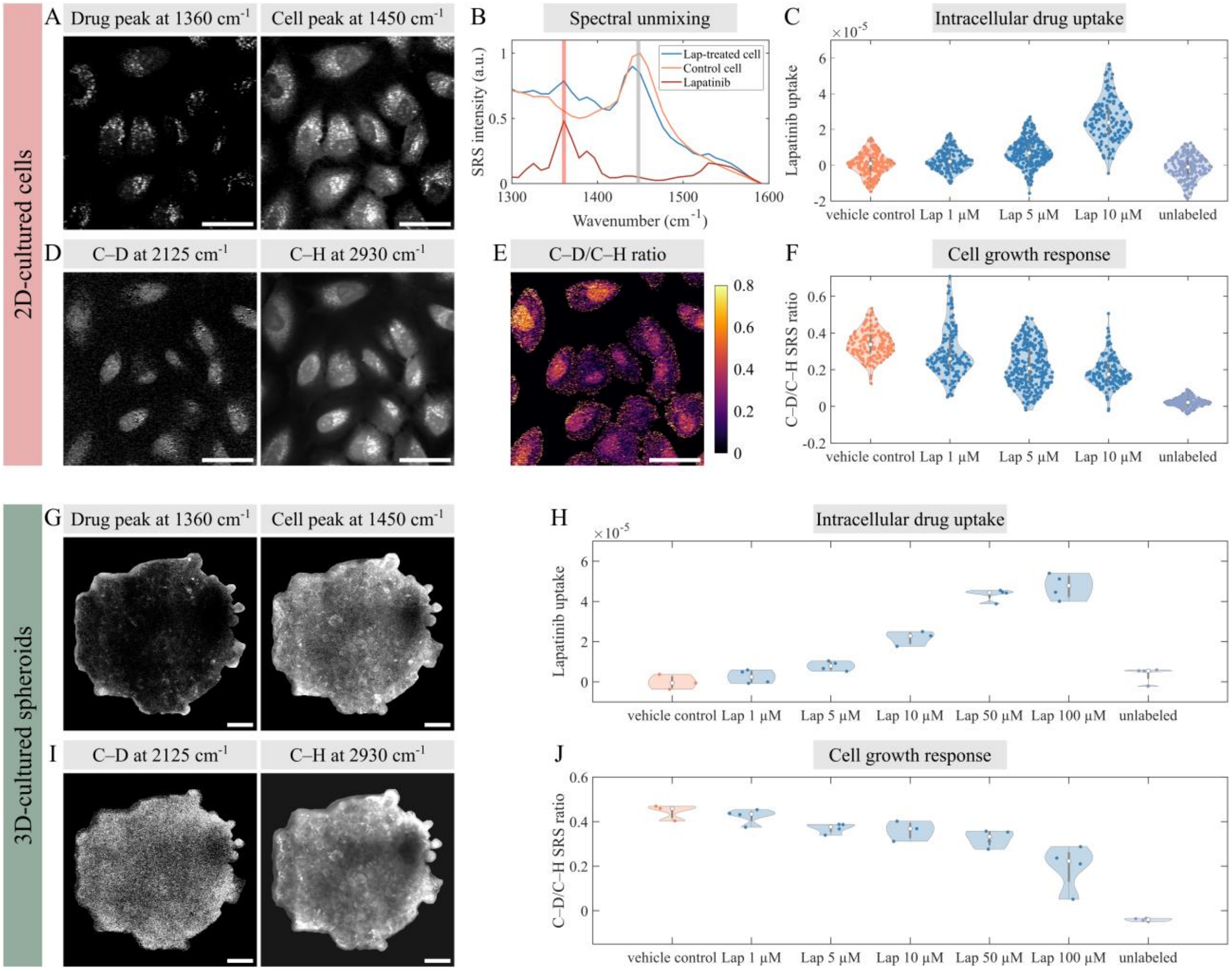

Figure 4.1. Representative SRS images and spectra of live 2D and 3D A549 cells and their intracellular drug uptake and growth rate changes during treatment with a tyrosine kinase inhibitor, lapatinib (Lap). (A) SRS image of 2D A549 cells treated with 5 µM of lapatinib at 1360 cm^{-1}, the most prominent drug peak (red shaded line in B), and at 1450 cm^{-1}, the cell peak (gray shaded line in B). (B) SRS spectra of Lap-treated cells were decomposed into cellular and drug components using a linear least-squares algorithm to measure drug uptakes. (C) The intracellular drug uptake in 2D cells treated with Lap at varying concentrations for 24 hours. (D) SRS images of 2D A549 cells at 2125 cm^{-1} in the C–D region and 2930 cm^{-1} in the C–H region. Their ratiometric image (E) reflects cellular growth rate. (F) The growth rate response of 2D cells labeled with d-LIV for 6 hours under different lapatinib treatments. (G, I) SRS image of 3D spheroid treated with 5 µM of lapatinib at drug, cell, C–D, and C–H peaks. (H, J) Single-spheroid drug uptake and growth rate response under lapatinib treatment of varying concentrations and 24-hour d-LIV labeling. Scale bars: 40 µm.

To measure the single-cell growth rate, we labeled the 2D A549 cells with d-LIV for 6 hours, which provides a sufficient C–D signal-to-noise ratio (SNR) for reliable quantification (Figure 4.1D). Figure 4.1E shows the C–D/C–H ratiometric image that allows visualization of different cell growth rates. The 2D single-cell growth response was plotted as a function of lapatinib concentration in Figure 4.1F. It has been reported that lapatinib significantly reduces various cellular activities in A549 cells, including cell proliferation, DNA synthesis, and colony formation capacity.[240] As the concentration of drug treatment increases, the C–D/C–H ratios decrease, agreeing with the expected growth inhibition.

We then performed the three-band SRS imaging method to quantify drug uptake and growth response in 3D cells. We cultured A549 cells in low-attachment plates to form spheroids and treated the spheroids with up to 100 μM lapatinib. 3-4 spheroids were imaged under each treatment. Representative drug peak, cell peak, C–D, and C–H SRS images of the middle cross-section of a spheroid treated with 5 μM of lapatinib are shown in Figure 4.1G and I. It has been reported that 3D-cultured cells have a slower proliferation rate compared to monolayer cells[196,200,201]; therefore, we performed 24-hour d-LIV labeling on 3D spheroids to obtain a sufficient C–D signal (Figure 4.1I). Different from 2D cell imaging, mosaic tile scans were needed to capture an entire spheroid middle cross-section at a depth of ~120 µm. However, as illustrated in Appendix A Figure A.3A, the field curvature of each field-of-view (FOV) results in obvious stitching artifacts that can greatly reduce the accuracy of our measurements. To address this problem, we generated an FOV normalization mask using cell-free regions for each spectral region. The masks were normalized to have an intensity ranging from 0 to 1. We then divided each tile image by the FOV mask to correct for the field curvature. As shown in Appendix A Figure

A.3B, this FOV normalization method significantly minimizes stitching artifacts and resultant intensity variations.

We observed stronger drug signals around the outer ring of the spheroids and weaker signals in their inner layers (Figure 4.1G). We note that cells in the center of the spheroid experienced much stronger light scattering and sample-induced aberration and thus have lower SRS signals.[199] This is reflected in all four channel images. This problem can be addressed by normalizing the drug uptake measurement to the 1450 cm^{-1} cell peak intensity. The C–D/C–H ratio also normalizes this contribution and provides quantitative single-cell growth measurement. Figure 4.1H and J demonstrate the single-spheroid drug uptake and growth rate response as a function of lapatinib concentration. As the drug dosage increases, the measured intracellular drug uptake increases, and the growth rate decreases. Interestingly, the increase in intracellular drug concentration began to level off at concentrations above 50 μM. As stated above, our SRS method primarily quantifies the intracellular drug uptake through the lysosomotropic effect, and pH-driven lysosomal sequestration is saturable.[241] The intracellular drug uptake level of spheroid treated with 50–100 μM likely indicates saturated lapatinib accumulation. These trends confirm the capability of our SRS method to detect and quantify both 2D and 3D drug uptake and cellular response simultaneously during treatments.

To further investigate differences in drug uptake and cellular response between 2D and 3D environments, we compared the intracellular lapatinib uptake, cell growth rates, and normalized cell growth rates for cells treated with the same concentrations in Figure 4.2. Figure 4.2A demonstrates that intracellular drug uptake levels are similar between single cells cultured in 2D and single spheroids in 3D, with no significant differences observed within each treatment concentration. The same trend was observed when using C–H peak intensity for drug uptake measurement normalization (Appendix A Figure A.2C). To compare growth inhibition differences between 2D and 3D-cultured cells, we adjusted the C–D/C–H ratio of 2D-cultured cells by multiplying it by a factor of 4, accounting for the 4-fold differences in d-LIV labeling duration. As shown in Figure 4.2B, 2D cells have significantly higher growth rates compared to 3D cells under identical treatment conditions. Interestingly, when we compared the relative growth rate changes during drug treatment by normalizing 2D and 3D cell growth rates to the median growth rates of their respective vehicle controls, we found that cells in the 3D environment exhibited higher normalized growth rates than those in the 2D environment, as illustrated in Figure 4.2C. This observation confirms that, with similar levels of drug uptake, the proliferation of 3D-cultured cells is more resistant to lapatinib treatment than their 2D-cultured counterparts, consistent with our observation that 3D cell culture can tolerate much higher concentration lapatinib treatment. This trend aligns with our previous drug response study of A549 cells treated with another TKI, gefitinib, in which the drug dosage that reduces cell growth rate by half increased by ~7-fold from 2D to 3D.[146]

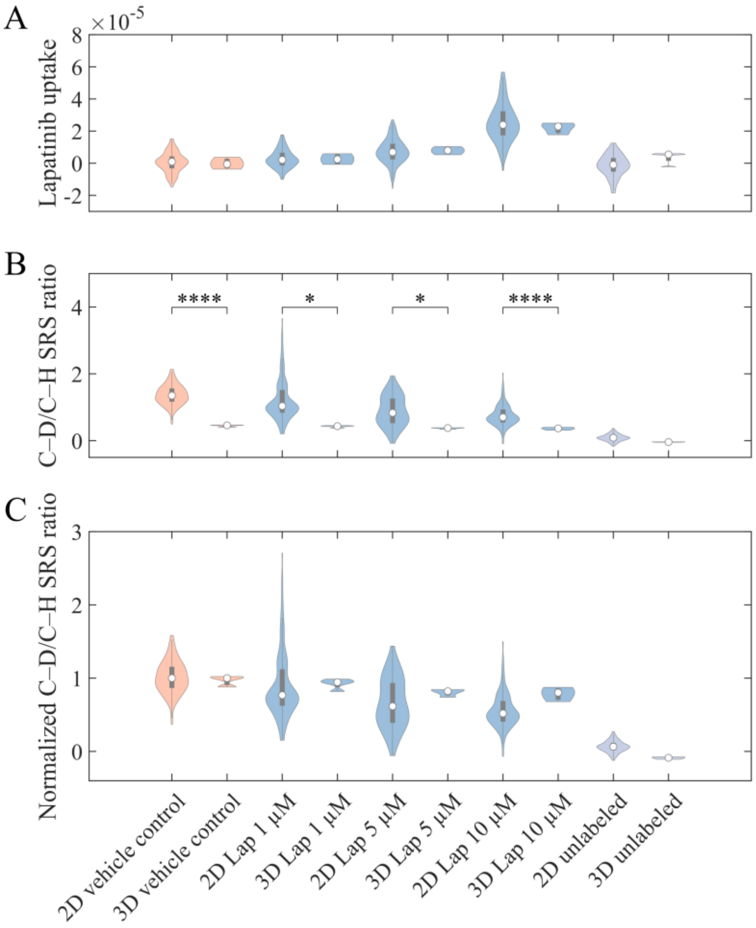

Figure 4.2. Comparison of intracellular drug uptake (A), cell growth rate (B), and normalized cell growth (C) between 2D-cultured cells and 3D-cultured spheroids treated with varying concentrations of lapatinib. Significance determined by Student’s t-test: *: $p \leq 0.05$, ****: $p \leq 0.0001$.

It is important to note that the 3D measurements in Figure 4.2 represent the averaged data from all cells in the imaged cross-section, resulting in much smaller variances compared to 2D measurements. This averaging does not capture the heterogeneity in drug uptake or response of cells within the individual spheroid. To explore potential reasons behind the increased resistance observed in 3D-cultured cells, we examined the correlation between drug penetration and cell response heterogeneity. Given the challenge of segmenting individual cells within each spheroid due to their dense packing and the limited SNR in the spheroid center, we segmented the spheroids into layers to study how the drug diffuses and influences cell responses. Using spheroids treated with 10 μM of lapatinib as an example, we compared their drug uptake and response at different layers against control spheroids. Figure 4.3A shows the drug/C–H ratiometric SRS image of a representative Lap 10 μM-treated spheroid. Such ratiometric images enable direct visualization of drug accumulation and localization within the spheroids. Figure 4.3B provides a zoom-in view of a drug-enriched area. By comparing the ratiometric image with the C–H SRS image, we observed a high spatial correlation between lapatinib accumulation, appearing as bright yellow spots, and cell cytoplasm. We note that the drug uptake measurements were normalized to the 1450 cm^{-1} cell peak. The C–H image was used here only for this visualization because of its higher SNR. Overall, we observed significant aggregations of lapatinib molecules in the outer and middle layers of the spheroid. This observation matches the lapatinib uptake plot in Figure 4.3C. The intracellular drug concentration is at a constant level between the boundary of the spheroid and around 60 μm from the center, then decreases rapidly as getting closer to the spheroid center.

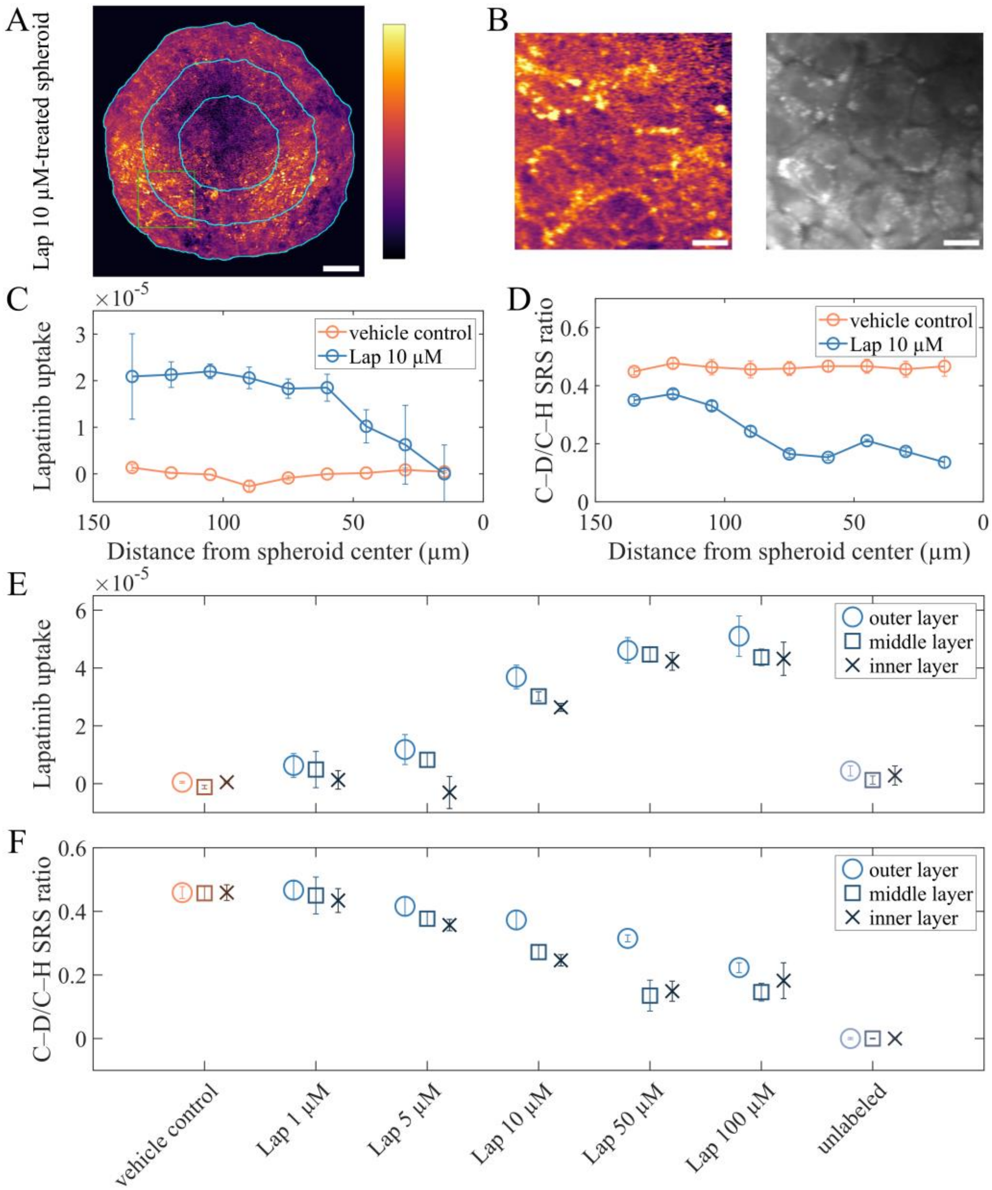

Figure 4.3. Cellular drug uptake and response in 3D-cultured spheroids treated with lapatinib. (A) The drug/C–H ratiometric image of a representative spheroid treated with 10 µM of lapatinib. (B) zoom-in ratiometric image and the corresponding C–H SRS image of a drug-enriched area (region indicated by green square in A). Spheroids were separated into layers to investigate drug penetration and cell response heterogeneity. (C-D) Plots of intracellular lapatinib uptake (C) and growth rate (D) of cells at different distances from the center of control and Lap-treated spheroids. (E-F) Plots of intracellular drug uptake (E) and growth rate (F) of cells in the inner, middle, and outer layers of spheroids treated with different concentrations of lapatinib (3 layers indicated by cyan circles in A). Scale bars: (A) 40 µm; (B) 10 µm.

Figure 4.3D illustrates the growth rates of cells at different layers in the spheroids. Cells in the vehicle control spheroids exhibited similar growth rates across all layers. It is important to note that the spheroids studied in this work have diameters of less than 300 μm and, therefore, do not have a significant oxygen concentration and nutrient penetration gradient. Spheroids exceeding 400–500 μm in diameter begin to develop a necrotic core[242], where we would expect a reduced cell growth rate at the center. Cells in all layers of the spheroids treated with 10 μM of lapatinib exhibited decreased growth rates. Interestingly, despite having a significantly lower intracellular drug uptake, cells closer to the spheroid's center exhibited a greater reduction in growth rates. This finding is counterintuitive, and we hypothesize that inner layer cells are potentially more sensitive to drugs than outer cells. It is possible that inner layer cells, having more limited access to nutrients and oxygen, are more likely to enter a quiescent state under treatment, in which cells are not proliferating or responsive to the drugs.[243–245] It has been studied that quiescent cells can lead to the emergence of therapy resistance and tumor recurrence[246,247], thus suggesting that the drug-induced quiescence of these cells could paradoxically enhance their survival capabilities and eventually contribute to increased resistance. However, further investigations are needed to elucidate the actual reasons behind the observed phenomenon.

We observed similar trends in spheroids treated with different drug concentrations. The imaged spheroids were divided into three layers, inner, middle, and outer, as illustrated in Figure 4.3A with cyan circles. Figure 4.3E displays lapatinib uptake in cells across three spheroid layers under varying dosages. With a lapatinib dosage of 1–50 μM, we can see a penetration gradient where the intracellular drug uptake level is the highest at the outer layer and lowest in the inner layer. When the drug dosage is below 5 μM, cells in the inner layer have no observable drug uptake. As dosage increases, the intracellular drug uptake level in all layers increases, with a higher drug uptake in outer layer cells than inner layer. The drug uptake becomes similar across different layers when the intracellular lapatinib concentration reaches a saturation level. These results indicate that the drug diffusion and penetration gradient across spheroids are concentration-dependent. Figure 4.3F shows the corresponding cellular responses. Overall, as lapatinib concentration increases, the growth rates of cells in all layers decrease. Similar to the trend we discussed above, cells in the inner layers exhibit higher growth inhibition. Such an effect was more obvious at higher drug concentrations. By combining drug uptake and growth rate measurements from the same spheroids, we gained valuable insights into how drugs of different concentrations penetrate through 3D-cultured cells and consequently lead to heterogeneous cellular response gradients.

Next, we explored the effects of the extracellular matrix (ECM) on drug uptake and response of 3D spheroids. The spheroids studied in the previous sections were cultured with low-attachment plates, which is a scaffold-free approach. Although scaffold-free 3D culture methods have many advantages, including high throughput and better reproducibility, they fail to provide cell-matrix interactions in tissue. Here, we used Matrigel, a protein-based hydrogel that is a well-established biomedical material for growing spheroids.[248,249] Figure 4.4A shows the C–H SRS images depicting a selection of representative spheroids cultured in Matrigel, showcasing significant variations in their size, shape, and structure. Most of the spheroids we selected for this study range from 200 to 400 μm in diameter. Compared to the round and densely packed spheroids observed in the scaffold-free method, as shown in Figure 4.1 and Figure 4.3, scaffold-based spheroids exhibit a more irregular shape and morphology. Notably, scaffold-based spheroids often display distinct cell-free regions within their structures, a characteristic not observed in scaffold-free spheroids. We postulate that these differences are likely caused by the distinct spheroid formation processes between the two approaches. In scaffold-free methods, spheroids are formed solely through cell aggregation without the presence of surrounding supporting materials. Cells aggregate and adhere to each other, facilitated by cell-cell adhesion molecules, resulting in a tightly packed spherical structure.[250–252] Subsequent cell growth and division lead to the enlargement of these spheroids. Conversely, in scaffold-based methods such as Matrigel culture, cells initially adhere to the surrounding extracellular matrix, forming an outer layer of the spheroid. Over time, these cells proliferate and gradually fill the inner regions of the spheroids, resulting in holes of various sizes and shapes between cells.

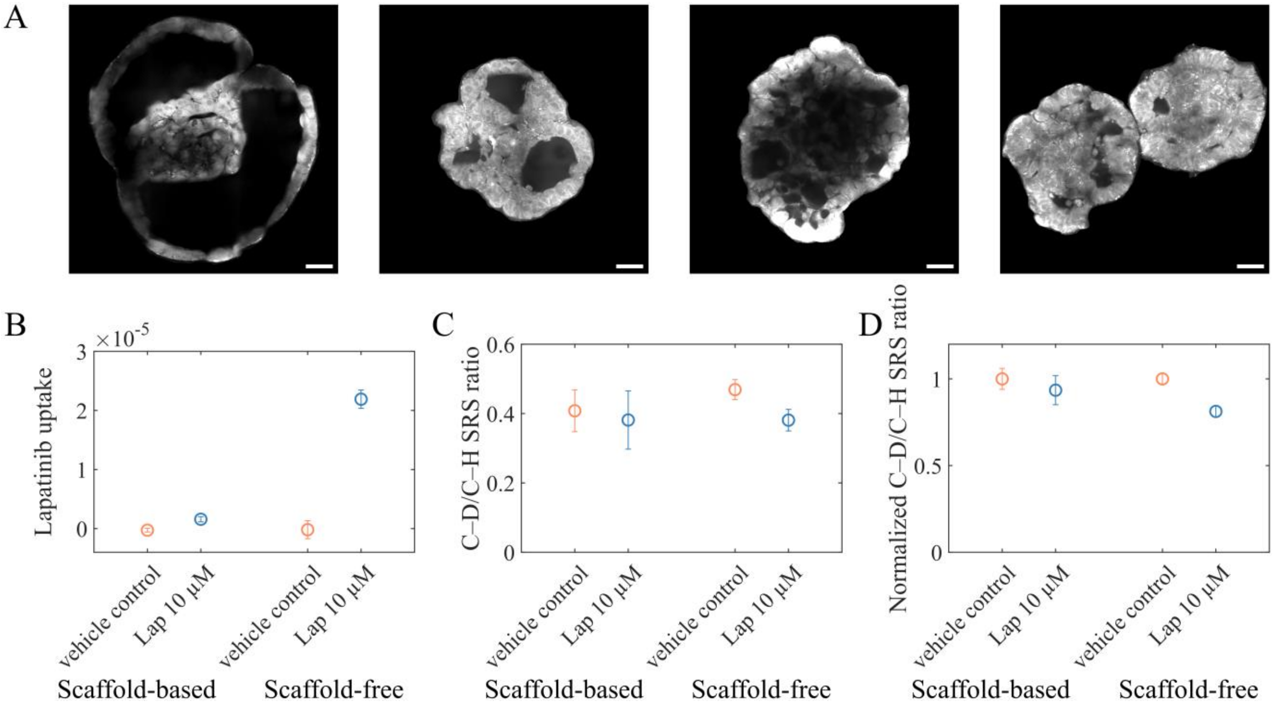

Figure 4.4. Effects of extracellular matrix on lapatinib uptake and response of 3D cells. (A) Example C–H SRS images of 3D spheroids cultured in Matrigel. (B-D) Intracellular drug uptake (B), growth rate (C), and normalized growth rate (D) comparison between scaffold-based and scaffold-free 3D spheroids treated with lapatinib at 10 µM and d-LIV-labeled for 24 hours. Scale bars: 40 µM.

To study the impact of the ECM on drug delivery and penetration, we treated Matrigel-cultured spheroids with 10 µM of lapatinib for 24 hours. We then compared the lapatinib uptake in these spheroids to that in scaffold-free spheroids under the identical treatment. The single-spheroid drug uptake measurements were normalized by the 1450 cm^{-1} cell peaks. Figure 4.4B demonstrates that the drug uptake level in scaffold-based spheroids is significantly lower than in scaffold-free spheroids. Contrary to scaffold-free culture, where spheroids are directly exposed to drug solutions, the presence of the ECM in scaffold-based culture creates a physical barrier for drug diffusion. The observed disparity in drug uptake levels between the two culture methods highlights the significant role of the ECM in impeding drug penetration in the 3D tumor environment.

Following our investigation into drug delivery and uptake, we compared spheroid growth rates between the two culture methods, as shown in Figure 4.4C. The control Matrigel-cultured spheroids exhibited slightly lower C–D/C–H SRS ratios, indicating a variance in growth rates. This reduction in growth rate can be attributed to the presence of ECM, which sterically hinders cell motion and migration and causes a less efficient nutrient delivery.[201] Additionally, both control and drug-treated scaffolded spheroids displayed a larger variation in their growth rates compared to scaffold-free spheroids, likely arising from their diverse sizes, shapes, and structures. Furthermore, by normalizing the growth rates of drug-treated spheroids to those of their respective controls, we observed a smaller decrease in growth rates for scaffolded spheroids, depicted in Figure 4.4D. This is likely due to their significantly lower drug exposure, underscoring how the extracellular matrix influences not only drug penetration but also the resultant cellular responses to treatment. Notably, contrasting the significant reduction in drug uptake due to the extracellular matrix, the inhibition of spheroid growth was less pronounced. This suggests that while spheroid growth inhibition is related to drug concentration, the relationship is not linear. Given the much higher drug tolerance of 3D spheroids, modest growth rate inhibition changes at 10 μM of lapatinib treatment are expected despite large drug uptake changes. Overall, our findings highlight the profound impact of spheroid culture conditions on drug delivery and cellular responses, demonstrating that the physical and biochemical environment significantly modifies the effectiveness of therapeutic interventions.

Lastly, we investigated differences in 2D and 3D cell growth rate response to a chemotherapeutic drug, paclitaxel (Pac), molecular formula and structure shown in Appendix A Figure A.1B. We first calculated the drug concentration at which the 2D cell growth rate is reduced by half (GR_{50}) using fixed A549 cells. The cells were treated with paclitaxel at varying concentrations, ranging from 0.2 to 5000 nM, for 24 hours. As shown in Figure 4.5A, by applying a sigmoidal fitting on the growth rate inhibition as a function of paclitaxel concentration, the GR_{50} concentration of 2D cells was determined to be 47.5 nM. Based on this measurement, we dosed cells and spheroids with 10, 50, and 100 nM of paclitaxel and performed live-cell SRS imaging after 24 hours of treatment. Representative C–H SRS images of drug-treated 2D and 3D cells are shown in Figure 4.5B. In the 2D cellular environment, at a concentration of 10 nM, many cells showed morphological features corresponding to mitotic arrest and became multinucleate. When the dosage is as high as 100 nM, most 2D A549 cells lose their nuclei and other cellular contents, indicating mitotic cell death. These observations align with the reported treatment outcomes of paclitaxel as a microtubule-stabilising drug.[253] Spheroids exhibited much less change under the same treatments. At a dosage of 10 nM, only very few cells around the spheroid periphery rounded, while the majority of cells maintained a healthy morphology. At a paclitaxel dosage of 100 nM, cells around the spheroid periphery rounded up, and their nuclei disappeared, showing signs of mitotic arrest. However, most cells in the spheroid remained less affected.

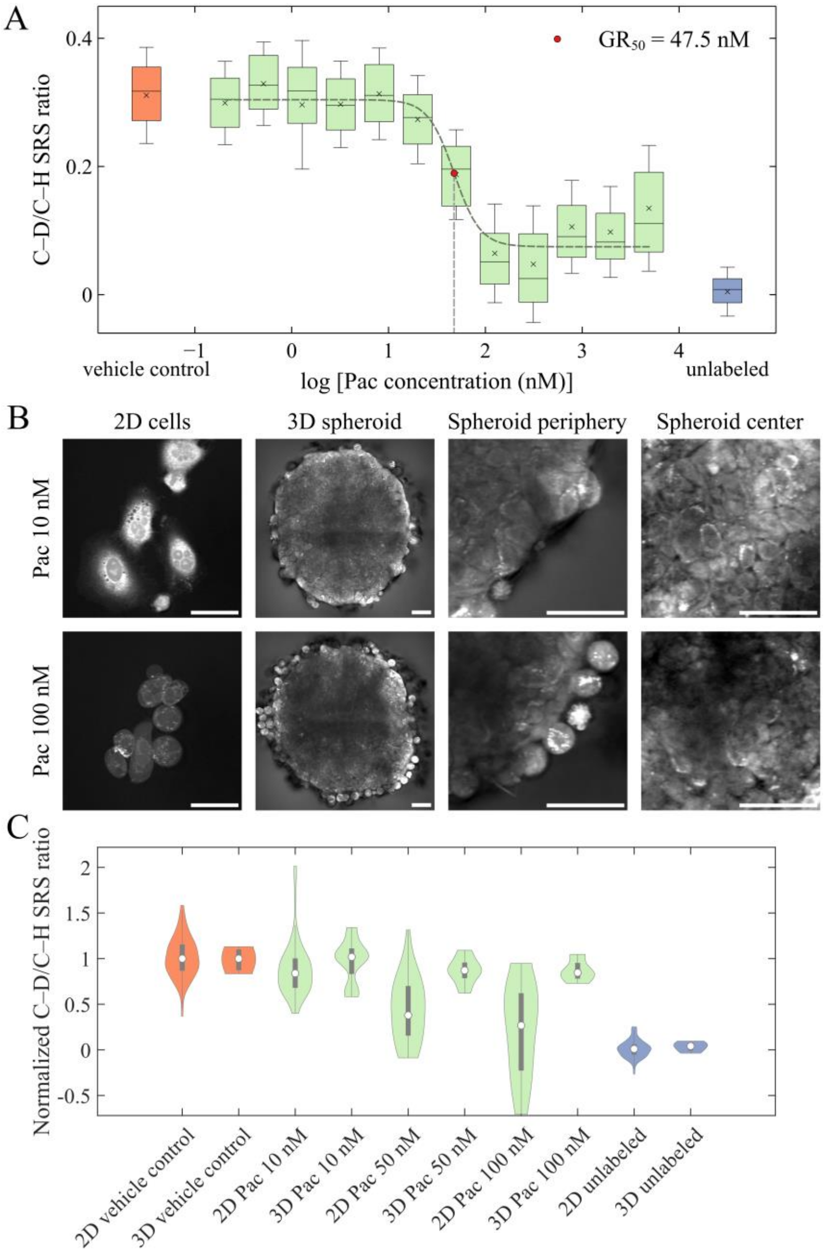

Figure 4.5. Cellular growth rate inhibition of 2D and 3D A549 cells treated with paclitaxel (Pac). (A) Growth rate response of fixed 2D cells treated with varying concentrations of Pac for 24 hours. (B) Representative C–H SRS images of Pac-treated cells and spheroids. (C) Growth rate inhibition comparison between 2D and 3D cells. Scale bars: 40 µm.

The growth inhibition comparison between 2D and 3D cells shown in Figure 4.5C matches these observations. In both 2D and 3D environments, the cell growth rate decreases as paclitaxel concentration increases. Yet, the decreasing rate, i.e., the growth rate inhibition, is significantly less in 3D, showing the same trend as the lapatinib treatment (Figure 4.2C). Given that the dosed paclitaxel concentrations are below the limit of detection of our SRS method, the drug penetration is not measurable. It is possible that paclitaxel has low penetration through the spheroids, leading to minor growth inhibition.

4.4 CONCLUSIONS

Different cell culture architectures and microenvironments lead to distinct cellular responses during drug treatment. Cells cultured in 3D environments generally exhibit higher drug resistance compared to cells in 2D monolayer, but the effect could be highly dependent on drug property and mechanism of action. Understanding such differences is important not only for designing more effective drug screening approaches during drug development but also for optimizing dosage and improving drug treatment in patients. By exploring the spatial features and growth differences between 2D and 3D cells during drug exposure, we can illuminate potential reasons for increased resistance. Our drug imaging efforts complement existing genetic and proteomic techniques that can identify a broad spectrum of genes, proteins, and biochemical pathways contributing to these cellular response differences.

Applying a robust three-band SRS imaging method capable of visualizing and quantifying both intracellular drug uptake and cellular growth response in 2D and 3D models, we performed a quantitative comparative analysis of drug uptake and its growth inhibition across different cell culture systems. For 3D cell imaging, most spheroids studied in this work, especially those cultured with the low attachment method, have a similar size of 240-270 μm diameter. Imaging at different depths would potentially fail to capture the innermost cells. To avoid such bias, the imaging depth was determined as the middle cross-section of the spheroids, which was ~120 μm. Since it was the middle cross-section, it captures an entire range of uptake and response of cells in the spheroids. The z-sectioning resolution is around 1 µm, less than the lateral resolution. However, it is the same for 2D and 3D samples if we neglect small contributions from aberration. In addition, the ratiometric analyses (C–D/C–H and drug/cell peak) can largely correct the signal loss induced by imaging depth differences and aberration. Our findings reveal that despite the similar intracellular drug levels in both 2D and 3D A549 cells during treatment with lapatinib, the 3D spheroids exhibit a notably lower impact on their growth, indicating an increased tolerance that likely stems from the complex 3D microenvironment. We note that when comparing 2D and 3D cell growth rates, we multiplied the C–D/C–H SRS ratio of 2D cells by a factor of 4, which was determined by the d-LIV labeling duration difference between 2D and 3D cells. We have previously discovered that the C–D/C–H ratio of 2D cells has a linear dependence on d-LIV labeling time during the first 8 hours; in this period, deuterated LIV replace their nondeuterated counterparts as cells grow and synthesize new proteins. After the cells grew in the d-LIV-supplemented medium for a while, deuterated LIV would replace both deuterated and nondeuterated amino acids, causing the C–D/C–H SRS ratio increase rate to eventually slow down. Therefore, we multiplied the C–D/C–H SRS ratio of 2D cells labeled for 6 hours by a factor of 4 to estimate 2D cell growth of 24 hours. On the other hand, 3D spheroids have significantly lower growth rates and, therefore, were labeled with d-LIV for 24 hours for sufficient C–D signal. While it is possible that the C–D/C–H ratio slightly underestimates 3D cell growth, the normalized C–D/C–H ratio is independent of labeling duration and provides a more robust comparison of growth response differences between the two cellular environments.

Our investigations further showed that limited drug penetration contributed to drug gradients in 3D cell cultures. Interestingly, we discovered that even though the inner layer cells in spheroids have less drug exposure and uptake, their growth rates experienced stronger inhibition, likely due to limited nutrient and oxygen availability. We also demonstrated that the presence of ECM can alter the spheroid structure, morphology, and growth and serve as a physical barrier that significantly impedes drug diffusion and uptake. The reduction in drug exposure can then lead to less prominent growth inhibition. These observations highlight how drug efficacy can be significantly modulated by the physical and biochemical environment surrounding the cells. Furthermore, our study extended beyond lapatinib to a chemotherapeutic drug, paclitaxel. Both morphological and quantitative information confirmed that cells in 3D exhibited significantly lower growth inhibition than in 2D under the same treatment. The agreement in spheroids having reduced growth inhibition than monolayer cells between different mechanisms of action drug treatments validated a generally enhanced drug tolerance in the 3D microenvironment. It is important to note that although the drugs studied in this work exhibited a similar trend in 2D and 3D cell growth response, drugs with different mechanisms of action could have varied effects. Our SRS methodology provides an essential platform for further investigation of various drugs and their unique properties and interactions in different cellular environments. Moreover, while we focused on the A549 cell, a well-established cancer cell model, for this manuscript, our SRS method applies to other cell lines and culture methods. We anticipate that the general trend of 3D cells having higher drug tolerance than their 2D counterparts will extend to other cells, as this phenomenon has been reported in previous studies.[196] Future studies can explore the drug uptake and response differences of drug-resistant cells or cells with gene mutations. These studies can broaden our understanding of cell-drug interactions and the development of drug resistance, helping to validate and expand the applicability of our conclusions across a wider range of cellular contexts.

Our three-band SRS imaging method not only advances our understanding of how biochemical and physical interactions affect drug resistance in 2D and 3D cellular systems but also sets the stage for more sophisticated drug testing with complex 3D culture models such as patient-derived organoids. The compatibility of SRS microscopy with tissue imaging enables the investigation of drug uptake and cell proliferation in patient-derived organoids and tissues. With the incorporation of epi-mode detection, this technique may also allow for in vivo monitoring and measuring drug penetration and cellular response in actual tumors in mice. Additionally, it is important to note that cell growth inhibition does not necessarily correlate with cell death. To enhance the robustness of our findings, our method can be integrated with viability measurements, such as live/dead staining and fluorescence imaging, to provide a more comprehensive profile of cellular responses during treatment in varying microenvironments. Moreover, coupling our results with RNA sequencing could identify specific genetic differences between cells under different culture conditions and drug treatments, thereby refining our understanding of the intricate drug resistance mechanisms. Overall, we anticipate that the continued refinement and application of these methods will yield critical insights necessary for understanding and overcoming drug resistance and improving treatment outcomes in clinical settings.

CHAPTER 5. DISCRIMINATION OF LIPID COMPOSITION AND CELLULAR LOCALIZATION IN HUMAN LIVER TISSUES BY STIMULATED RAMAN SCATTERING MICROSCOPY

The work presented in this chapter has been published in the following article[254]*:*

Xu, F. X.; Ioannou, G. N.; Lee, S. P.; Savard, C.; Horn, C. L.; Fu, D. Discrimination of Lipid Composition and Cellular Localization in Human Liver Tissues by Stimulated Raman Scattering Microscopy. *J Biomed Opt* **2024**, *29* (1), 016008. https://doi.org/10.1117/1.JBO.29.1.016008.

5.1 INTRODUCTION

In this chapter, we shift the focus from protein synthesis in cells to using SRS microscopy to study lipid metabolism in liver tissue samples. The molecular mechanisms driving the development of advanced fibrosing nonalcoholic steatohepatitis (NASH) and cirrhosis in a relatively small subset of persons with nonalcoholic fatty liver disease (NAFLD) are incompletely understood. Lipotoxicity is a prominent pathogenetic mechanism postulated to explain the progression of fatty liver disease from “simple steatosis” (or nonalcoholic fatty liver, NAFL) to NASH, accompanied by the development of hepatic necroinflammation and fibrosis. Lipotoxicity theories of NASH suggest that certain lipid molecules (e.g., cholesterol, ceramides, di-acylglycerol, or free fatty acids) are responsible for initiating and/or driving the inflammation and fibrosis that characterizes NASH, whereas other lipid molecules (e.g., triglycerides) may be innocent bystanders that are present in NASH, even in relatively large quantities, but do not necessarily drive disease progression. The cellular (e.g., hepatocytes versus Kupffer cells versus stellate cells) and subcellular (e.g., within lipid droplets versus endoplasmic reticulum) localization of potentially harmful lipid species is also critical to understanding how lipotoxicity may contribute to NASH pathogenesis. We, and others, have been particularly interested in the potential role of cholesterol and cholesteryl esters as critical lipotoxic molecules in NAFLD progression, including the implications of both its cellular and subcellular localization.[255–259]

Raman microscopy is a technique that has been applied to NAFLD only recently and has great potential in further clarifying the role of lipotoxicity in NASH because it can characterize both the type and spatial localization of relevant lipid molecules.[260–264] Specifically, Minamikawa et al. applied Raman microscopy to visualize the distribution of lipid droplets in hepatocytes in NASH model mice liver tissues and demonstrated its capability of characterizing the molecular features of accumulated microvesicular and macrovesicular lipid droplets.[260] Takemura et al. utilized spontaneous Raman to evaluate steatosis and retinol content in rat liver tissues at the nascent state of NAFLD.[261] Diagnosing states of NAFLD in mice models can also be achieved by Raman micro-spectroscopy combined with machine learning algorithms.[262–264] Our group has been involved in the development of hyperspectral stimulated Raman scattering (hsSRS) microscopy as an advancement over traditional Raman microscopy, which offers several advantages such as increased imaging sensitivity and acquisition speed.[69–71,265] Moreover, the SRS signal has a linear dependence on the analyte concentration, making it an ideal tool for quantitative chemical composition analysis.[266] Previous research has demonstrated the utility of SRS microscopy in investigating subcellular distributions and metabolic dynamics of lipid molecules in cells and tissues.[76,84,82,267–271] By leveraging the spectral differences between lipid species, SRS microscopy has shown its potential in classifying different types of lipid molecules. Specifically, our lab has applied hyperspectral SRS imaging, i.e., acquiring SRS images at a series of vibrational frequencies, in the carbon–hydrogen (C–H) stretching region, between 2825 and 3050 cm^{-1}, to quantitatively differentiate and localize cholesteryl esters and triglycerides in cells and mouse liver and adrenal gland tissues.[82] Wang et al. demonstrated that fingerprint region (within 400 – 1800 cm^{-1}) SRS imaging enables the classification of crystalline cholesterol, cholesteryl esters, and triglycerides in atherosclerotic arterial tissues. [84] Moreover, SRS microscopy can also distinguish saturated lipid molecules (i.e., fatty acid (FA) chains have all single carbon–carbon bonds) from unsaturated lipids (fatty acid chains contain carbon–carbon double bonds) and determine the saturation level of specific lipid species. For instance, Jia et al. employed SRS imaging for quantifying triglycerides of different saturation degrees based on the ratio between the =C–H band at 3010 cm^{-1} and the CH_2 band at 2850 cm^{-1} in fibrotic liver tissues.[271]

In this work, we applied the dual-band SRS imaging system presented in Chapter 2 that simultaneously acquires hyperspectral data from both C–H stretching and fingerprint region to accurately classify free cholesterol, saturated cholesterol ester, unsaturated cholesterol ester, and triglyceride. We also report our image analysis pipeline that enables characterizing the content and cellular localization of these lipid species in liver tissue sections from NAFL and NASH patients and compare them with traditional polarization microscopy used for identifying cholesterol crystals. We anticipate that the SRS imaging and analysis pipeline we developed here can be used in future studies to provide insights into how these lipid molecules might exert lipotoxic effects and contribute to the progression from NAFL to NASH.

5.2 MATERIALS AND METHODS

5.2.1 *Patients with biopsy-proven NAFL and NASH*

Patient data, serum specimens, and liver tissue were derived from a biorepository at Veterans Affairs Puget Sound Healthcare System (VAPSHCS). This biorepository prospectively recruited patients undergoing clinically indicated liver biopsies and stored liver tissue that was flash-frozen in liquid nitrogen immediately after the liver biopsy. We identified patients with NAFLD based on histological hepatic steatosis on liver biopsy in the absence of hepatitis C virus (negative serum HCV antibody and HCV RNA), hepatitis B virus (negative serum HBV surface antigen), excessive alcohol consumption (dedicated alcohol questionnaire administered on the day of the liver biopsy), iron overload (hepatic stain and serum iron markers), or markers of autoimmune liver diseases. Liver slides were prospectively reviewed by a hepatopathologist who scored the grade of steatosis (1-3), inflammation (0-3), ballooning degeneration (0-2), and the stage of fibrosis (0-4) according to the system proposed by Kleiner et al.[272] We randomly selected frozen liver tissue specimens from patients with NAFLD who either had histological "isolated steatosis (NAFL)" or "fibrosing-NASH" defined as follows:

A. "Isolated Steatosis", also known as "nonalcoholic fatty liver" or NAFL [273] (n=5): Defined by histological steatosis grades 1-3, inflammation grade 0-1, fibrosis stage 0, and ballooning degeneration grade 0.

B. "Fibrosing-NASH" (n=7): Defined by histological steatosis grades 1-3, inflammation grade 1-3, fibrosis stage 1-3, and ballooning degeneration grade 1-2. We purposefully selected patients with NASH who had fibrosis because fibrosis is the histological feature most strongly associated with adverse long-term outcomes in patients with NAFLD.[274,275]

5.2.2 *NAFLD tissue sectioning and slide preparation*

A 2-3 mm piece of repository stored frozen human liver biopsies were snap frozen in OCT Compound. 10 μm sections of the livers were cut on a cryostat, placed on glass slides, and stored at -70 degrees. For polarization and SRS analysis, the slides were thawed at room temperature for 10 minutes and then coverslipped with Aquamount (ThermoFisher, Kalamazoo, MI) using No.1.5

cover glass. Sections were immediately viewed using a polarizing microscope followed by the SRS imaging system.

5.2.3 *Dual-band hsSRS microscopy system*

The schematic diagram of the SRS imaging setup used for this project is shown in Figure 5.1. The Stokes beam was generated by an ultrafast oscillator (Light Conversion FLINT-FL2) at a center wavelength of 1030 nm. The pump beams were generated using two home-built optical parametric oscillators (OPOs) at center wavelengths of 790 and 880 nm that probe the C–H and fingerprint regions, respectively. The synchronized femtosecond laser pulses were chirped to approximately 2 ps using SF11 glass rods. The temporal delay between the pump and Stokes pulses was controlled by a motorized delay stage (Zaber X-DMQ-AE). The combined beams were sent into a home-built microscope equipped with a 40x water immersion objective (Nikon N40XLWD-NIR, NA = 1.15). A polarizing beam splitter was used to control the polarization state of the incident beams at the sample plane. The polarizing beam splitter was configured to transmit linearly polarized light along the y-direction. At the sample, the power of both pump and Stokes beams was 40 mW. The two pump beams were separated by a dichroic after the sample and detected separately using an amplified Si photodiode, and the SRS signals were extracted by a dual-channel lock-in amplifier (Liquid instruments Moku:Pro). All images collected were 512 × 512 pixels with a spatial resolution of approximately 400 nm.

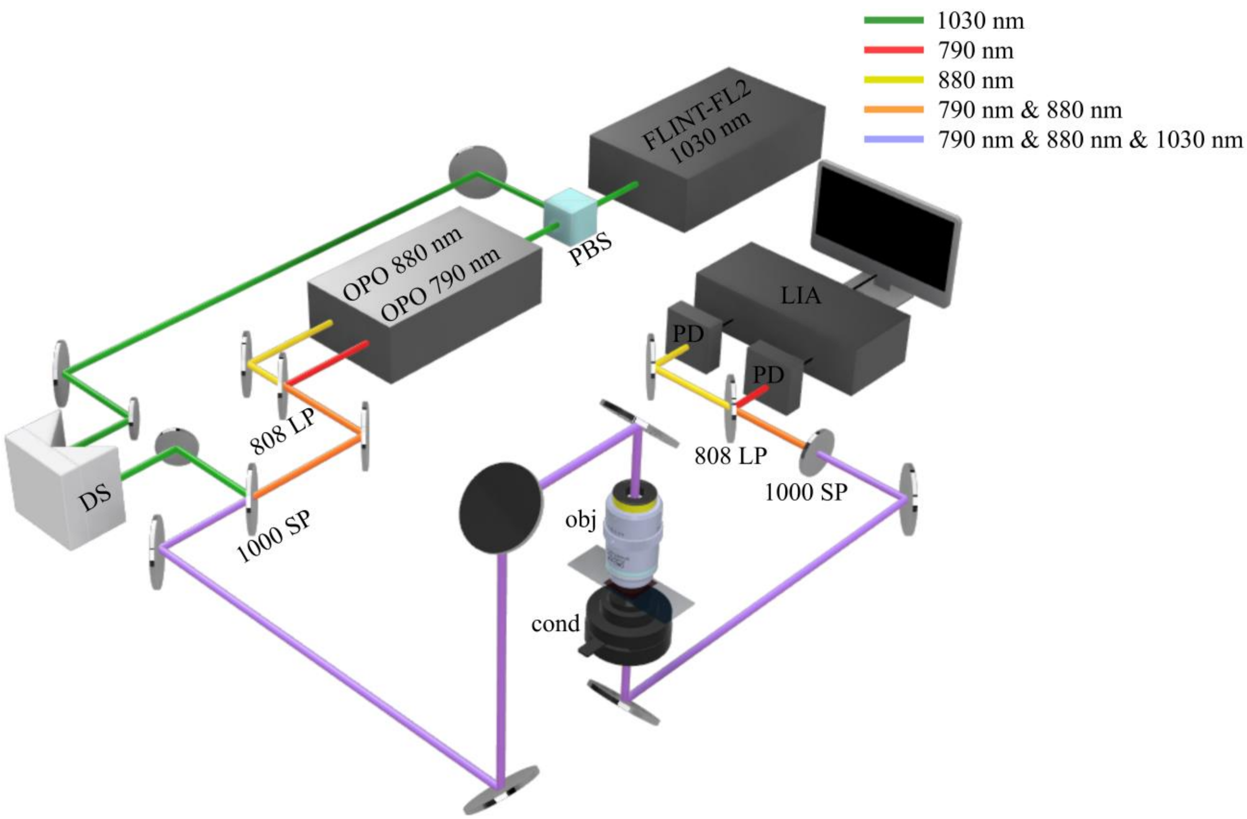

Figure 5.1. Schematic diagram of the dual-band hyperspectral SRS microscopy system for liver tissue imaging. The Stokes beam is generated directly by an ultrafast laser, FLINT-FL2, at a center wavelength of 1030 nm. The second harmonic of 1030 nm pulse is used to pump two optical parametric oscillators (OPOs) to generate two synchronized pump beams at 790 nm and 880 nm. The two pump beams are combined by an 808 nm long pass (808 LP) dichroic mirror. The three beams are then combined with a 1000 nm short pass (1000 SP) dichroic mirror and synchronized using a delay stage (DS). The overlapped pulses are sent into a homebuilt upright microscope system (obj: objective; cond: condenser). The SRS signals are detected by two photodiodes (PDs) and demodulated with a multi-channel lock-in amplifier (LIA).

5.2.4 *Spectral unmixing and lipid classification*

To determine the cellular distribution of free cholesterol, cholesteryl ester (CE), and triglyceride (TAG), we collected the calibration standard SRS spectra of free cholesterol (Sigma-Aldrich), saturated CE (cholesteryl palmitate (13.1% CE, Sigma-Aldrich) and cholesteryl stearate (1.94% CE, Sigma-Aldrich)), unsaturated CE (cholesteryl linoleate (47.1% CE, Sigma-Aldrich) and cholesteryl oleate (20.3% CE, Sigma-Aldrich)), and TAG (1,3-dioleoyl-2-palmitoyl glycerol (11.7% TAG, Cayman Chemical), glyceryl trioleate (3.25% TAG, Sigma-Aldrich), 1-myristoyl-2-oleoyl-3-palmitoyl-rac-glycerol (0.911% TAG, Cayman Chemical), 1,2,3-tri-heptadecenoyl glycerol (~0.1% TAG, Cayman Chemical)). We selected these CE and TAG calibration samples based on their high abundance in three human NAFLD tissue samples (2 diagnosed as NAFL and 1 as NASH) measured with MS-spectroscopy in our laboratory.

We examined previously frozen liver tissue samples from 12 NAFLD patients, including 5 classified as NAFL and 7 as fibrosing-NASH. For each liver tissue slice, we acquired hyperspectral stacks of SRS images in both the C–H stretching region in the high wavenumber window, between 2800 and 3060 cm^{-1}, and the C=C/C=O stretching region in the fingerprint window, between 1645 and 1780 cm^{-1}. The lipid droplets were segmented from the surrounding non-lipid components, such as collagen, by thresholding the 2850/2930 cm^{-1} ratiometric image. A nonnegative linear least-squares spectral unmixing algorithm (MATLAB Isqnonneg) was applied to both the C–H and the fingerprint region spectra for spectral unmixing of each pixel in lipid droplets. The spectral unmixing results from the two spectral bands were combined to generate lipid composition maps.

5.2.5 *Brightfield and polarized light microscopy system*

Liver tissue section slides were viewed by the Nikon Ni-E microscope using brightfield and polarization filters prior to hyperspectral SRS imaging. Images were taken using a Nikon color camera.

5.2.6 *Assessment of hepatic free cholesterol*

Free cholesterol was extracted with water, methanol, and chloroform solvents (1:1:1 v/v/v). The chloroform fractions were dried using nitrogen gas, and the residues were dissolved in deuterated chloroform. NMR spectra were obtained using an 800 MHz Bruker Avance III spectrometer. Free cholesterol signal was identified, and its concentration was obtained using the residual solvent signal from the solvent as the internal reference.

5.2.7 *Assessment of other hepatic lipids*

Lipids were extracted using dichloromethane/methanol after the addition of 54 isotope-labeled internal standards. The extracts were concentrated under nitrogen and reconstituted in 10 mM ammonium acetate in dichloromethane:methanol (50:50). Lipids were analyzed using the Sciex Lipidyzer platform consisting of a Shimadzu LC and AB Sciex QTRAP 5500 MS/MS system equipped with SelexION for differential mobility spectrometry (DMS). Multiple reaction monitoring (MRM) was used to target and quantify lipids in positive and negative ionization modes with and without DMS.

5.3 RESULTS

5.3.1 *Quantitative classification of lipid molecules*

We obtained SRS spectra of several lipid standard samples as calibration standards to facilitate the identification of different lipid molecules. The normalized C–H region and fingerprint region SRS spectra of free cholesterol, CE, and TAG are demonstrated in Figure 5.2A and B, respectively. The SRS spectra of all imaged lipid standard samples are presented in Appendix B Figure B.1. We observed clear spectral differences between free cholesterol, CE, and TAG. The relative peak heights in the 2850 – 2950 cm^{-1} region and around 3010 cm^{-1} are distinctive between different molecules. The spectral separations in the fingerprint are also distinct. Free cholesterol has a single sharp peak, resulting from C=C stretching, at 1673 cm^{-1} and no peak near 1740 cm^{-1}; whereas both CE and TAG molecules contain C=O bonds that contribute to an additional peak at around 1740 cm^{-1}. Compared to CE, the C=C Raman peak of TAG shifts lower while the C=O shifts slightly higher. More interestingly, we observed a significant spectral difference between saturated CE and unsaturated CE. As indicated with shaded lines in Figure 5.2, in the C–H region, saturated CE has a strong peak at around 2880 cm^{-1}, a small peak at 2850 cm^{-1}, and no peak at 3010 cm^{-1}, whereas unsaturated CE has four peaks at 2865 cm^{-1}, 2900 cm^{-1}, 2930 cm^{-1}, and 3010 cm^{-1}. Additionally, the saturated CE has a strong Raman peak at 1667 cm^{-1} in the fingerprint region (green shaded line), and unsaturated CE has a peak near 1656 cm^{-1} (blue shaded line). These differences allow spectral separation and identification of the saturated and unsaturated CE.

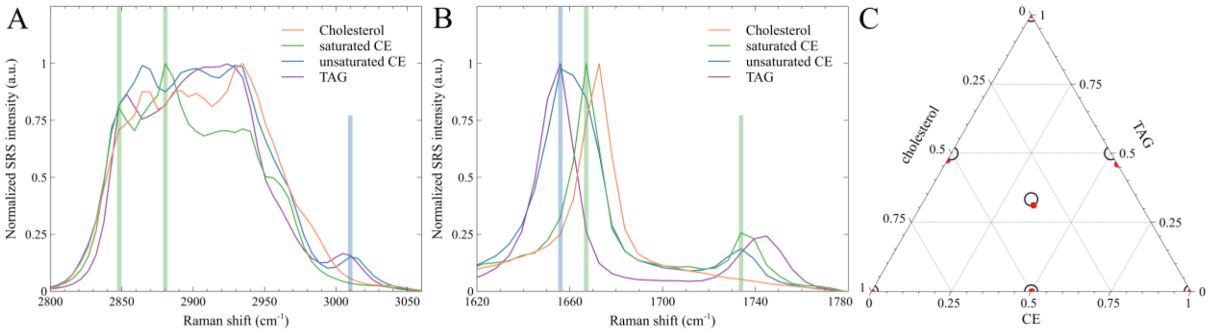

Figure 5.2. SRS spectra of cholesterol crystal, saturated cholesteryl ester, unsaturated cholesteryl ester, and triglyceride in the C–H region (A) and fingerprint region (B). Shaded lines: main spectral differences between saturated CE (green) and unsaturated CE (blue). (C) Ternary plot of the calculated fractions of three-component mixtures using SRS imaging and the spectral unmixing algorithm. Black circles: lipid standard mixture fractions. Red dots: calculated lipid fractions.

We then evaluated the accuracy of the classification and quantification of different types of lipid molecules with a ternary solution system. We performed SRS imaging and the linear least-squares spectral unmixing analysis on mixtures of cholesterol, cholesteryl oleate (representing CE), and glyceryl trioleate (representing TAG) at different ratios in $CDCl_3$ solutions. The SRS spectra of cholesterol, unsaturated CE, and TAG in both the C–H stretching region (2800 – 3060 cm^{-1}) and fingerprint region (1645 – 1780 cm^{-1}) were used for the unmixing analysis. The quantitative determination of lipid concentrations in three-component mixtures is shown in Figure 5.2C, with black circles representing the lipid standard mixture percentages and red dots indicating the calculated lipid percentages. The accuracies of the calculated concentrations are above 92%, with an average of 95.3%, validating that our imaging and analysis system provides a quantitative identification and classification of different lipid molecules based on their spectral information.

5.3.2 *Lipid composition and cellular localization in human NAFLD tissues*

We examined frozen liver sections from 12 NAFLD patients (7 NASH, 5 NAFL) via hyperspectral SRS imaging in the C–H and fingerprint regions, followed by linear least-squares spectral unmixing analysis. Our image processing pipeline is shown in Figure 5.3. In the acquired SRS images, many non-lipid tissue components, predominantly proteins, contain abundant CH_3 bonds and therefore generate strong signals at the CH_3 peak at 2930 cm^{-1}. In contrast, all lipid species are CH_2 bond-rich and hence produce strong signals at the CH_2 peak around 2850 cm^{-1}.[68] Leveraging this spectral difference, we can separate lipid molecules from their surrounding components by taking the ratio between SRS images at 2850 cm^{-1} and 2930 cm^{-1}, which highlights lipid contents and suppresses signals from other species. We generated a binary lipid map for each tissue by thresholding the $R_{2850/2930}$ ratiometric image (Figure 5.3C). After isolating lipid droplets from non-lipid backgrounds, including collagen and cell cytoplasm, we apply the linear least-squares spectral unmixing algorithm on each pixel of the lipid droplets in hyperspectral SRS images of both spectral regions to obtain the molar percentages of free cholesterol, saturated CE, unsaturated CE, and total TAG. We note that 100% is defined as the total concentration of these four aforementioned lipid species. We then plotted the mole percent measurements as percentage maps for each classified lipid type, as shown in Figure 5.3F - I. To evaluate the performance of the fitting algorithm, we demonstrated three example pixel SRS spectra and their spectral unmixing algorithm fitted results in Appendix B Figure B.2A - C. The spectral unmixing results were determined as the sum of each individual lipid spectrum multiplied by its calculated percentage. The three pixels were selected from regions that were classified with higher percentages of TAG (Appendix B Figure B.2A), saturated CE (Appendix B Figure B.2B), or free cholesterol (Appendix B Figure B.2C). Overall, the spectral unmixing results overlap well with the SRS spectra. We also generated fitting error maps for spectra in both C–H and fingerprint regions individually (Appendix B Figure B.2D). We evaluated the fitting error by the squared value of the fitting residual norm. A smaller residual norm value represents a more accurate fitting result. We also explored the distributions of TAG at different unsaturation levels by including spectra of TAG containing both saturated and unsaturated FA chains and TAG containing exclusively unsaturated FAs in the spectral unmixing algorithm. We demonstrated the comparison between lipid percentage maps generated by the two versions of the spectral unmixing algorithm in Appendix B Figure B.3. Both spectral unmixing algorithm versions generated similar free cholesterol, saturated CE, and unsaturated CE percentage maps with comparable fitting error maps. The total TAG map generated in version 1 matches the sum of the two different unsaturation level TAG maps in version 2.

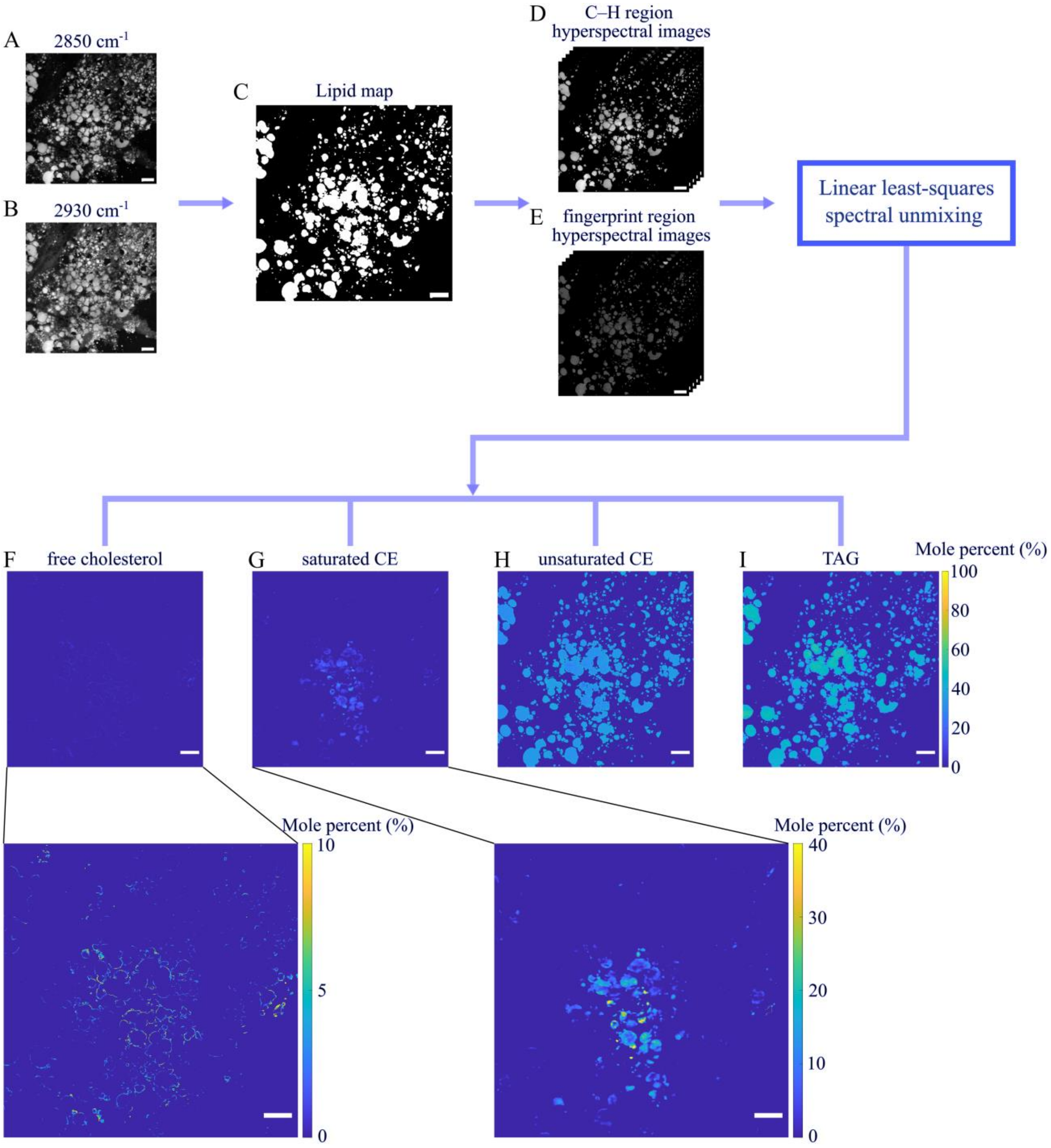

Figure 5.3. Schematic diagram of the image analysis pipeline and representative SRS images and lipid composition maps of a liver tissue section from a patient with NASH. From the SRS images at 2850 cm^{-1} (A) and 2930 cm^{-1}(B), we use the $R_{2850/2930}$ ratiometric image to create a binary lipid map (C). We then perform the linear least-squares spectral unmixing analysis on both C–H and fingerprint region hyperspectral SRS images of lipid molecules (D-E) to generate mole percentage maps of free cholesterol, saturated CE, unsaturated CE, and TAG (F-I). The percentage

maps of free cholesterol and saturated CE are also shown with a scale extending only from 0-10% (for cholesterol) and 0-40% (for saturated CE) rather than for 0-100% in order to make more apparent the distribution of these lipids that are present in much lower relative percentages than unsaturated CEs and TAGs. Scale bar: 50 µm.

We discovered that in the examined tissues, the localization of TAG and unsaturated CE are overall uniform across all lipid droplets. TAG is the dominant lipid species in the majority of lipid droplets, with an average percentage above 50-60%. We observed that distributions of TAG of different saturation levels are also uniform, with a slightly higher percentage of higher unsaturation degree TAG (Appendix B Figure B.3). Interestingly, saturated CE and free cholesterol have much lower percentages and less uniform distributions compared to TAG and unsaturated CE in all tissues. We adjusted the contrast of both percentage maps from 0 – 100% to 0 – 40% and 0 – 10%, respectively, to better visualize saturated CE and free cholesterol in the representative field-of-view shown in Figure 5.3. In Figure 5.3G, saturated CE forms a cluster below the center of the image but is not present in other lipid droplets. In Figure 5.3F, we observed that the algorithm classifies the outer periphery of most lipid droplets as free cholesterol. This pattern agrees with the localization of free cholesterol determined by filipin staining (Appendix B Figure B.4). However, it is important to note that because free cholesterol abundance is quite low, this percentage map is potentially susceptible to fitting errors. As illustrated in Appendix B Figure B.2C, the fingerprint region spectral unmixing result of a pixel selected from a region classified with higher free cholesterol shows a lower fitting accuracy with its SRS spectrum compared to the other pixels. The SRS spectrum is nosier in the 1700 – 1780 cm^{-1} region due to the lower SRS intensity from C=O vibration, which could lead to higher spectral unmixing inaccuracy. Additionally, as shown in the corresponding C–H region spectra fitting error map in Appendix B Figure B.2D, the squared residual norm value is higher around the edges of all lipid droplets. Based on lipidomics analysis data shown in Appendix B Table B.1, the average percentage of free cholesterol in a NASH tissue sample is at the level of 0.001%. If its distribution is only at the surface of droplets, as filipin staining suggested[276,277], the local concentration could be much higher and reach the detection limit of SRS. Nonetheless, quantifying free cholesterol with current SRS sensitivity may suffer from a lower accuracy compared to the other lipid species.

The submicron resolution of SRS microscopy allows us to investigate the subcellular distribution of analyzed lipid species in each lipid droplet. Three representative lipid droplets in an examined NASH tissue are shown in Figure 5.4. Most interestingly, we discovered that saturated CE tends to self-associate into a heterogeneous subcellular localization pattern. Saturated CE molecules are observed to be predominantly near the boundary of the lipid droplet. In lipid droplets such as lipid droplet 1 in Figure 5.4, saturated CE appears as arcs surrounding the central TAG and unsaturated CE core. In certain areas, as shown by lipid droplet 2, an enriched condensate of saturated CE can form crescent-like deposits. We hypothesize that these saturated CE molecules are inclined to self-aggregate to create a microenvironment where they can easily interact with the lipid droplet envelope consisting of phospholipids and free cholesterol at the periphery. It is also possible that the crescent-like localization of saturated CE allows them to bind to abundant membrane proteins. Occasionally, further enrichment of saturated CE leads to a uniform deposit pattern across the lipid droplet, as shown in Figure 5.4 lipid droplet 3. Overall, the heterogeneity in the spatial distribution of specific lipid molecules confirmed that imaging techniques with spatially resolved capability are essential for investigating the functions and interactions of various lipid species. We note that the polarization state of the incident laser beams at the sample plane may also contribute to the observed lipid distribution patterns. However, we found that the localization patterns of lipid molecules in general displayed random orientations and shapes across multiple samples, which suggests that they were not dominated by the laser polarization state.

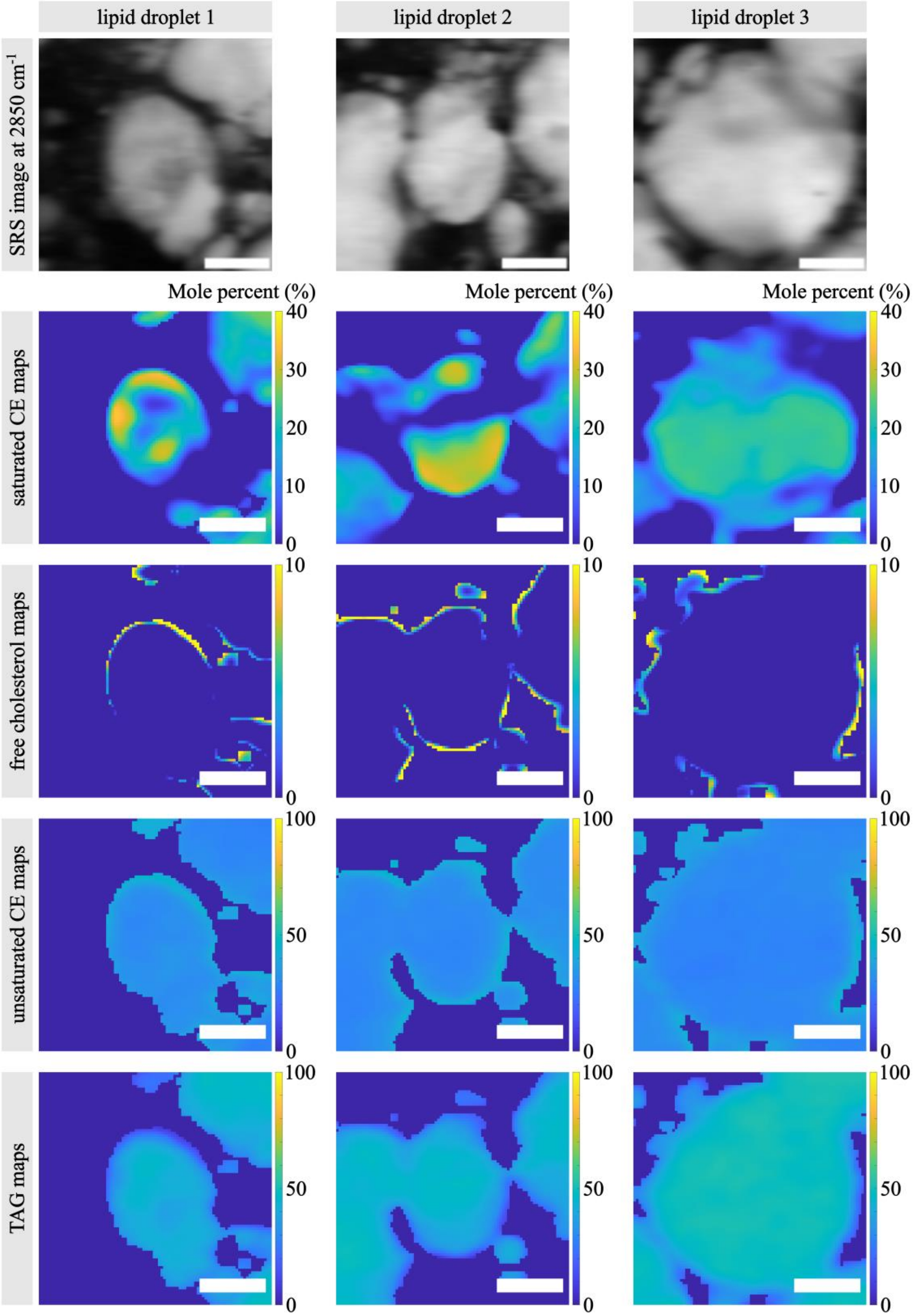

Figure 5.4. The 2850 cm^{-1} SRS images and percentage maps of three representative lipid droplets selected from the frozen liver section of a patient with NASH. The three lipid droplets demonstrate homogeneous TAG and unsaturated CE compositions but heterogeneous free cholesterol and saturated CE compositions. Scale bar: 10 µm.

5.3.3 *Identifying the origin of birefringent crystals in NAFLD tissues*

Polarized light microscopy has been used to investigate the association of cholesterol crystal formation with high cholesterol uptake in NAFLD tissues. It was hypothesized that cholesterol crystal leads to strong birefringence, which can be easily detected with polarized light microscopy. These crystals were indeed observed in both mouse tissue and human liver sections from patients with NASH.[258,278] Furthermore, the birefringence signals of these crystals were found to be strongly correlated with NASH progression.[256] However, the identity of those birefringent crystals was never conclusively determined due to a lack of spatially resolved chemical information. To investigate the chemical composition of the birefringent crystals, we performed SRS imaging and analysis on human tissue sections immediately after acquiring polarization images using polarized light microscopy. The brightfield, polarization images, and SRS imaging generated percentage maps of the same regions for two NAFLD tissues are shown in Figure 5.5. We selected a typical NAFL tissue section region with no birefringent signals (A) and a NASH tissue section region with abundant birefringent crystals (B). The NASH tissue contains a high accumulation of birefringent crystals in the center region and low birefringent signals in the surrounding lipid droplets. This pattern matches the saturated CE percentage map. The spatial difference between the polarization image and saturated CE percentage map is caused by the imaging tissue depth difference, as the polarized light microscope has a much larger depth of focus compared to SRS microscopy. Similarly, the extremely low percentage of saturated CE in the selected NAFL tissue (Figure 5.5A) agrees with its corresponding polarization image. The distributions of free cholesterol, unsaturated CE, and TAG suggested by their percentage maps have low spatial correlations with the strong birefringent signals. In both NAFL and NASH tissue images, the calculated free cholesterol accumulates around the periphery of lipid droplets, and the unsaturated CE and TAG localizations are uniform across the entire imaged regions.

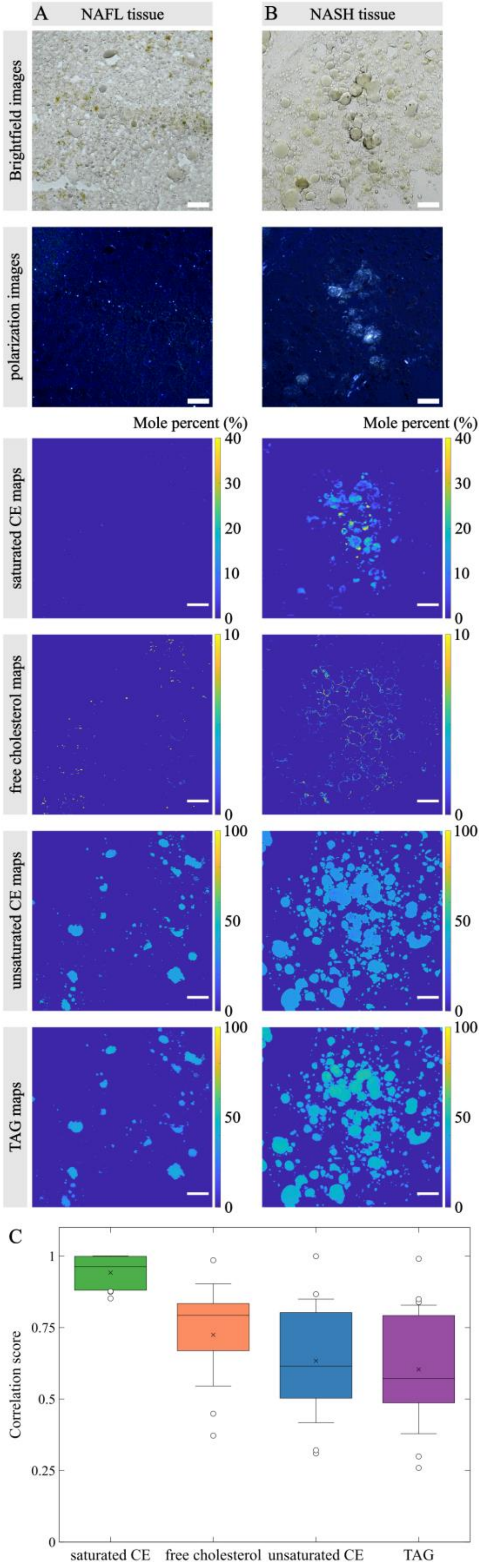
A
NAFL tissue
B
NASH tissue
Brightfield images
polarization images
Mole percent (%)
Mole percent (%)
saturated CE maps
40
30
20
10
0
free cholesterol maps
10
0
unsaturated CE maps
100
50
0
TAG maps
100
50
0
C
Correlation score
1
0.75
0.5
0.25
0
saturated CE
free cholesterol
unsaturated CE
TAG

Figure 5.5. Brightfield, polarization images, and percentage maps of a NAFL tissue section region with low birefringent signals (A) and a NASH tissue section region with abundant birefringent crystals (B). Pixel percentage correlation plots between birefringent signals in polarization images and different lipid species. Scale bar: 50 μm. (C) Evaluation of spatial correlation between the polarization images and lipid percentage maps for 7 NAFLD tissues with standard deviations as error bars.

We observed the same correlation trends in all imaged human liver tissue samples. We evaluated the spatial correlation between birefringent signals and different lipid molecules by converting the polarization images and lipid percentage maps to binary maps and comparing their pixel values. The correlation score was calculated for each tissue image as the number of matching pixels between the two binary images divided by the total number of pixels. A correlation score closer to 1 indicates a better matching between the two images. We report the correlation scores of the four lipid molecules for 7 NAFLD tissues in Figure 5.5C. The average correlation score of saturated CE is as high as 0.94, with a low standard deviation of 0.06, indicating a strong spatial correlation between birefringent signals in polarization images and saturated CE accumulation. The average correlation scores between birefringent signals and other lipid molecules, free cholesterol, unsaturated CE, and TAG, are 0.72, 0.63, and 0.60, respectively, with high standard deviations of 0.18, 0.22, and 0.22. These lower average correlation scores and larger variations indicate lower matchings between the distribution of birefringent signals and the localization of these lipid molecules. This reveals that these lipid species play less significant roles in birefringent crystal formation.

We plotted out the average percentages of different lipid species based on SRS-imaged regions of liver tissue sections from patients diagnosed with NAFL and NASH (Appendix B Figure B.5). The two groups had no statistical significance for all lipid species, partially due to the limited sample size for each patient. More importantly, we observed abundant birefringent crystals in some regions of NAFL tissues and specifically selected these regions for SRS imaging, resulting in a selection bias with much higher percentages of saturated CE. These regions with strong birefringent crystals in NAFL may indicate the development of NASH. In homogeneous sample measurements, such as lipidomics analysis, these early signs of NASH development are susceptible to being overlooked because of their low percentages compared to the rest of the tissue. With larger tissue size and unbiased sampling, our SRS method is suitable for detecting regions with abundant saturated CE to provide insights into the progression from NAFL to NASH.

5.4 DISCUSSION

Understanding the molecular mechanisms underlying the disease progression from NAFL to NASH is crucial for both the prevention and treatment of NASH. Lipotoxicity induced by different lipid molecules is thought to play a critical role in the development and progression of NASH. Lipidomics analysis is a well-established technique for quantifying lipid composition, but it does not provide spatial information and therefore hinders the investigation of lipid localization heterogeneity in the analyzed specimens. In comparison, SRS microscopy offers both spatial (cellular and subcellular) and chemical information on lipid species classification and quantification. In this work, we presented an SRS method that combines C–H and fingerprint region to characterize the distribution of different lipid species in liver tissue sections from NAFLD patients. We note that the dual-band hyperspectral SRS system is not a fundamental requirement for the study, as the same analysis pipeline can be applied to images acquired with conventional single-band SRS systems by tuning laser wavelength. However, the simultaneous acquisition of SRS images in the two separate spectral regions without wavelength tuning improves imaging speed by two-fold and minimizes imaging inaccuracy caused by sample movement, focus drift, or laser power fluctuation. By collecting spatial and spectral information from hyperspectral SRS imaging in both the high wavenumber C–H stretching region and the fingerprint C=C/C=O stretching region, we demonstrated spatially resolved mapping of free cholesterol, saturated CE, unsaturated CE, and TAG distribution in lipid droplets. We developed an image acquisition and processing pipeline that allows us to explore the cellular and subcellular localization patterns of these different lipid molecules.

We found that TAG is the most abundant lipid species and distributes uniformly across all hepatocyte lipid droplets in the human NAFLD tissues, followed by unsaturated CE. Saturated CE has a much lower mole percentage than TAG and unsaturated CE. These results agree with lipidomics analysis. Importantly, we found that only saturated CE and free cholesterol have a heterogenous distribution pattern: saturated CE molecules tend to self-aggregate around the periphery of a small percentage of lipid droplets, and further enrichment can lead to a relatively uniform localization within the lipid droplets, while the outer periphery of lipid droplets is the most probable location for free cholesterol to accumulate. The cholesterol distribution is supported by filipin staining, but quantification is susceptible to fitting errors due to its low abundance and thus requires further validation.

We then used the developed pipeline to investigate the composition of birefringent liquid crystals that have been previously associated with NASH progression. We discovered a high spatial correlation between the birefringent crystals and saturated CE by comparing SRS images and polarization images of the same tissues. This finding is supported by previous studies reporting that CE molecules can form liquid crystalline lattices in lipid droplets.[279] Indeed, we have observed the emergence of liquid crystals with typical “Maltese crosses” in liver biopsies of animal models of NASH preceding the onset of inflammation and fibrosis.[278] The strong spatial correlation indicates that the main composition of these birefringent liquid crystals is saturated CE, suggesting that the presence and the fate of saturated CE (e.g., lipolysis, phase equilibrium, and phase transition of cholesterol) may also play a vital role in NASH progression. It is important to note that the spatial correlation between the polarization and SRS images is reduced by two factors: one being the imaging depth mismatch between the polarized light and SRS microscopy systems, and the other is that other components, mainly collagen, also generate birefringent signals in the polarization images. In polarization images, the collagen signals can overlap with signals of the birefringent crystals of interest, hindering the visualization of crystal distribution. Our developed SRS imaging and analysis system addressed this problem by separating signals from non-lipid components, such as collagen, to only focus on lipid molecules. With the spatially resolved capability of SRS imaging, we observed that some small regions in clinically diagnosed NAFL tissue sections contain accumulated saturated CE, which are potential indicators of NASH development. Future studies will focus on elucidating the origin of saturated CE aggregation in lipid droplets and its role in the pathogenesis of NASH. The SRS microscopy platform can be used to test specific hypotheses of lipotoxicity and may have potential clinical applications in the future if SRS "markers" associated with clinical outcomes are identified.[262–264]

Our work has some limitations. We only focused on free cholesterol, cholesterol esters (saturated and unsaturated), and triglycerides (of different saturation levels) in this work. Due to their lower percentages in examined NAFLD tissues (~3% TAG), the classification of TAG containing only saturated FAs, i.e., saturated TAG, was not included in this work. The Raman spectral difference between saturated TAG and other lipid species has been explored in previous studies. As Czamara et al. reported, although saturated TAG has a similar Raman spectrum as saturated CE in the C–H stretching region with subtle peak shifts and relative peak intensity differences, they have significant spectral differences in the C=C/C=O stretching region in the fingerprint window. Specifically, saturated TAG has no peak near 1660 cm^{-1} due to a lack of C=C bond and has double peaks at 1743 cm^{-1} and 1729 cm^{-1}.[280] Leveraging these spectral differences, classification of saturated TAG can also be achieved using the SRS spectral unmixing algorithm. Moreover, future studies can expand the SRS technique to explore other lipid species, such as free fatty acids and phospholipids. However, it is important to note that there is a limitation in the number of lipid species that can be classified by SRS imaging depending on the spectral difference between different lipid molecules. Increasing the spectral window in the fingerprint region may help, but due to the limited sensitivity of SRS imaging, it is difficult to reliably quantify lipid species with a molar percentage at the level of or below 5%. Therefore, while SRS imaging is not a substitute for other techniques such as lipidomics in the comprehensive profiling of lipids, it can be used in conjunction with lipidomics to provide complementary spatial information and a more detailed characterization of the lipid composition in NAFLD tissues. In conclusion, we believe that the SRS imaging and analysis pipeline we developed provides a valuable tool for characterizing the spatial distribution of different lipid species in human liver sections, which appear to be inhomogeneous in NAFL/NASH. It offers great potential for gaining new insights into the molecular mechanisms of the progression from NAFL to NASH.

CHAPTER 6. INVESTIGATION OF LIPID PEROXIDATION IN CELL FERROPTOSIS USING STIMULATED RAMAN SCATTERING MICROSCOPY

6.1 INTRODUCTION

In this chapter, we demonstrate another unique and powerful capability of SRS microscopy by leveraging its spectral analysis capabilities to investigate chemical reaction mechanisms, specifically focusing on lipid metabolism during cell ferroptosis. Ferroptosis is an iron-dependent, lipid peroxidation-driven form of regulated cell death that is distinct from other types of cell death, such as apoptosis, necrosis, and autophagy.[281–284] Unlike these other forms of cell death, ferroptosis is characterized by the accumulation of lipid peroxides within a cell, ultimately leading to oxidative damage and permeabilization of cellular membranes.[285] This process is dependent on iron, which acts as a catalyst in the formation of reactive oxygen species (ROS) through Fenton chemistry, which drives the peroxidation of polyunsaturated fatty acids (PUFAs) within membrane phospholipids.[286] Glutathione peroxidase 4 (GPX4) is a critical enzyme that inhibits ferroptosis by reducing lipid hydroperoxides to their corresponding alcohols, thereby preventing the accumulation of toxic lipid peroxides.[287] RSL3 is a small molecule that directly inhibits GPX4, thereby promoting the accumulation of lipid peroxides and inducing ferroptosis.[288]

Lipid peroxidation is a free radical-mediated process that proceeds through three main steps: initiation, propagation, and termination.[289–292] The initiation step involves the formation of a lipid radical (R•), which occurs when a PUFA is attacked by a reactive radical species, such as a hydroxyl radical (•OH), leading to the abstraction of a hydrogen atom. The propagation step is the core of lipid peroxidation, during which lipid peroxyl radicals (ROO•) are generated and propagate the chain reaction. This step can occur through two potential mechanisms. The first mechanism is hydrogen atom transfer (HAT), in which a lipid peroxyl radical (ROO•) abstracts a hydrogen atom from a neighboring lipid molecule (RH), forming a new lipid radical (R•) and lipid hydroperoxide (ROOH). The newly formed lipid radical can react with another oxygen molecule to form another peroxyl radical, thereby continuing the chain reaction. The second potential mechanism is peroxyl radical addition (PRA), during which the lipid peroxyl radical (ROO•) adds directly to the double bond of another lipid molecule, resulting in the formation of a more stable, conjugated radical. The PRA mechanism often leads to the formation of electrophilic lipid species, which are highly reactive and can modify proteins and other cellular components, contributing significantly to cytotoxicity.[293–295] This cycle of hydrogen abstraction and radical formation is a defining feature of the propagation phase and leads to the spread of lipid peroxidation across the cellular membrane. Finally, the termination step of lipid peroxidation occurs when two radical species react to form a non-radical product, effectively halting the chain reaction. This step often requires the presence of antioxidants, such as vitamin E (α-tocopherol), which donate a hydrogen atom to lipid peroxyl radicals, thereby preventing further propagation.[296]

Previous studies have demonstrated that different exogenous lipids can either protect against or promote lipid peroxidation and ferroptosis in cells. For instance, monounsaturated fatty acids (MUFAs) have been shown to inhibit ferroptosis by preventing lipid ROS accumulation at the plasma membrane.[297,298] Nonconjugated PUFAs, such as linoleic acid (NLA 18:2) and arachidonic acid (AA 20:4), have been shown to sensitize cells to ferroptosis due to their susceptibility to oxidation via HAT, which leads to the formation of lipid peroxyl radicals. Conjugated PUFAs, such as conjugated linoleic acid (CLA 18:2), have exhibited a higher cytotoxicity than nonconjugated PUFAs, possibly due to their propensity to undergo oxidation via peroxyl radical addition. It has been shown that oxidation via PRA proceeds at a much faster rate than oxidation via HAT.[294] These findings collectively suggest that the structure of fatty acids, specifically the presence of conjugated versus nonconjugated double bonds in PUFAs, plays a crucial role in determining their reactivity and impact on ferroptosis.

Despite current findings, most of the techniques used to study lipid peroxidation and ferroptosis are still limited. Many of these methods, such as cell viability assays, rely on bulk measurements that average signals across large populations of cells, obscuring important heterogeneity at the single-cell level. Additionally, endpoint assays, such as lipidomics and fluorescence-based detection of lipid peroxides, provide only static snapshots of lipid peroxidation, lacking the ability to capture the dynamic nature of lipid oxidation and cell death processes.[299,300] The required extensive sample processing or staining for these techniques may alter the targeted chemicals, biasing the results. These limitations highlight the need for new approaches that can provide real-time, spatially resolved information on lipid peroxidation in live cells. Recently, stimulated Raman scattering (SRS) microscopy, a label-free, vibrational imaging technique, has demonstrated its great potential in visualizing the subcellular lipid peroxidation reaction sites in cells.[301] In this work, we propose to leverage SRS's capability of detecting and quantifying specific chemical bonds within biological environments to monitor changes in lipid composition and oxidation states at the subcellular level. Specifically, we aim to use SRS microscopy to differentiate between the peroxidation mechanisms of conjugated and nonconjugated PUFAs, providing valuable experimental evidence on their distinct chemical bond changes during lipid peroxidation.

6.2 METHODS AND MATERIALS

6.2.1 *Hyperspectral SRS microscopy*

The hyperspectral SRS microscopy setup has been reported in detail in our previous work.[21] Briefly, a broadband femtosecond dual beam laser system (Spectra-Physics Insight DS+) outputs a wavelength-tunable beam (pump) and a fixed beam at 1040 nm (Stokes) at an 80 MHz repetition rate. The pump beam is chirped to approximately 3 ps with high-dispersion SF11 dense flint glass rods (GR, Newlight Photonics). The Stokes beam is modulated at 20 MHz with an electro-optical modulator (EOM, Thorlabs) and coupled into a 4-m polarization-maintaining Yb-doped fiber (YB1200-10/125 DC-PM, Thorlabs) for parabolic amplification[22], then chirped to approximately 3 ps using a grating stretcher (GS, LightSmyth). The two beams are combined with a 1000 nm short pass (SP) dichroic mirror (Thorlabs) and temporally overlapped using a motorized delay stage (DS, Zaber X-DMQ-AE).

The synchronized laser beams are directed into a home-built upright laser scanning microscope equipped with a 40× water immersion objective (Nikon N40XLWD-NIR, NA = 1.15) and an oil immersion condenser (Nikon MEL41410, NA = 1.4). The pump beam is isolated with a 1000 nm SP filter (Thorlabs) and detected by an amplified Si photodiode (PD). The signal is then demodulated with a lock-in amplifier (LIA, Zurich Instruments H2FLI) with a time constant of 4 μs to generate 512 × 512-pixel SRS images. For SRS imaging of the HT-1080 cells, 40 mW of the pump beam at 800 nm for C–H, 851 nm for C–D, and 887 nm for fingerprint region, and 72 mW of the Stokes beam were used.

6.2.2 *Cell culture and slide preparation*

HT1080 cells (ATCC) were cultured in high-glucose DMEM containing 10% fetal bovine serum and 1% penicillin-streptomycin (Gibco). One day prior to imaging, cells were seeded at a density of 1.2×10^3 cells per well in 8-well glass bottom chamber slides (ThermoFisher). The cells were allowed to adhere to the slide for 8 hours, and then media was replaced with media containing 80 uM lipid. All lipids in this study were obtained from Cayman Chemical. On the day of imaging, the media was replaced with media containing 50 nM RSL3 and incubated for 0-4 hours. Once treatment was complete, the media was aspirated and slides were rinsed with phosphate buffered saline (PBS) (Gibco). The cells were fixed on the slides using 4% paraformaldehyde. PBS was added to the wells after fixation to prevent morphological changes associated with drying.

6.3 PRELIMINARY RESULTS

6.3.1 *SRS imaging of cells undergoing RSL3-induced ferroptosis*

Our preliminary results show that SRS microscopy can effectively visualize lipid droplets and track the process of lipid peroxidation in live cells (Figure 6.1). HT-1080 cells were treated with RSL3 for 0-4 hours. The cells were imaged with the SRS setup demonstrated in Figure 6.1A immediately after fixation. An interesting feature we observed is illustrated in Figure 6.1B. In a small population of cells, small hollow features began to form in the cell cytoplasm with RSL3 treatment. As the RSL3 treatment time increased, this phenomenon progressed and caused more and bigger holes to form. Although this observation has not been reported previously, we hypothesize that these holes indicate damaged ER membranes since ER has been reported as the primary site for lipid peroxidation.[301]

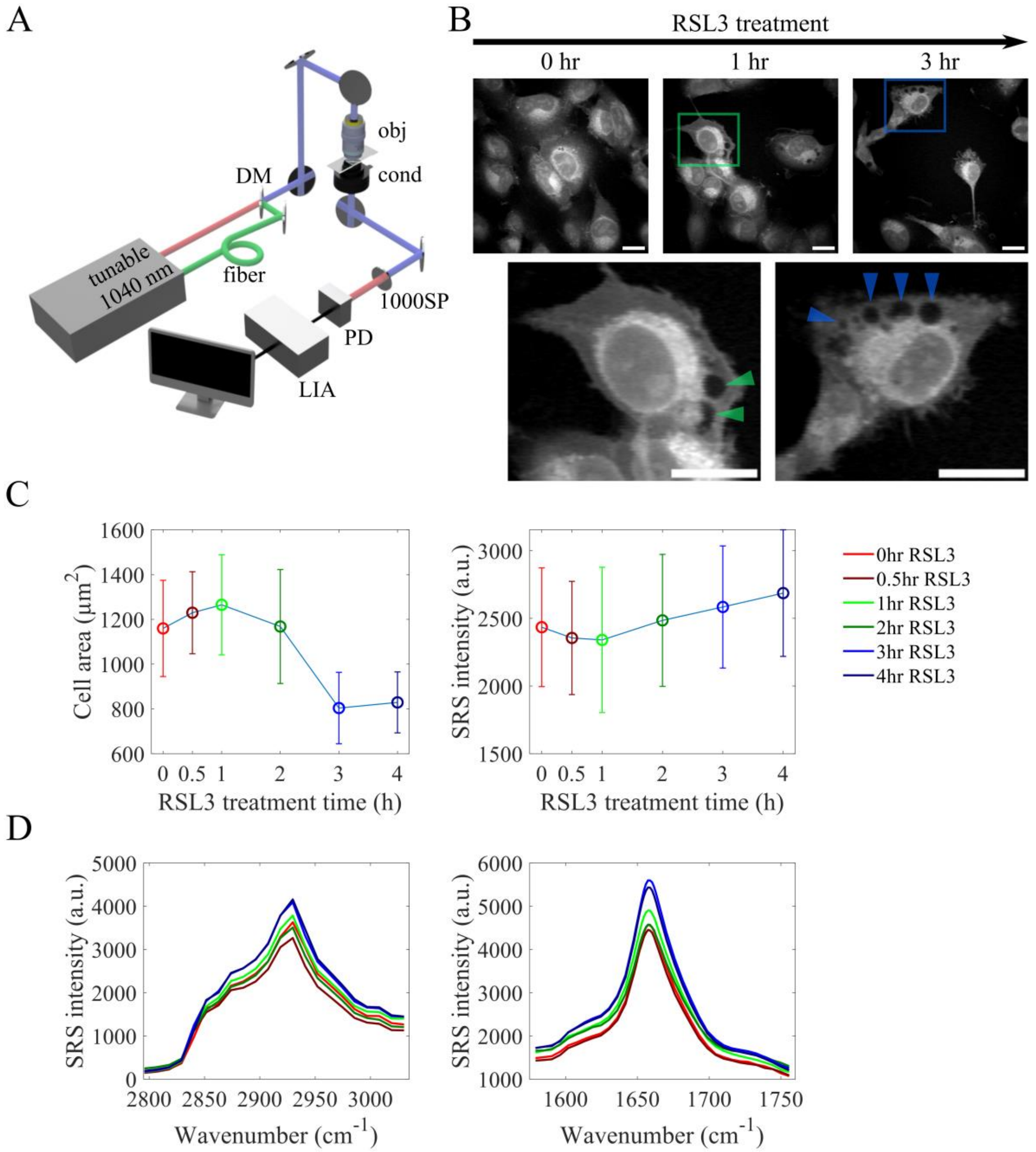

Figure 6.1. SRS imaging of HT-1080 cells during RSL3-induced ferroptosis. (A) Schematic diagram of the SRS microscopy system. (B) SRS images show the morphological changes during ferroptosis, with arrows indicating holes formed in the cell cytoplasm. (C) Cell area change (left) and 2930 cm^{-1} C-H SRS intensity change (right) during RSL3 treatment, with error bars showing standard deviations. (D) Averaged SRS spectra of cell cytoplasm in the C-H stretching (left) and amide (right) regions. Scale bars: 20 μm.

Another notable change during RSL3-induced ferroptosis is cell size. As presented in Figure 6.1C, the cell area remained consistent with a small increase during the first 2 hours, then decreased significantly after 3-4 hours of treatment. During the later 2 hours of treatment, the majority of cells shrank and started to round up, which is an indication of cell death.[302] The corresponding cell intensity change shows an opposite trend. The cell intensity slightly decreased and then increased with increased RSL3 treatment time. This trend could be attributed to two factors. The first factor is the change in the cell area. When the cells were flattened out, the averaged SRS intensity of the whole cell was lower compared to when the cells rounded up. The other factor is lipid droplet (LD) formation, a reported phenomenon during the early stage of ferroptosis[303], which leads to an increase in SRS intensity.

Since the onset of lipid peroxidation primarily occurs in organelles within the cell cytoplasm[301], we segmented out the cell cytoplasm regions and illustrated their C-H stretching region (2800 – 3035 cm^{-1}) and amide region (1575 – 1760 cm^{-1}) SRS spectra in Figure 6.1D. The RSL3 treatment did not introduce notable spectral shifts. The cell cytoplasm intensity changes in both spectral regions followed a similar trend as the whole cell signal intensity change.

6.3.2 *Lipid peroxidation of conjugated PUFAs*

To investigate the different peroxidation reaction mechanisms and potential products of conjugated versus nonconjugated PUFAs, we first incubated HT-1080 cells with conjugated linoleic acid (CLA 18:2) overnight before RSL3 treatment and SRS imaging. The SRS images of CLA-incorporated cells are shown in Figure 6.2A. Compared to control cells without exogenous lipids (Figure 6.1B), CLA-incorporated cells demonstrate significantly higher cytotoxicity with severe cell shrinkage and loss of cellular content, especially after 4 hours of RSL3 treatment. This is also reflected in Figure 6.2B, in which the cell cytoplasm SRS intensity decreased with a longer treatment time. This observation is likely caused by the higher reactivity of conjugated PUFAs towards oxidation than their non-conjugated counterparts, as they preferentially undergo oxidation via peroxyl radical addition rather than hydrogen atom transfer (Figure 6.2D).

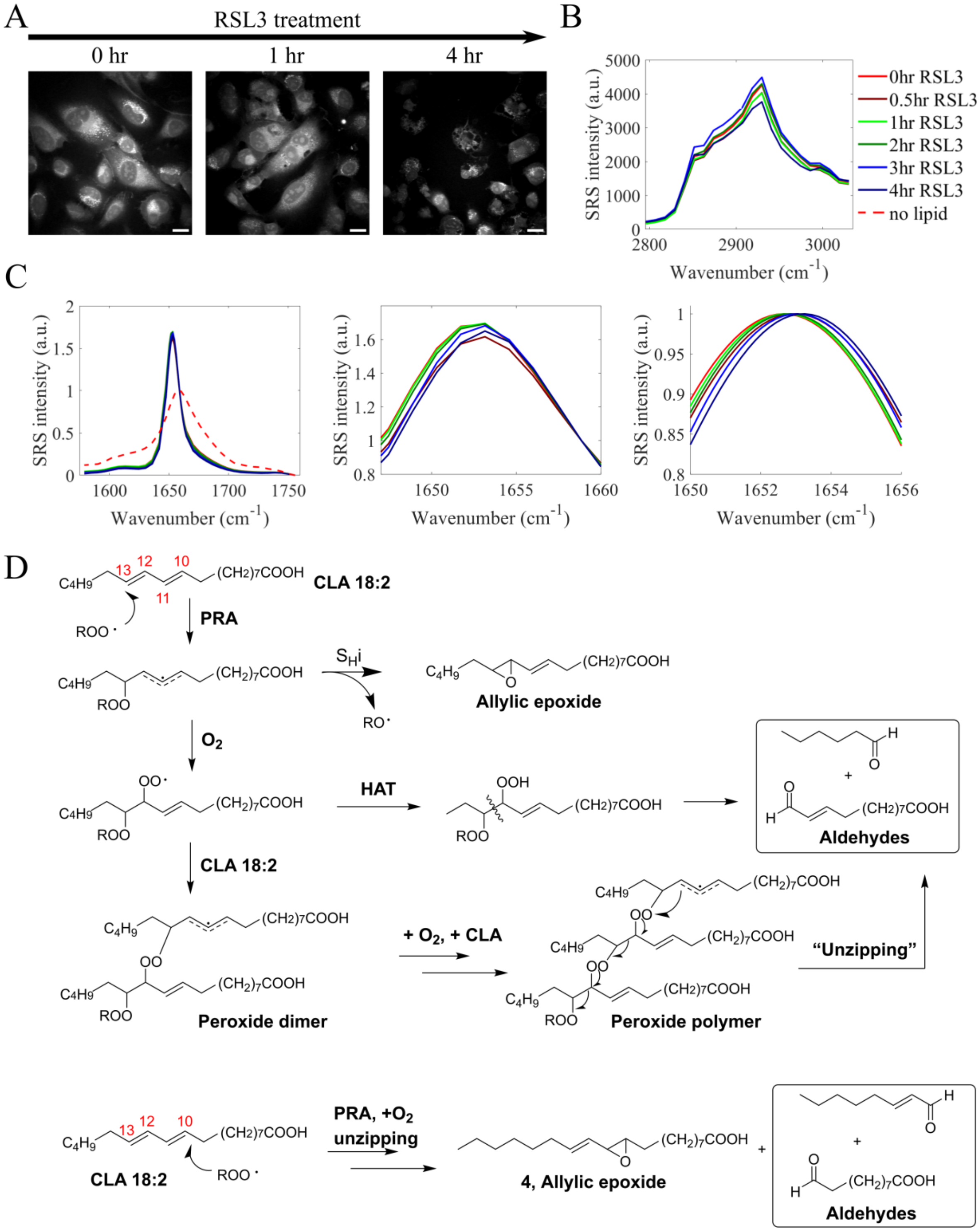

Figure 6.2. SRS imaging of lipid peroxidation of conjugated linoleic acid (CLA 18:2). (A) SRS images of CLA-incorporated cells during RSL3 treatment. (B) Cell cytoplasm SRS spectra in the C-H stretching region. (C) Normalized SRS spectra of cell cytoplasm in the C=C/amide region. Left: SRS spectra normalized by the amide peak for visualizing lipid-to-protein ratio. Middle: Zoomed in on the CLA peak of the normalized spectra. Right: Normalized CLA peak with Lorentzian fitting to visualize the spectral shift induced by lipid peroxidation. (D) Proposed oxidation mechanisms and products of CLA.

CLA has a strong conjugated C=C SRS peak at 1653 cm^{-1}, which induces a shift and a significant intensity increase in the cell cytoplasm SRS spectra in CLA-incorporated cells. To visualize the lipid-to-protein ratio change during lipid peroxidation, we normalized the cell cytoplasm C=C/amide SRS spectra by the amide peak. As demonstrated in Figure 6.2C, the lipid-to-protein ratio, in general, decreased as RSL3 treatment time increased, indicating the degradation and peroxidation of the lipid. We applied Lorentzian fitting to smooth the SRS spectra for better visualization of the lipid spectral shift. A longer RSL3 treatment time leads to a blue shift of the lipid peak. This trend shows the loss of the conjugated C=C bond, which aligns with our expected mechanisms shown in Figure 6.2D.

6.3.3 *Lipid peroxidation of nonconjugated PUFAs*

The NLA C=C peak overlaps with the amide peak at 1656 cm^{-1}, as shown in Figure 6.3C. In order to dissect the effects of peroxidation on NLA from the contribution of amide spectral information, we employed C_{13}-NLA, which has its C=C peak at ~1598 cm^{-1}, well-separated from the amide peak. Although the overall cell intensity change was less than in CLA-incorporated cells (Figure 6.3A-B), we also observed a lipid-to-protein ratio decrease (Figure 6.3D). Interestingly, the NLA C=C peak exhibits a slight blue shift as RSL3 treatment time increases. The primary hydroperoxide product of HAT-mediated peroxidation has a conjugated double bond (Figure

6.3E), which would lead to a red shift of the peak. We hypothesize that the primary hydroperoxides then undergo PRA oxidation, forming a more complicated hydroperoxide product. The strong electron withdrawing group can lead to a blue shift of the lipid peak, which matches what we observed experimentally in NLA-incorporated cells. Further investigations are needed to validate our proposed oxidation mechanism (Figure 6.3E).

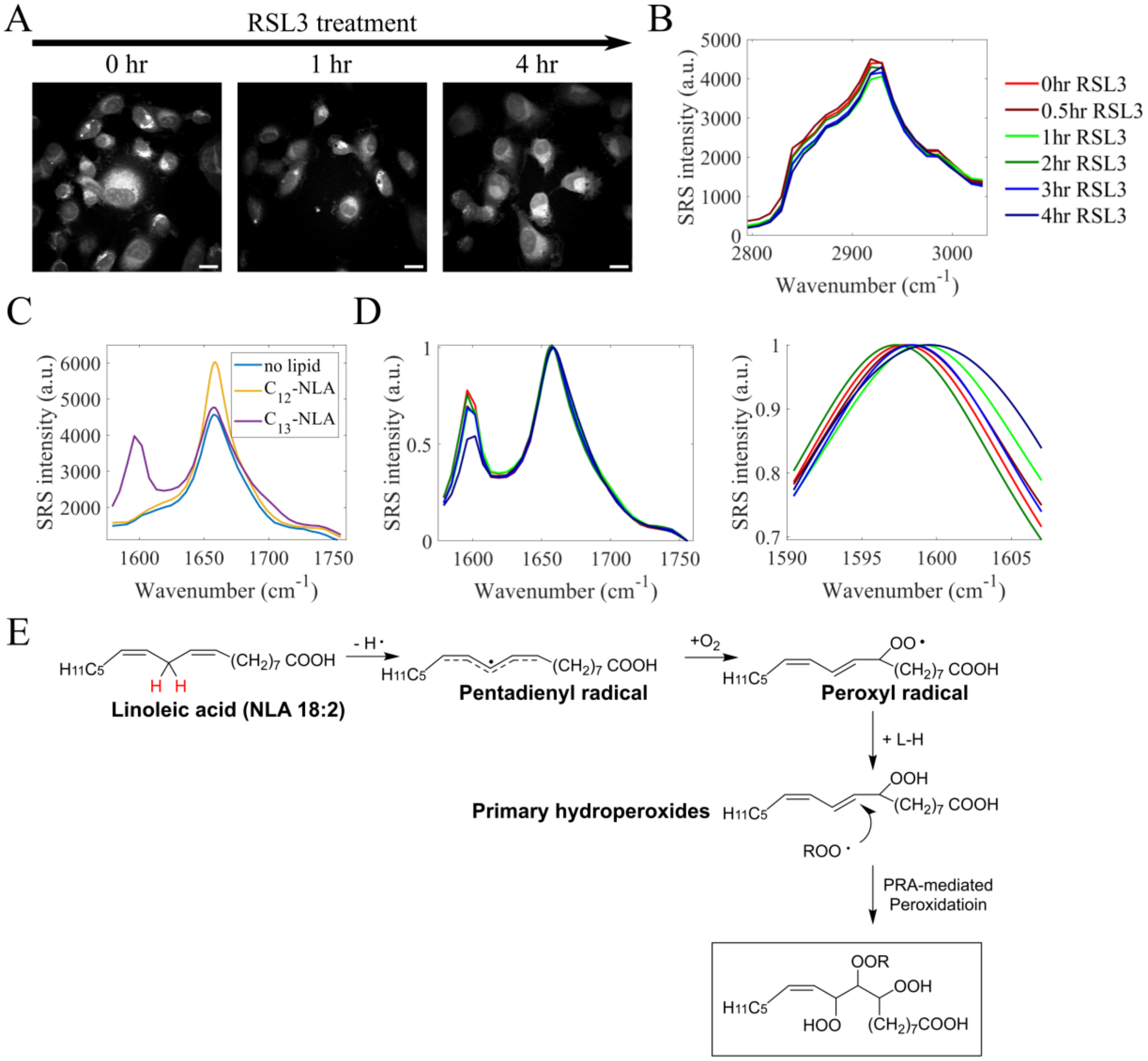

Figure 6.3. SRS imaging of lipid peroxidation of nonconjugated linoleic acid (NLA 18:2). (A) SRS images of NLA-incorporated cells during RSL3 treatment. (B) Cell cytoplasm SRS spectra in the C-H stretching region. (C) Spectral difference of cells incorporating C_{12} or C_{13}-NLA. (D) Normalized SRS spectra of C_{13}-NLA-incorporated cell cytoplasm in the C=C/amide region. Right:

C_{13}-NLA peak with Lorentzian fitting to visualize the spectral shift induced by lipid peroxidation. (E) Proposed oxidation mechanisms and products of NLA.

6.4 SUMMARY OF PRELIMINARY RESULTS AND NEXT STEPS

We observed that cells treated with conjugated linoleic acid (CLA 18:2) exhibited higher levels of cytotoxicity compared to cells treated with nonconjugated linoleic acid (NLA 18:2) or vehicle control. Furthermore, subtle shifts in the Raman peak positions corresponding to C=C bonds were detected, indicating changes in the conjugation state of lipids during peroxidation. Specifically, we observed a blue shift in the lipid peak, which indicates the loss of conjugation during peroxidation. We also discovered a blue shift in the NLA peak, the cause of which requires further investigation. These findings demonstrate the potential of SRS microscopy to provide new insights into the mechanisms of lipid peroxidation and ferroptosis, particularly with respect to the unique reactivity of conjugated versus nonconjugated PUFAs.

By revealing how different fatty acids undergo distinct chemical transformations during lipid peroxidation, our approach offers new insights into the molecular underpinnings of ferroptosis. This knowledge is crucial for understanding how lipid metabolism influences cell fate and for identifying new therapeutic strategies to modulate ferroptosis in diseases such as cancer and neurodegeneration.

CHAPTER 7. CONCLUSIONS AND FUTURE DIRECTIONS

7.1 DISSERTATION SUMMARY

This dissertation presents significant advancements in stimulated Raman scattering (SRS) microscopy and its applications in protein and lipid metabolism studies. The work described across the chapters highlights the potential of SRS microscopy as a versatile and powerful tool for investigating complex biological systems with high spatial, temporal, and chemical resolution, providing novel insights at cellular and molecular scales and demonstrating its unique capabilities in biomedical applications.

In Chapter 2, we introduced a novel multi-channel SRS microscopy system capable of simultaneous imaging in two distinct spectral regions. This system, developed using a femtosecond laser combined with dual-output tunable optical parametric oscillators (OPOs), enables hyperspectral imaging with significantly expanded spectral coverage. By eliminating the need for sequential wavelength tuning, the system enhances imaging speed, reproducibility, and reliability, addressing key limitations of conventional SRS microscopy. These improvements allow for more accurate quantification of both chemical and morphological features in biological samples. This dual-band system was applied to visualize and quantify fatty acid accumulation, drug uptake, and lipid unsaturation levels, demonstrating its potential for concurrent spatial and biochemical analysis. This technological advancement sets the stage for the subsequent applications explored in this dissertation.

Chapters 3 and 4 focused on protein metabolism, specifically leveraging SRS microscopy to study cell growth rates and drug response in 2D and 3D microenvironments. In Chapter 3, we developed a ratiometric SRS imaging-based technique utilizing deuterium-labeled amino acids to quantify protein synthesis rates at the single-cell level. This approach offered a robust and rapid method for evaluating drug responses with a short turnaround time, providing complementary insights to traditional cell viability and proliferation assays. Chapter 4 extended this methodology to compare intracellular drug uptake and growth inhibition in 2D monolayer cells and 3D spheroids, uncovering critical differences in their drug-cell interactions driven by intricate microenvironmental factors in 3D cultures. These results highlight the importance of studying cellular responses using physiologically relevant models during drug discovery and testing.

In Chapter 5, we shifted our focus to lipid metabolism, where SRS microscopy was employed to analyze lipid composition and spatial distribution in liver tissue sections from patients with different stages of nonalcoholic fatty liver disease (NAFLD). Utilizing dual-band hyperspectral SRS imaging, we mapped key lipid species, including free cholesterol, saturated and unsaturated cholesterol esters, and triglycerides, correlating their distributions with disease progression. This study showcases the ability of SRS microscopy to provide spatially resolved biochemical information, offering new insights into lipid metabolism and its dysregulation in metabolic disorders.

Chapter 6 explored the promising capability of SRS microscopy to investigate chemical reaction mechanisms, with a focus on lipid peroxidation during ferroptosis. By analyzing subtle spectral shifts associated with the oxidation of polyunsaturated fatty acids (PUFAs), we identified distinct chemical pathways linked to different conjugation levels in PUFAs. This study provided valuable insights into the molecular mechanisms underlying ferroptosis, advancing our understanding of how lipid oxidation contributes to this regulated cell death process. These findings demonstrated the potential of SRS microscopy to leverage its spectral analysis capabilities for detailed mechanism studies, broadening its applications in biochemical research.

Collectively, this dissertation showcases the tremendous potential of SRS microscopy in life sciences, addressing critical challenges in studying metabolic processes and enabling novel applications in complex biomedical research.

7.2 FUTURE DIRECTIONS

The advancements presented in this dissertation pave the way for expanding the capabilities of SRS microscopy in future research. The noninvasive and label-free nature of SRS microscopy makes it ideal for monitoring dynamic biological processes, including cell-drug interactions, in real time. Spectral focusing SRS is particularly well-suited for studying rapid biochemical changes, such as lipid remodeling or protein synthesis, by enabling fast delay adjustments and arbitrary discrete spectral sampling. This approach provides unparalleled insights into time-sensitive processes like cell division, signal transduction, and drug responses. Additionally, SRS microscopy can be utilized to track disease progression or evaluate drug efficacy dynamically, making it a powerful tool for studying cellular responses to environmental changes.

SRS microscopy's compatibility with tissue and organoid imaging presents unique opportunities for studying complex biological systems. Patient-derived organoids, which mimic tissue structures and functions, serve as robust models for disease research and drug development.[304,305] SRS imaging provides spatially resolved metabolic information in these models, complementing traditional assays for evaluating therapeutic responses. Furthermore, with epi-detection setups, SRS microscopy could be extended to in vivo studies, enabling real-time monitoring of metabolic processes in animal models and bridging the gap between preclinical studies and clinical applications.

Integrating SRS with complementary techniques creates a comprehensive platform for studying biological systems, driving innovation in both fundamental research and translational applications.

One critical integration is coupling SRS microscopy with fluorescence microscopy. While fluorescence microscopy excels in sensitivity and specificity, SRS microscopy provides label-free imaging of endogenous molecules. Combining these techniques enables simultaneous mapping of labeled and unlabeled targets, facilitating a deeper understanding of metabolic pathways. For instance, fluorescence microscopy can track specific biomolecules or cellular structures, while SRS provides complementary information on broader morphological and biochemical contexts.[122] Additionally, combining SRS with live-dead staining assays can decouple measurements of cell viability and growth, offering richer insights into cellular responses to treatments. This dual-modality approach is particularly valuable for studying protein-lipid interactions, drug localization, and metabolic dynamics in cells and tissues.

The integration of SRS microscopy with omics technologies, such as proteomics and lipidomics, further enhances its utility. Proteomics enables comprehensive profiling of protein expression and post-translational modifications, while lipidomics provides detailed quantification of lipid species and molecular composition. When combined with the spatial resolution of SRS, these approaches bridge molecular and spatial information, offering a multidimensional view of metabolic processes. For example, correlating SRS imaging data with mass spectrometry-based proteomics could reveal how protein localization influences functional pathways in disease progression. Similarly, combining SRS with lipidomics could elucidate the interplay between lipid spatial distribution and metabolic regulation, providing critical insights into diseases like NAFLD and cardiovascular disorders.

In addition, integrating SRS microscopy with transcriptomics offers new opportunities for comprehensive studies of metabolic regulation.[306] Transcriptomics reveals changes in gene expression that drive metabolic alterations, while SRS maps the spatial and biochemical outcomes of these changes. This combination could elucidate how genetic regulation influences metabolic phenotypes, offering insights into disease mechanisms or therapeutic responses. For instance, correlating transcriptomic profiles with SRS imaging could uncover connections between gene expression patterns and localized biochemical alterations in cells and tissues, advancing our understanding of cellular and molecular processes.

Finally, the incorporation of artificial intelligence (AI) into SRS microscopy presents immense potential for advancing its capabilities. AI-driven tools can enhance image quality through denoising or unmixing spectral data, enabling faster and more accurate identification of different molecular species.[142] Deep learning models can predict biochemical patterns from sparse data, facilitating high-throughput studies of metabolic pathways.[307] Moreover, AI-based algorithms can support automated classification of cellular organelles, identification of disease-specific biomarkers, and efficient analysis of large datasets.[144] These capabilities significantly broaden the scope of SRS microscopy applications in biomedical research.

In conclusion, integrating SRS microscopy with complementary techniques such as fluorescence microscopy, omics technologies, transcriptomics, and AI offers a pathway for exciting advancements in biomedical research. These combinations provide a more comprehensive understanding of biological systems, driving innovation in studying protein and lipid metabolism, disease mechanisms, and therapeutic development. The future of SRS microscopy lies in its ability to evolve and integrate with emerging technologies, solidifying its role as a cornerstone technique in life sciences.

BIBLIOGRAPHY

(1) Horn, A.; Jaiswal, J. K. Structural and Signaling Role of Lipids in Plasma Membrane Repair. *Curr Top Membr* **2019**, *84*, 67–98. https://doi.org/10.1016/bs.ctm.2019.07.001.

(2) Ayala, A.; Muñoz, M. F.; Argüelles, S. Lipid Peroxidation: Production, Metabolism, and Signaling Mechanisms of Malondialdehyde and 4-Hydroxy-2-Nonenal. *Oxidative Medicine and Cellular Longevity* **2014**, *2014*, e360438. https://doi.org/10.1155/2014/360438.

(3) Zhu, J.; Thompson, C. B. Metabolic Regulation of Cell Growth and Proliferation. *Nat Rev Mol Cell Biol* **2019**, *20* (7), 436–450. https://doi.org/10.1038/s41580-019-0123-5.

(4) Agathocleous, M.; Harris, W. A. Metabolism in Physiological Cell Proliferation and Differentiation. *Trends in Cell Biology* **2013**, *23* (10), 484–492. https://doi.org/10.1016/j.tcb.2013.05.004.

(5) Krycer, J. R.; Sharpe, L. J.; Luu, W.; Brown, A. J. The Akt–SREBP Nexus: Cell Signaling Meets Lipid Metabolism. *Trends in Endocrinology & Metabolism* **2010**, *21* (5), 268–276. https://doi.org/10.1016/j.tem.2010.01.001.

(6) Castano, A. P.; Demidova, T. N.; Hamblin, M. R. Mechanisms in Photodynamic Therapy: Part Two—Cellular Signaling, Cell Metabolism and Modes of Cell Death. *Photodiagnosis and Photodynamic Therapy* **2005**, *2* (1), 1–23. https://doi.org/10.1016/S1572-1000(05)00030-X.

(7) Song, G.; Ouyang, G.; Bao, S. The Activation of Akt/PKB Signaling Pathway and Cell Survival.

(8) Alberts, B.; Johnson, A.; Lewis, J.; Raff, M.; Roberts, K.; Walter, P. The Shape and Structure of Proteins. In *Molecular Biology of the Cell. 4th edition*; Garland Science, 2002.

(9) Merrick, W. C. Mechanism and Regulation of Eukaryotic Protein Synthesis. *Microbiological Reviews* **1992**, *56* (2), 291–315. https://doi.org/10.1128/mr.56.2.291-315.1992.

(10) Rusilowicz-Jones, E. V.; Urbé, S.; Clague, M. J. Protein Degradation on the Global Scale. *Molecular Cell* **2022**, *82* (8), 1414–1423. https://doi.org/10.1016/j.molcel.2022.02.027.

(11) Yoon, H.; Shaw, J. L.; Haigis, M. C.; Greka, A. Lipid Metabolism in Sickness and in Health: Emerging Regulators of Lipotoxicity. *Molecular Cell* **2021**, *81* (18), 3708–3730. https://doi.org/10.1016/j.molcel.2021.08.027.

(12) Sunshine, H.; Iruela-Arispe, M. L. Membrane Lipids and Cell Signaling. *Curr Opin Lipidol* **2017**, *28* (5), 408–413. https://doi.org/10.1097/MOL.0000000000000443.

(13) Jeon, Y. G.; Kim, Y. Y.; Lee, G.; Kim, J. B. Physiological and Pathological Roles of Lipogenesis. *Nat Metab* **2023**, *5* (5), 735–759. https://doi.org/10.1038/s42255-023-00786-y.

(14) Grabner, G. F.; Xie, H.; Schweiger, M.; Zechner, R. Lipolysis: Cellular Mechanisms for Lipid Mobilization from Fat Stores. *Nat Metab* **2021**, *3* (11), 1445–1465. https://doi.org/10.1038/s42255-021-00493-6.

(15) Bolsoni-Lopes, A.; Alonso-Vale, M. I. C. Lipolysis and Lipases in White Adipose Tissue - An Update. *Arch Endocrinol Metab* **2015**, *59* (4), 335–342. https://doi.org/10.1590/2359-3997000000067.

(16) Mallick, R.; Basak, S.; Duttaroy, A. K. Fatty Acids and Evolving Roles of Their Proteins in Neurological, Cardiovascular Disorders and Cancers. *Progress in Lipid Research* **2021**, *83*, 101116. https://doi.org/10.1016/j.plipres.2021.101116.

(17) Wu, X.; Xu, M.; Geng, M.; Chen, S.; Little, P. J.; Xu, S.; Weng, J. Targeting Protein Modifications in Metabolic Diseases: Molecular Mechanisms and Targeted Therapies. *Sig Transduct Target Ther* **2023**, *8* (1), 1–45. https://doi.org/10.1038/s41392-023-01439-y.

(18) Shamim, A.; Mahmood, T.; Ahsan, F.; Kumar, A.; Bagga, P. Lipids: An Insight into the Neurodegenerative Disorders. *Clinical Nutrition Experimental* **2018**, *20*, 1–19. https://doi.org/10.1016/j.yclnex.2018.05.001.

(19) Yan, X.; Hu, Y.; Wang, B.; Wang, S.; Zhang, X. Metabolic Dysregulation Contributes to the Progression of Alzheimer's Disease. *Front Neurosci* **2020**, *14*, 530219. https://doi.org/10.3389/fnins.2020.530219.

(20) Jp, L. Q.; Ka, S.; M, B.; Ae, W. Dysregulation of Protein Synthesis and Disease. *The Journal of pathology* **2010**, *220* (2). https://doi.org/10.1002/path.2627.

(21) Marchingo, J. M.; Cantrell, D. A. Protein Synthesis, Degradation, and Energy Metabolism in T Cell Immunity. *Cell Mol Immunol* **2022**, *19* (3), 303–315. https://doi.org/10.1038/s41423-021-00792-8.

(22) Song, P.; Yang, F.; Jin, H.; Wang, X. The Regulation of Protein Translation and Its Implications for Cancer. *Signal Transduct Target Ther* **2021**, *6*, 68. https://doi.org/10.1038/s41392-020-00444-9.

(23) Chen, H.-H.; Tarn, W.-Y. uORF-Mediated Translational Control: Recently Elucidated Mechanisms and Implications in Cancer. *RNA Biol* **2019**, *16* (10), 1327–1338. https://doi.org/10.1080/15476286.2019.1632634.

(24) Yuan, W.; Zhang, R.; Lyu, H.; Xiao, S.; Guo, D.; Zhang, Q.; Ali, D. W.; Michalak, M.; Chen, X.-Z.; Zhou, C.; Tang, J. Dysregulation of tRNA Methylation in Cancer: Mechanisms and Targeting Therapeutic Strategies. *Cell Death Discov.* **2024**, *10* (1), 1–19. https://doi.org/10.1038/s41420-024-02097-x.

(25) Pei, K.; Gui, T.; Kan, D.; Feng, H.; Jin, Y.; Yang, Y.; Zhang, Q.; Du, Z.; Gai, Z.; Wu, J.; Li, Y. An Overview of Lipid Metabolism and Nonalcoholic Fatty Liver Disease. *Biomed Res Int* **2020**, *2020*, 4020249. https://doi.org/10.1155/2020/4020249.

(26) Deprince, A.; Haas, J. T.; Staels, B. Dysregulated Lipid Metabolism Links NAFLD to Cardiovascular Disease. *Molecular Metabolism* **2020**, *42*, 101092. https://doi.org/10.1016/j.molmet.2020.101092.

(27) Linton, M. F.; Yancey, P. G.; Davies, S. S.; Jerome, W. G.; Linton, E. F.; Song, W. L.; Doran, A. C.; Vickers, K. C. The Role of Lipids and Lipoproteins in Atherosclerosis. In *Endotext*; Feingold, K. R., Anawalt, B., Blackman, M. R., Boyce, A., Chrousos, G., Corpas, E., de Herder, W. W., Dhatariya, K., Dungan, K., Hofland, J., Kalra, S., Kaltsas, G., Kapoor, N., Koch, C., Kopp, P., Korbonits, M., Kovacs, C. S., Kuohung, W., Laferrère, B., Levy, M., McGee, E. A., McLachlan, R., New, M., Purnell, J., Sahay, R., Shah, A. S., Singer, F., Sperling, M. A., Stratakis, C. A., Trence, D. L., Wilson, D. P., Eds.; MDText.com, Inc.: South Dartmouth (MA), 2000.

(28) Malekmohammad, K.; Bezsonov, E. E.; Rafieian-Kopaei, M. Role of Lipid Accumulation and Inflammation in Atherosclerosis: Focus on Molecular and Cellular Mechanisms. *Front. Cardiovasc. Med.* **2021**, *8*. https://doi.org/10.3389/fcvm.2021.707529.

(29) Alseekh, S.; Aharoni, A.; Brotman, Y.; Contrepois, K.; D'Auria, J.; Ewald, J.; C. Ewald, J.; Fraser, P. D.; Giavalisco, P.; Hall, R. D.; Heinemann, M.; Link, H.; Luo, J.; Neumann, S.; Nielsen, J.; Perez de Souza, L.; Saito, K.; Sauer, U.; Schroeder, F. C.; Schuster, S.; Siuzdak, G.; Skirycz, A.; Sumner, L. W.; Snyder, M. P.; Tang, H.; Tohge, T.; Wang, Y.; Wen, W.; Wu, S.; Xu, G.; Zamboni, N.; Fernie, A. R. Mass Spectrometry-Based Metabolomics: A

Guide for Annotation, Quantification and Best Reporting Practices. *Nat Methods* **2021**, *18* (7), 747–756. https://doi.org/10.1038/s41592-021-01197-1.

(30) Lee, D. Y.; Bowen, B. P.; Northen, T. R. Mass Spectrometry—Based Metabolomics, Analysis of Metabolite-Protein Interactions, and Imaging. *BioTechniques* **2010**, *49* (2), 557–565. https://doi.org/10.2144/000113451.

(31) Frick, M.; Schmidt, C. Mass Spectrometry—A Versatile Tool for Characterising the Lipid Environment of Membrane Protein Assemblies. *Chemistry and Physics of Lipids* **2019**, *221*, 145–157. https://doi.org/10.1016/j.chemphyslip.2019.04.001.

(32) Rae Buchberger, A.; DeLaney, K.; Johnson, J.; Li, L. Mass Spectrometry Imaging: A Review of Emerging Advancements and Future Insights. *Anal Chem* **2018**, *90* (1), 240–265. https://doi.org/10.1021/acs.analchem.7b04733.

(33) Vats, M.; Cillero-Pastor, B.; Cuypers, E.; A. Heeren, R. M. Mass Spectrometry Imaging in Plants, Microbes, and Food: A Review. *Analyst* **2024**, *149* (18), 4553–4582. https://doi.org/10.1039/D4AN00644E.

(34) Kubo, A.; Kajimura, M.; Suematsu, M. Matrix-Assisted Laser Desorption/Ionization (MALDI) Imaging Mass Spectrometry (IMS): A Challenge for Reliable Quantitative Analyses. *Mass Spectrom (Tokyo)* **2012**, *1* (1), A0004. https://doi.org/10.5702/massspectrometry.A0004.

(35) Zhang, H.; Lu, K. H.; Ebbini, M.; Huang, P.; Lu, H.; Li, L. Mass Spectrometry Imaging for Spatially Resolved Multi-Omics Molecular Mapping. *npj Imaging* **2024**, *2* (1), 1–15. https://doi.org/10.1038/s44303-024-00025-3.

(36) Zhang, H.; Delafield, D. G.; Li, L. Mass Spectrometry Imaging: The Rise of Spatially Resolved Single-Cell Omics. *Nat Methods* **2023**, *20* (3), 327–330. https://doi.org/10.1038/s41592-023-01774-6.

(37) Gilmore, I. S.; Heiles, S.; Pieterse, C. L. Metabolic Imaging at the Single-Cell Scale: Recent Advances in Mass Spectrometry Imaging. *Annu Rev Anal Chem (Palo Alto Calif)* **2019**, *12* (1), 201–224. https://doi.org/10.1146/annurev-anchem-061318-115516.

(38) Dong, Y.; Aharoni, A. Image to Insight: Exploring Natural Products through Mass Spectrometry Imaging. *Natural Product Reports* **2022**, *39* (7), 1510–1530. https://doi.org/10.1039/D2NP00011C.

(39) Sezgin, E.; Schwille, P. Fluorescence Techniques to Study Lipid Dynamics. *Cold Spring Harb Perspect Biol* **2011**, *3* (11), a009803. https://doi.org/10.1101/cshperspect.a009803.

(40) Mottillo, E. P.; Paul, G. M.; Moore, H.-P. H.; Granneman, J. G. Use of Fluorescence Microscopy to Probe Intracellular Lipolysis. *Methods Enzymol* **2014**, *538*, 263–278. https://doi.org/10.1016/B978-0-12-800280-3.00015-3.

(41) Elangovan, M.; Day, R. N.; Periasamy, A. Nanosecond Fluorescence Resonance Energy Transfer-Fluorescence Lifetime Imaging Microscopy to Localize the Protein Interactions in a Single Living Cell. *Journal of Microscopy* **2002**, *205* (1), 3–14. https://doi.org/10.1046/j.0022-2720.2001.00984.x.

(42) Kohnhorst, C. L.; Schmitt, D. L.; Sundaram, A.; An, S. Subcellular Functions of Proteins under Fluorescence Single-Cell Microscopy. *Biochimica et Biophysica Acta (BBA) - Proteins and Proteomics* **2016**, *1864* (1), 77–84. https://doi.org/10.1016/j.bbapap.2015.05.014.

(43) Yang, J.; Ning, J.; Sun, P.; Nie, Y.; Li, Y.; Guo, M.; Zhou, Y. Fluorescent Probes - Illuminate the Interplay Network between Lipid Droplets and Other Organelles.

Coordination Chemistry Reviews **2024**, *510*, 215792. https://doi.org/10.1016/j.ccr.2024.215792.

(44) D'Este, E.; Lukinavičius, G.; Lincoln, R.; Opazo, F.; Fornasiero, E. F. Advancing Cell Biology with Nanoscale Fluorescence Imaging: Essential Practical Considerations. *Trends in Cell Biology* **2024**, *34* (8), 671–684. https://doi.org/10.1016/j.tcb.2023.12.001.

(45) Thorn, K. Genetically Encoded Fluorescent Tags. *MBoC* **2017**, *28* (7), 848–857. https://doi.org/10.1091/mbc.e16-07-0504.

(46) Daemen, S.; van Zandvoort, M. A. M. J.; Parekh, S. H.; Hesselink, M. K. C. Microscopy Tools for the Investigation of Intracellular Lipid Storage and Dynamics. *Molecular Metabolism* **2016**, *5* (3), 153–163. https://doi.org/10.1016/j.molmet.2015.12.005.

(47) Gowda, G. A. N.; Raftery, D. NMR Based Metabolomics. *Adv Exp Med Biol* **2021**, *1280*, 19–37. https://doi.org/10.1007/978-3-030-51652-9_2.

(48) Hu, Y.; Cheng, K.; He, L.; Zhang, X.; Jiang, B.; Jiang, L.; Li, C.; Wang, G.; Yang, Y.; Liu, M. NMR-Based Methods for Protein Analysis. *Anal. Chem.* **2021**, *93* (4), 1866–1879. https://doi.org/10.1021/acs.analchem.0c03830.

(49) Moco, S. Studying Metabolism by NMR-Based Metabolomics. *Front. Mol. Biosci.* **2022**, *9*. https://doi.org/10.3389/fmolb.2022.882487.

(50) Peng, Y.; Zhang, Z.; He, L.; Li, C.; Liu, M. NMR Spectroscopy for Metabolomics in the Living System: Recent Progress and Future Challenges. *Anal Bioanal Chem* **2024**, *416* (9), 2319–2334. https://doi.org/10.1007/s00216-024-05137-8.

(51) Reinhold, D.; Pielke-Lombardo, H.; Jacobson, S.; Ghosh, D.; Kechris, K. Pre-Analytic Considerations for Mass Spectrometry Based Untargeted Metabolomics Data. *Methods Mol Biol* **2019**, *1978*, 323–340. https://doi.org/10.1007/978-1-4939-9236-2_20.

(52) Kostidis, S.; Addie, R. D.; Morreau, H.; Mayboroda, O. A.; Giera, M. Quantitative NMR Analysis of Intra- and Extracellular Metabolism of Mammalian Cells: A Tutorial. *Analytica Chimica Acta* **2017**, *980*, 1–24. https://doi.org/10.1016/j.aca.2017.05.011.

(53) Creek, D. J. Stable Isotope Labeled Metabolomics Improves Identification of Novel Metabolites and Pathways. *Bioanalysis* **2013**, *5* (15), 1807–1810. https://doi.org/10.4155/bio.13.131.

(54) Jang, C.; Chen, L.; Rabinowitz, J. D. Metabolomics and Isotope Tracing. *Cell* **2018**, *173* (4), 822–837. https://doi.org/10.1016/j.cell.2018.03.055.

(55) Chokkathukalam, A.; Kim, D.-H.; Barrett, M. P.; Breitling, R.; Creek, D. J. Stable Isotope-Labeling Studies in Metabolomics: New Insights into Structure and Dynamics of Metabolic Networks. *Bioanalysis* **2014**, *6* (4), 511–524. https://doi.org/10.4155/bio.13.348.

(56) Antoniewicz, M. R. A Guide to 13C Metabolic Flux Analysis for the Cancer Biologist. *Exp Mol Med* **2018**, *50* (4), 1–13. https://doi.org/10.1038/s12276-018-0060-y.

(57) Twining, C. W.; Taipale, S. J.; Ruess, L.; Bec, A.; Martin-Creuzburg, D.; Kainz, M. J. Stable Isotopes of Fatty Acids: Current and Future Perspectives for Advancing Trophic Ecology. *Philosophical Transactions of the Royal Society B: Biological Sciences* **2020**, *375* (1804), 20190641. https://doi.org/10.1098/rstb.2019.0641.

(58) Lane, A. N.; Higashi, R. M.; Fan, T. W.-M. NMR and MS-Based Stable Isotope-Resolved Metabolomics and Applications in Cancer Metabolism. *TrAC Trends in Analytical Chemistry* **2019**, *120*, 115322. https://doi.org/10.1016/j.trac.2018.11.020.

(59) Gowda, G. A. N.; Shanaiah, N.; Raftery, D. Isotope Enhanced Approaches in Metabolomics. *Adv Exp Med Biol* **2012**, *992*, 147–164. https://doi.org/10.1007/978-94-007-4954-2_8.

(60) Dayie, T. K.; Olenginski, L. T.; Taiwo, K. M. Isotope Labels Combined with Solution NMR Spectroscopy Make Visible the Invisible Conformations of Small-to-Large RNAs. *Chem. Rev.* **2022**, *122* (10), 9357–9394. https://doi.org/10.1021/acs.chemrev.1c00845.

(61) Chen, D.; Su, X.; Wang, N.; Li, Y.; Yin, H.; Li, L.; Li, L. Chemical Isotope Labeling LC-MS for Monitoring Disease Progression and Treatment in Animal Models: Plasma Metabolomics Study of Osteoarthritis Rat Model. *Sci Rep* **2017**, *7* (1), 40543. https://doi.org/10.1038/srep40543.

(62) Raman, C. V.; Krishnan, K. S. A New Type of Secondary Radiation. *Nature* **1928**, *121* (3048), 501–502. https://doi.org/10.1038/121501c0.

(63) Baena, J. R.; Lendl, B. Raman Spectroscopy in Chemical Bioanalysis. *Current Opinion in Chemical Biology* **2004**, *8* (5), 534–539. https://doi.org/10.1016/j.cbpa.2004.08.014.

(64) Prince, R. C.; Frontiera, R. R.; Potma, E. O. Stimulated Raman Scattering: From Bulk to Nano. *Chem. Rev.* **2017**, *117* (7), 5070–5094. https://doi.org/10.1021/acs.chemrev.6b00545.

(65) Gao, X.; Li, X.; Min, W. Absolute Stimulated Raman Cross Sections of Molecules. *J. Phys. Chem. Lett.* **2023**, *14* (24), 5701–5708. https://doi.org/10.1021/acs.jpclett.3c01064.

(66) Zhang, C.; Zhang, D.; Cheng, J.-X. Coherent Raman Scattering Microscopy in Biology and Medicine. *Annu Rev Biomed Eng* **2015**, *17*, 415–445. https://doi.org/10.1146/annurev-bioeng-071114-040554.

(67) Min, W.; Freudiger, C. W.; Lu, S.; Xie, X. S. Coherent Nonlinear Optical Imaging: Beyond Fluorescence Microscopy. *Annu Rev Phys Chem* **2011**, *62*, 507–530. https://doi.org/10.1146/annurev.physchem.012809.103512.

(68) Cheng, J.-X.; Xie, X. S. Vibrational Spectroscopic Imaging of Living Systems: An Emerging Platform for Biology and Medicine. *Science* **2015**, *350* (6264), aaa8870. https://doi.org/10.1126/science.aaa8870.

(69) Freudiger, C. W.; Min, W.; Saar, B. G.; Lu, S.; Holtom, G. R.; He, C.; Tsai, J. C.; Kang, J. X.; Xie, X. S. Label-Free Biomedical Imaging with High Sensitivity by Stimulated Raman Scattering Microscopy. *Science* **2008**, *322* (5909), 1857–1861. https://doi.org/10.1126/science.1165758.

(70) Saar, B. G.; Freudiger, C. W.; Reichman, J.; Stanley, C. M.; Holtom, G. R.; Xie, X. S. Video-Rate Molecular Imaging in Vivo with Stimulated Raman Scattering. *Science* **2010**, *330* (6009), 1368–1370. https://doi.org/10.1126/science.1197236.

(71) Ozeki, Y.; Kitagawa, Y.; Sumimura, K.; Nishizawa, N.; Umemura, W.; Kajiyama, S.; Fukui, K.; Itoh, K. Stimulated Raman Scattering Microscope with Shot Noise Limited Sensitivity Using Subharmonically Synchronized Laser Pulses. *Opt. Express, OE* **2010**, *18* (13), 13708–13719. https://doi.org/10.1364/OE.18.013708.

(72) Wei, L.; Yu, Y.; Shen, Y.; Wang, M. C.; Min, W. Vibrational Imaging of Newly Synthesized Proteins in Live Cells by Stimulated Raman Scattering Microscopy. *Proc Natl Acad Sci USA* **2013**, *110* (28), 11226. https://doi.org/10.1073/pnas.1303768110.

(73) Wei, L.; Shen, Y.; Xu, F.; Hu, F.; Harrington, J. K.; Targoff, K. L.; Min, W. Imaging Complex Protein Metabolism in Live Organisms by Stimulated Raman Scattering Microscopy with Isotope Labeling. *ACS Chem Biol* **2015**, *10* (3), 901–908. https://doi.org/10.1021/cb500787b.

(74) Shen, Y.; Xu, F.; Wei, L.; Hu, F.; Min, W. Live-Cell Quantitative Imaging of Proteome Degradation by Stimulated Raman Scattering. *Angewandte Chemie International Edition* **2014**, *53* (22), 5596–5599. https://doi.org/10.1002/anie.201310725.

(75) Jia, H.; Yue, S. Stimulated Raman Scattering Imaging Sheds New Light on Lipid Droplet Biology. *J. Phys. Chem. B* **2023**, *127* (11), 2381–2394. https://doi.org/10.1021/acs.jpcb.3c00038.

(76) Wang, M. C.; Min, W.; Freudiger, C. W.; Ruvkun, G.; Xie, X. S. RNAi Screening for Fat Regulatory Genes with SRS Microscopy. *Nat Methods* **2011**, *8* (2), 135–138. https://doi.org/10.1038/nmeth.1556.

(77) Dou, W.; Zhang, D.; Jung, Y.; Cheng, J.-X.; Umulis, D. M. Label-Free Imaging of Lipid-Droplet Intracellular Motion in Early *Drosophila* Embryos Using Femtosecond-Stimulated Raman Loss Microscopy. *Biophysical Journal* **2012**, *102* (7), 1666–1675. https://doi.org/10.1016/j.bpj.2012.01.057.

(78) Hong, S.; Chen, T.; Liu, L.; Cao, C.; Lv, F.; Rabinowitz, J. D.; Huang, Y.; Chen, X. Live-Cell Imaging of NADPH Production from Specific Pathways. *CCS Chemistry* **2020**, *3* (6), 1642–1648. https://doi.org/10.31635/ccschem.020.202000346.

(79) Li, X.; Li, Y.; Jiang, M.; Wu, W.; He, S.; Chen, C.; Qin, Z.; Tang, B. Z.; Mak, H. Y.; Qu, J. Y. Quantitative Imaging of Lipid Synthesis and Lipolysis Dynamics in Caenorhabditis Elegans by Stimulated Raman Scattering Microscopy. *Anal. Chem.* **2019**, *91* (3), 2279–2287. https://doi.org/10.1021/acs.analchem.8b04875.

(80) Chen, A. J.; Li, J.; Jannasch, A.; Ozseker, S.; Wang, M. C.; Cheng, J.-X. Fingerprint Stimulated Raman Scattering Imaging Reveals Retinoid Coupling Lipid Metabolism and Survival. *Chemphyschem* **2018**, *19* (19), 2500–2506. https://doi.org/10.1002/cphc.201800545.

(81) Adams, W. R.; Gautam, R.; Locke, A.; Masson, L. E.; Borrachero-Conejo, A. I.; Dollinger, B. R.; Throckmorton, G. A.; Duvall, C.; Jansen, E. D.; Mahadevan-Jansen, A. Visualizing the Lipid Dynamics Role in Infrared Neural Stimulation Using Stimulated Raman Scattering. *Biophysical Journal* **2022**, *121* (8), 1525–1540. https://doi.org/10.1016/j.bpj.2022.03.006.

(82) Fu, D.; Yu, Y.; Folick, A.; Currie, E.; Farese, R. V. Jr.; Tsai, T.-H.; Xie, X. S.; Wang, M. C. In Vivo Metabolic Fingerprinting of Neutral Lipids with Hyperspectral Stimulated Raman Scattering Microscopy. *J. Am. Chem. Soc.* **2014**, *136* (24), 8820–8828. https://doi.org/10.1021/ja504199s.

(83) Zhang, D.; Slipchenko, M. N.; Cheng, J.-X. Highly Sensitive Vibrational Imaging by Femtosecond Pulse Stimulated Raman Loss. *J. Phys. Chem. Lett.* **2011**, *2* (11), 1248–1253. https://doi.org/10.1021/jz200516n.

(84) Wang, P.; Li, J.; Wang, P.; Hu, C.-R.; Zhang, D.; Sturek, M.; Cheng, J.-X. Label-Free Quantitative Imaging of Cholesterol in Intact Tissues by Hyperspectral Stimulated Raman Scattering Microscopy. *Angewandte Chemie* **2013**, *125* (49), 13280–13284. https://doi.org/10.1002/ange.201306234.

(85) Wang, P.; Liu, B.; Zhang, D.; Belew, M. Y.; Tissenbaum, H. A.; Cheng, J.-X. Imaging Lipid Metabolism in Live Caenorhabditis Elegans Using Fingerprint Vibrations. *Angewandte Chemie* **2014**, *126* (44), 11981–11986. https://doi.org/10.1002/ange.201406029.

(86) Yue, S.; Li, J.; Lee, S.-Y.; Lee, H. J.; Shao, T.; Song, B.; Cheng, L.; Masterson, T. A.; Liu, X.; Ratliff, T. L.; Cheng, J.-X. Cholesteryl Ester Accumulation Induced by PTEN Loss and PI3K/AKT Activation Underlies Human Prostate Cancer Aggressiveness. *Cell Metabolism* **2014**, *19* (3), 393–406. https://doi.org/10.1016/j.cmet.2014.01.019.

(87) Li, J.; Cheng, J.-X. Direct Visualization of De Novo Lipogenesis in Single Living Cells. *Sci Rep* **2014**, *4* (1), 6807. https://doi.org/10.1038/srep06807.

(88) Tan, Y.; Li, J.; Zhao, G.; Huang, K.-C.; Cardenas, H.; Wang, Y.; Matei, D.; Cheng, J.-X. Metabolic Reprogramming from Glycolysis to Fatty Acid Uptake and Beta-Oxidation in Platinum-Resistant Cancer Cells. *Nat Commun* **2022**, *13* (1), 4554. https://doi.org/10.1038/s41467-022-32101-w.

(89) Tague, N.; Lin, H.; Lugagne, J.-B.; O'Connor, O. M.; Burman, D.; Wong, W. W.; Cheng, J.-X.; Dunlop, M. J. Longitudinal Single-Cell Imaging of Engineered Strains with Stimulated Raman Scattering to Characterize Heterogeneity in Fatty Acid Production. *Advanced Science* **2023**, *10* (20), 2206519. https://doi.org/10.1002/advs.202206519.

(90) Ozeki, Y.; Umemura, W.; Sumimura, K.; Nishizawa, N.; Fukui, K.; Itoh, K. Stimulated Raman Hyperspectral Imaging Based on Spectral Filtering of Broadband Fiber Laser Pulses. *Opt. Lett., OL* **2012**, *37* (3), 431–433. https://doi.org/10.1364/OL.37.000431.

(91) Zhang, D.; Wang, P.; Slipchenko, M. N.; Ben-Amotz, D.; Weiner, A. M.; Cheng, J.-X. Quantitative Vibrational Imaging by Hyperspectral Stimulated Raman Scattering Microscopy and Multivariate Curve Resolution Analysis. *Anal Chem* **2013**, *85* (1), 98–106. https://doi.org/10.1021/ac3019119.

(92) Suhalim, J. L.; Chung, C.-Y.; Lilledahl, M. B.; Lim, R. S.; Levi, M.; Tromberg, B. J.; Potma, E. O. Characterization of Cholesterol Crystals in Atherosclerotic Plaques Using Stimulated Raman Scattering and Second-Harmonic Generation Microscopy. *Biophysical Journal* **2012**, *102* (8), 1988–1995. https://doi.org/10.1016/j.bpj.2012.03.016.

(93) Freudiger, C. W.; Min, W.; Holtom, G. R.; Xu, B.; Dantus, M.; Xie, X. S. Highly Specific Label-Free Molecular Imaging with Spectrally Tailored Excitation Stimulated Raman Scattering (STE-SRS) Microscopy. *Nat Photonics* **2011**, *5* (2), 103–109. https://doi.org/10.1038/nphoton.2010.294.

(94) Fu, D.; Lu, F.-K.; Zhang, X.; Freudiger, C.; Pernik, D. R.; Holtom, G.; Xie, X. S. Quantitative Chemical Imaging with Multiplex Stimulated Raman Scattering Microscopy. *J. Am. Chem. Soc.* **2012**, *134* (8), 3623–3626. https://doi.org/10.1021/ja210081h.

(95) Fu, D.; Holtom, G.; Freudiger, C.; Zhang, X.; Xie, X. S. Hyperspectral Imaging with Stimulated Raman Scattering by Chirped Femtosecond Lasers. *J. Phys. Chem. B* **2013**, *117* (16), 4634–4640. https://doi.org/10.1021/jp308938t.

(96) Beier, H. T.; Noojin, G. D.; Rockwell, B. A. Stimulated Raman Scattering Using a Single Femtosecond Oscillator with Flexibility for Imaging and Spectral Applications. *Opt. Express, OE* **2011**, *19* (20), 18885–18892. https://doi.org/10.1364/OE.19.018885.

(97) Andresen, E. R.; Berto, P.; Rigneault, H. Stimulated Raman Scattering Microscopy by Spectral Focusing and Fiber-Generated Soliton as Stokes Pulse. *Opt. Lett., OL* **2011**, *36* (13), 2387–2389. https://doi.org/10.1364/OL.36.002387.

(98) Polli, D.; Kumar, V.; Valensise, C. M.; Marangoni, M.; Cerullo, G. Broadband Coherent Raman Scattering Microscopy. *Laser & Photonics Reviews* **2018**, *12* (9), 1800020. https://doi.org/10.1002/lpor.201800020.

(99) Hellerer, T.; Enejder, A. M. K.; Zumbusch, A. Spectral Focusing: High Spectral Resolution Spectroscopy with Broad-Bandwidth Laser Pulses. *Appl. Phys. Lett.* **2004**, *85* (1), 25–27. https://doi.org/10.1063/1.1768312.

(100) Xu, F. X.; Rathbone, E. G.; Fu, D. Simultaneous Dual-Band Hyperspectral Stimulated Raman Scattering Microscopy with Femtosecond Optical Parametric Oscillators. *J. Phys. Chem. B* **2023**, *127* (10), 2187–2197. https://doi.org/10.1021/acs.jpcb.2c09105.

(101) Das, R. S.; Agrawal, Y. K. Raman Spectroscopy: Recent Advancements, Techniques and Applications. *Vibrational Spectroscopy* **2011**, *57* (2), 163–176. https://doi.org/10.1016/j.vibspec.2011.08.003.

(102) Puppels, G. J.; de Mul, F. F. M.; Otto, C.; Greve, J.; Robert-Nicoud, M.; Arndt-Jovin, D. J.; Jovin, T. M. Studying Single Living Cells and Chromosomes by Confocal Raman Microspectroscopy. *Nature* **1990**, *347* (6290), 301–303. https://doi.org/10.1038/347301a0.

(103) Chan, J.; Fore, S.; Wachsmann-Hogiu, S.; Huser, T. Raman Spectroscopy and Microscopy of Individual Cells and Cellular Components. *Laser & Photonics Reviews* **2008**, *2* (5), 325–349. https://doi.org/10.1002/lpor.200810012.

(104) Freudiger, C. W.; Min, W.; Saar, B. G.; Lu, S.; Holtom, G. R.; He, C.; Tsai, J. C.; Kang, J. X.; Xie, X. S. Label-Free Biomedical Imaging with High Sensitivity by Stimulated Raman Scattering Microscopy. *Science* **2008**, *322* (5909), 1857–1861. https://doi.org/10.1126/science.1165758.

(105) Lu, F.-K.; Ji, M.; Fu, D.; Ni, X.; Freudiger, C. W.; Holtom, G.; Xie, X. S. Multicolor Stimulated Raman Scattering Microscopy. *Molecular Physics* **2012**, *110* (15–16), 1927–1932. https://doi.org/10.1080/00268976.2012.695028.

(106) Liao, C.-S.; Slipchenko, M. N.; Wang, P.; Li, J.; Lee, S.-Y.; Oglesbee, R. A.; Cheng, J.-X. Microsecond Scale Vibrational Spectroscopic Imaging by Multiplex Stimulated Raman Scattering Microscopy. *Light Sci Appl* **2015**, *4* (3), e265–e265. https://doi.org/10.1038/lsa.2015.38.

(107) Liao, C.-S.; Wang, P.; Wang, P.; Li, J.; Lee, H. J.; Eakins, G.; Cheng, J.-X. Spectrometer-Free Vibrational Imaging by Retrieving Stimulated Raman Signal from Highly Scattered Photons. *Science Advances* **2015**, *1* (9), e1500738. https://doi.org/10.1126/sciadv.1500738.

(108) Réhault, J.; Crisafi, F.; Kumar, V.; Ciardi, G.; Marangoni, M.; Cerullo, G.; Polli, D. Broadband Stimulated Raman Scattering with Fourier-Transform Detection. *Opt. Express, OE* **2015**, *23* (19), 25235–25246. https://doi.org/10.1364/OE.23.025235.

(109) Figueroa, B.; Fu, W.; Nguyen, T.; Shin, K.; Manifold, B.; Wise, F.; Fu, D. Broadband Hyperspectral Stimulated Raman Scattering Microscopy with a Parabolic Fiber Amplifier Source. *Biomed Opt Express* **2018**, *9* (12), 6116–6131. https://doi.org/10.1364/BOE.9.006116.

(110) Shin, K. S.; Laohajaratsang, M.; Men, S.; Figueroa, B.; Dintzis, S. M.; Fu, D. Quantitative Chemical Imaging of Breast Calcifications in Association with Neoplastic Processes. *Theranostics* **2020**, *10* (13), 5865–5878. https://doi.org/10.7150/thno.43325.

(111) Shin, K. S.; Men, S.; Wong, A.; Cobb-Bruno, C.; Chen, E. Y.; Fu, D. Quantitative Chemical Imaging of Bone Tissue for Intraoperative and Diagnostic Applications. *Anal. Chem.* **2022**, *94* (9), 3791–3799. https://doi.org/10.1021/acs.analchem.1c04354.

(112) Ni, H.; Lin, P.; Zhu, Y.; Zhang, M.; Tan, Y.; Zhan, Y.; Wang, Z.; Cheng, J.-X. Multiwindow SRS Imaging Using a Rapid Widely Tunable Fiber Laser. *Anal. Chem.* **2021**, *93* (47), 15703–15711. https://doi.org/10.1021/acs.analchem.1c03604.

(113) Heuke, S.; Sarri, B.; Audier, X.; Rigneault, H. Simultaneous Dual-Channel Stimulated Raman Scattering Microscopy Demultiplexed at Distinct Modulation Frequencies. *Opt. Lett., OL* **2018**, *43* (15), 3582–3585. https://doi.org/10.1364/OL.43.003582.

(114) Heuke, S.; Rimke, I.; Sarri, B.; Gasecka, P.; Appay, R.; Legoff, L.; Volz, P.; Büttner, E.; Rigneault, H. Shot-Noise Limited Tunable Dual-Vibrational Frequency Stimulated Raman Scattering Microscopy. *Biomed Opt Express* **2021**, *12* (12), 7780–7789. https://doi.org/10.1364/BOE.446348.

(115) Choi, Y.; Lim, S.; Shim, J. W.; Chon, B.; Lim, J. M.; Cho, M. Shot-Noise-Limited Two-Color Stimulated Raman Scattering Microscopy with a Balanced Detection Scheme. *J. Phys. Chem. B* **2020**, *124* (13), 2591–2599. https://doi.org/10.1021/acs.jpcb.0c01065.

(116) Figueroa, B.; Hu, R.; Rayner, S. G.; Zheng, Y.; Fu, D. Real-Time Microscale Temperature Imaging by Stimulated Raman Scattering. *J. Phys. Chem. Lett.* **2020**, *11* (17), 7083–7089. https://doi.org/10.1021/acs.jpclett.0c02029.

(117) Figueroa, B.; Xu, F. X.; Hu, R.; Men, S.; Fu, D. Quantitative Imaging of Intracellular Density with Ratiometric Stimulated Raman Scattering Microscopy. *J. Phys. Chem. B* **2022**, *126* (39), 7595–7603. https://doi.org/10.1021/acs.jpcb.2c04355.

(118) Alsabeeh, N.; Chausse, B.; Kakimoto, P. A.; Kowaltowski, A. J.; Shirihai, O. Cell Culture Models of Fatty Acid Overload: Problems and Solutions. *Biochimica et Biophysica Acta (BBA) - Molecular and Cell Biology of Lipids* **2018**, *1863* (2), 143–151. https://doi.org/10.1016/j.bbalip.2017.11.006.

(119) Ranneva, S. V.; Okotrub, K. A.; Amstislavsky, S. Y.; Surovtsev, N. V. Deuterated Stearic Acid Uptake and Accumulation in Lipid Droplets of Cat Oocytes. *Archives of Biochemistry and Biophysics* **2020**, *692*, 108532. https://doi.org/10.1016/j.abb.2020.108532.

(120) Stiebing, C.; Meyer, T.; Rimke, I.; Matthäus, C.; Schmitt, M.; Lorkowski, S.; Popp, J. Real-Time Raman and SRS Imaging of Living Human Macrophages Reveals Cell-to-Cell Heterogeneity and Dynamics of Lipid Uptake. *Journal of Biophotonics* **2017**, *10* (9), 1217–1226. https://doi.org/10.1002/jbio.201600279.

(121) Fu, D.; Zhou, J.; Zhu, W. S.; Manley, P. W.; Wang, Y. K.; Hood, T.; Wylie, A.; Xie, X. S. Imaging the Intracellular Distribution of Tyrosine Kinase Inhibitors in Living Cells with Quantitative Hyperspectral Stimulated Raman Scattering. *Nature Chem* **2014**, *6* (7), 614–622. https://doi.org/10.1038/nchem.1961.

(122) Sepp, K.; Lee, M.; Bluntzer, M. T. J.; Helgason, G. V.; Hulme, A. N.; Brunton, V. G. Utilizing Stimulated Raman Scattering Microscopy To Study Intracellular Distribution of Label-Free Ponatinib in Live Cells. *J. Med. Chem.* **2020**, *63* (5), 2028–2034. https://doi.org/10.1021/acs.jmedchem.9b01546.

(123) De Duve, C.; De Barsy, T.; Poole, B.; Trouet, A.; Tulkens, P.; Van Hoof, F. Lysosomotropic Agents. *Biochemical Pharmacology* **1974**, *23* (18), 2495–2531. https://doi.org/10.1016/0006-2952(74)90174-9.

(124) Rinia, H. A.; Burger, K. N. J.; Bonn, M.; Müller, M. Quantitative Label-Free Imaging of Lipid Composition and Packing of Individual Cellular Lipid Droplets Using Multiplex CARS Microscopy. *Biophysical Journal* **2008**, *95* (10), 4908–4914. https://doi.org/10.1529/biophysj.108.137737.

(125) Corcoran, M. P.; Lamon-Fava, S.; Fielding, R. A. Skeletal Muscle Lipid Deposition and Insulin Resistance: Effect of Dietary Fatty Acids and Exercise. *The American Journal of Clinical Nutrition* **2007**, *85* (3), 662–677. https://doi.org/10.1093/ajcn/85.3.662.

(126) Marshall, J. A.; Bessesen, D. H.; Hamman, R. F. High Saturated Fat and Low Starch and Fibre Are Associated with Hyperinsulinaemia in a Non-Diabetic Population: The San Luis Valley Diabetes Study. *Diabetologia* **1997**, *40* (4), 430–438. https://doi.org/10.1007/s001250050697.

(127) Soriguer, F.; Esteva, I.; Rojo-Martinez, G.; Adana, M. R. de; Dobarganes, M. C.; Garcia-Almeida, J. M.; Tinahones, F.; Beltran, M.; Gonzalez-Romero, S.; Olveira, G.; Gomez-Zumaquero, J. M. Oleic Acid from Cooking Oils Is Associated with Lower Insulin

Resistance in the General Population (Pizarra Study). *European Journal of Endocrinology* **2004**, *150* (1), 33.

(128) Yu, Y.; Ramachandran, P. V.; Wang, M. C. Shedding New Light on Lipid Functions with CARS and SRS Microscopy. *Biochim Biophys Acta* **2014**, *1841* (8), 1120–1129. https://doi.org/10.1016/j.bbalip.2014.02.003.

(129) Heinrich, C.; Hofer, A.; Ritsch, A.; Ciardi, C.; Bernet, S.; Ritsch-Marte, M. Selective Imaging of Saturated and Unsaturated Lipids by Wide-Field CARS-Microscopy. *Opt. Express, OE* **2008**, *16* (4), 2699–2708. https://doi.org/10.1364/OE.16.002699.

(130) Samek, O.; Jonáš, A.; Pilát, Z.; Zemánek, P.; Nedbal, L.; Tříska, J.; Kotas, P.; Trtílek, M. Raman Microspectroscopy of Individual Algal Cells: Sensing Unsaturation of Storage Lipids in Vivo. *Sensors* **2010**, *10* (9), 8635–8651. https://doi.org/10.3390/s100908635.

(131) Wu, H.; Volponi, J. V.; Oliver, A. E.; Parikh, A. N.; Simmons, B. A.; Singh, S. In Vivo Lipidomics Using Single-Cell Raman Spectroscopy. *Proceedings of the National Academy of Sciences* **2011**, *108* (9), 3809–3814. https://doi.org/10.1073/pnas.1009043108.

(132) Hosokawa, M.; Ando, M.; Mukai, S.; Osada, K.; Yoshino, T.; Hamaguchi, H.; Tanaka, T. In Vivo Live Cell Imaging for the Quantitative Monitoring of Lipids by Using Raman Microspectroscopy. *Anal. Chem.* **2014**, *86* (16), 8224–8230. https://doi.org/10.1021/ac501591d.

(133) Czamara, K.; Majzner, K.; Selmi, A.; Baranska, M.; Ozaki, Y.; Kaczor, A. Unsaturated Lipid Bodies as a Hallmark of Inflammation Studied by Raman 2D and 3D Microscopy. *Sci Rep* **2017**, *7* (1), 40889. https://doi.org/10.1038/srep40889.

(134) Daemen, S.; Gemmink, A.; Paul, A.; Billecke, N.; Rieger, K.; Parekh, S. H.; Hesselink, M. K. C. Label-Free CARS Microscopy Reveals Similar Triacylglycerol Acyl Chain Length and Saturation in Myocellular Lipid Droplets of Athletes and Individuals with Type 2 Diabetes. *Diabetologia* **2020**, *63* (12), 2654–2664. https://doi.org/10.1007/s00125-020-05266-6.

(135) Haka, A. S.; Shafer-Peltier, K. E.; Fitzmaurice, M.; Crowe, J.; Dasari, R. R.; Feld, M. S. Diagnosing Breast Cancer by Using Raman Spectroscopy. *Proceedings of the National Academy of Sciences* **2005**, *102* (35), 12371–12376. https://doi.org/10.1073/pnas.0501390102.

(136) Ichimura, T.; Chiu, L.; Fujita, K.; Kawata, S.; Watanabe, T. M.; Yanagida, T.; Fujita, H. Visualizing Cell State Transition Using Raman Spectroscopy. *PLoS One* **2014**, *9* (1), e84478. https://doi.org/10.1371/journal.pone.0084478.

(137) Ichimura, T.; Chiu, L.; Fujita, K.; Machiyama, H.; Yamaguchi, T.; Watanabe, T.; Fujita, H. Non-Label Immune Cell State Prediction Using Raman Spectroscopy. *Scientific Reports* **2016**, *6*, 37562. https://doi.org/10.1038/srep37562.

(138) Dellepiane, G.; Overend, J. Vibrational Spectra and Assignment of Acetone, Aαα Acetone-D3 and Acetone-D6. *Spectrochimica Acta* **1966**, *22* (4), 593–614. https://doi.org/10.1016/0371-1951(66)80091-7.

(139) Wilmshurst, J. K.; Bernstein, H. J. THE INFRARED AND RAMAN SPECTRA OF TOLUENE, TOLUENE-α-D3, m-XYLENE, AND m-XYLENE-Aα′-D6. *Can. J. Chem.* **1957**, *35* (8), 911–925. https://doi.org/10.1139/v57-123.

(140) Manifold, B.; Fu, D. Quantitative Stimulated Raman Scattering Microscopy: Promises and Pitfalls. *Annual Review of Analytical Chemistry* **2022**, *15* (1), 269–289. https://doi.org/10.1146/annurev-anchem-061020-015110.

(141) Oh, S.; Lee, C.; Yang, W.; Li, A.; Mukherjee, A.; Basan, M.; Ran, C.; Yin, W.; Tabin, C. J.; Fu, D.; Xie, X. S.; Kirschner, M. W. Protein and Lipid Mass Concentration Measurement in Tissues by Stimulated Raman Scattering Microscopy. *Proceedings of the National Academy of Sciences* **2022**, *119* (17), e2117938119. https://doi.org/10.1073/pnas.2117938119.

(142) Manifold, B.; Thomas, E.; Francis, A. T.; Hill, A. H.; Fu, D. Denoising of Stimulated Raman Scattering Microscopy Images via Deep Learning. *Biomed Opt Express* **2019**, *10* (8), 3860–3874. https://doi.org/10.1364/BOE.10.003860.

(143) Zhang, J.; Zhao, J.; Lin, H.; Tan, Y.; Cheng, J.-X. High-Speed Chemical Imaging by Dense-Net Learning of Femtosecond Stimulated Raman Scattering. *J. Phys. Chem. Lett.* **2020**, *11* (20), 8573–8578. https://doi.org/10.1021/acs.jpclett.0c01598.

(144) Manifold, B.; Men, S.; Hu, R.; Fu, D. A Versatile Deep Learning Architecture for Classification and Label-Free Prediction of Hyperspectral Images. *Nat Mach Intell* **2021**, *3*, 306–315. https://doi.org/10.1038/s42256-021-00309-y.

(145) Liu, Z.; Su, W.; Ao, J.; Wang, M.; Jiang, Q.; He, J.; Gao, H.; Lei, S.; Nie, J.; Yan, X.; Guo, X.; Zhou, P.; Hu, H.; Ji, M. Instant Diagnosis of Gastroscopic Biopsy via Deep-Learned Single-Shot Femtosecond Stimulated Raman Histology. *Nat Commun* **2022**, *13* (1), 4050. https://doi.org/10.1038/s41467-022-31339-8.

(146) Xu, F. X.; Wu, R.; Hu, K.; Fu, D. Measuring Drug Response with Single-Cell Growth Rate Quantification. *Anal. Chem.* **2023**, *95* (49), 18114–18121. https://doi.org/10.1021/acs.analchem.3c03434.

(147) Trédan, O.; Galmarini, C. M.; Patel, K.; Tannock, I. F. Drug Resistance and the Solid Tumor Microenvironment. *JNCI: Journal of the National Cancer Institute* **2007**, *99* (19), 1441–1454. https://doi.org/10.1093/jnci/djm135.

(148) Spencer, S. L.; Gaudet, S.; Albeck, J. G.; Burke, J. M.; Sorger, P. K. Non-Genetic Origins of Cell-to-Cell Variability in TRAIL-Induced Apoptosis. *Nature* **2009**, *459* (7245), 428–432. https://doi.org/10.1038/nature08012.

(149) Albeck, J.; Burke, J.; Aldridge, B.; Zhang, M.; Lauffenburger, D.; Sorger, P. Quantitative Analysis of Pathways Controlling Extrinsic Apoptosis in Single Cells. *Mol Cell* **2008**, *30* (1), 11–25. https://doi.org/10.1016/j.molcel.2008.02.012.

(150) Saunders, N. A.; Simpson, F.; Thompson, E. W.; Hill, M. M.; Endo-Munoz, L.; Leggatt, G.; Minchin, R. F.; Guminski, A. Role of Intratumoural Heterogeneity in Cancer Drug Resistance: Molecular and Clinical Perspectives. *EMBO Molecular Medicine* **2012**, *4* (8), 675–684. https://doi.org/10.1002/emmm.201101131.

(151) Sun, X.; Yu, Q. Intra-Tumor Heterogeneity of Cancer Cells and Its Implications for Cancer Treatment. *Acta Pharmacol Sin* **2015**, *36* (10), 1219–1227. https://doi.org/10.1038/aps.2015.92.

(152) Mansoori, B.; Mohammadi, A.; Davudian, S.; Shirjang, S.; Baradaran, B. The Different Mechanisms of Cancer Drug Resistance: A Brief Review. *Adv Pharm Bull* **2017**, *7* (3), 339–348. https://doi.org/10.15171/apb.2017.041.

(153) Wang, X.; Zhang, H.; Chen, X. Drug Resistance and Combating Drug Resistance in Cancer. *Cancer Drug Resistance* **2019**, *2* (2), 141–160. https://doi.org/10.20517/cdr.2019.10.

(154) Batlle, E.; Clevers, H. Cancer Stem Cells Revisited. *Nat Med* **2017**, *23* (10), 1124–1134. https://doi.org/10.1038/nm.4409.

(155) Patel, A. P.; Tirosh, I.; Trombetta, J. J.; Shalek, A. K.; Gillespie, S. M.; Wakimoto, H.; Cahill, D. P.; Nahed, B. V.; Curry, W. T.; Martuza, R. L.; Louis, D. N.; Rozenblatt-Rosen, O.; Suvà, M. L.; Regev, A.; Bernstein, B. E. Single-Cell RNA-Seq Highlights Intratumoral Heterogeneity in Primary Glioblastoma. *Science* **2014**, *344* (6190), 1396–1401. https://doi.org/10.1126/science.1254257.

(156) Hafner, M.; Niepel, M.; Chung, M.; Sorger, P. K. Growth Rate Inhibition Metrics Correct for Confounders in Measuring Sensitivity to Cancer Drugs. *Nat Methods* **2016**, *13* (6), 521–527. https://doi.org/10.1038/nmeth.3853.

(157) Schwartz, H. R.; Richards, R.; Fontana, R. E.; Joyce, A. J.; Honeywell, M. E.; Lee, M. J. Drug GRADE: An Integrated Analysis of Population Growth and Cell Death Reveals Drug-Specific and Cancer Subtype-Specific Response Profiles. *Cell Rep* **2020**, *31* (12), 107800. https://doi.org/10.1016/j.celrep.2020.107800.

(158) Lukačišin, M.; Espinosa-Cantú, A.; Bollenbach, T. Intron-Mediated Induction of Phenotypic Heterogeneity. *Nature* **2022**, *605* (7908), 113–118. https://doi.org/10.1038/s41586-022-04633-0.

(159) Granada, A. E.; Jiménez, A.; Stewart-Ornstein, J.; Blüthgen, N.; Reber, S.; Jambhekar, A.; Lahav, G. The Effects of Proliferation Status and Cell Cycle Phase on the Responses of Single Cells to Chemotherapy. *Mol Biol Cell* **2020**, *31* (8), 845–857. https://doi.org/10.1091/mbc.E19-09-0515.

(160) Jing, W.; Camellato, B.; Roney, I. J.; Kaern, M.; Godin, M. Measuring Single-Cell Phenotypic Growth Heterogeneity Using a Microfluidic Cell Volume Sensor. *Sci Rep* **2018**, *8*, 17809. https://doi.org/10.1038/s41598-018-36000-3.

(161) Leal-Esteban, L. C.; Fajas, L. Cell Cycle Regulators in Cancer Cell Metabolism. *Biochimica et Biophysica Acta (BBA) - Molecular Basis of Disease* **2020**, *1866* (5), 165715. https://doi.org/10.1016/j.bbadis.2020.165715.

(162) Costello, J. C.; Heiser, L. M.; Georgii, E.; Gönen, M.; Menden, M. P.; Wang, N. J.; Bansal, M.; Ammad-ud-din, M.; Hintsanen, P.; Khan, S. A.; Mpindi, J.-P.; Kallioniemi, O.; Honkela, A.; Aittokallio, T.; Wennerberg, K.; Collins, J. J.; Gallahan, D.; Singer, D.; Saez-Rodriguez, J.; Kaski, S.; Gray, J. W.; Stolovitzky, G. A Community Effort to Assess and Improve Drug Sensitivity Prediction Algorithms. *Nat Biotechnol* **2014**, *32* (12), 1202–1212. https://doi.org/10.1038/nbt.2877.

(163) Almendro, V.; Marusyk, A.; Polyak, K. Cellular Heterogeneity and Molecular Evolution in Cancer. *Annual Review of Pathology: Mechanisms of Disease* **2013**, *8* (1), 277–302. https://doi.org/10.1146/annurev-pathol-020712-163923.

(164) Popescu, G.; Park, K.; Mir, M.; Bashir, R. New Technologies for Measuring Single Cell Mass. *Lab Chip* **2014**, *14* (4), 646–652. https://doi.org/10.1039/C3LC51033F.

(165) Zangle, T. A.; Teitell, M. A. Live-Cell Mass Profiling: An Emerging Approach in Quantitative Biophysics. *Nat Methods* **2014**, *11* (12), 1221–1228. https://doi.org/10.1038/nmeth.3175.

(166) Godin, M.; Delgado, F. F.; Son, S.; Grover, W. H.; Bryan, A. K.; Tzur, A.; Jorgensen, P.; Payer, K.; Grossman, A. D.; Kirschner, M. W.; Manalis, S. R. Using Buoyant Mass to Measure the Growth of Single Cells. *Nat Methods* **2010**, *7* (5), 387–390. https://doi.org/10.1038/nmeth.1452.

(167) Bryan, A. K.; Hecht, V. C.; Shen, W.; Payer, K.; Grover, W. H.; Manalis, S. R. Measuring Single Cell Mass, Volume, and Density with Dual Suspended Microchannel Resonators. *Lab Chip* **2014**, *14* (3), 569–576. https://doi.org/10.1039/c3lc51022k.

(168) Cermak, N.; Olcum, S.; Delgado, F. F.; Wasserman, S. C.; Payer, K. R.; A Murakami, M.; Knudsen, S. M.; Kimmerling, R. J.; Stevens, M. M.; Kikuchi, Y.; Sandikci, A.; Ogawa, M.; Agache, V.; Baléras, F.; Weinstock, D. M.; Manalis, S. R. High-Throughput Measurement of Single-Cell Growth Rates Using Serial Microfluidic Mass Sensor Arrays. *Nature Biotechnology* **2016**, *34* (10), 1052–1059. https://doi.org/10.1038/nbt.3666.

(169) Lee, K.; Kim, K.; Jung, J.; Heo, J.; Cho, S.; Lee, S.; Chang, G.; Jo, Y.; Park, H.; Park, Y. Quantitative Phase Imaging Techniques for the Study of Cell Pathophysiology: From Principles to Applications. *Sensors (Basel)* **2013**, *13* (4), 4170–4191. https://doi.org/10.3390/s130404170.

(170) Sherazade Aknoun; Julien Savatier; Pierre Bon; Frédéric Galland; Lamiae Abdeladim; Benoit F. Wattellier; Serge Monneret. Living Cell Dry Mass Measurement Using Quantitative Phase Imaging with Quadriwave Lateral Shearing Interferometry: An Accuracy and Sensitivity Discussion. *Journal of Biomedical Optics* **2015**, *20* (12), 1–15. https://doi.org/10.1117/1.JBO.20.12.126009.

(171) Miao, K.; Wei, L. Live-Cell Imaging and Quantification of PolyQ Aggregates by Stimulated Raman Scattering of Selective Deuterium Labeling. *ACS Cent. Sci.* **2020**, *6* (4), 478–486. https://doi.org/10.1021/acscentsci.9b01196.

(172) Spratt, S. J.; Oguchi, K.; Miura, K.; Asanuma, M.; Kosakamoto, H.; Obata, F.; Ozeki, Y. Probing Methionine Uptake in Live Cells by Deuterium Labeling and Stimulated Raman Scattering. *J. Phys. Chem. B* **2022**, *126* (8), 1633–1639. https://doi.org/10.1021/acs.jpcb.1c08343.

(173) Spratt, S. J.; Mizuguchi, T.; Akaboshi, H.; Kosakamoto, H.; Okada, R.; Obata, F.; Ozeki, Y. Imaging the Uptake of Deuterated Methionine in Drosophila with Stimulated Raman Scattering. *Frontiers in Chemistry* **2023**, *11*.

(174) Zhang, M.; Hong, W.; Abutaleb, N. S.; Li, J.; Dong, P.-T.; Zong, C.; Wang, P.; Seleem, M. N.; Cheng, J.-X. Rapid Determination of Antimicrobial Susceptibility by Stimulated Raman Scattering Imaging of D2O Metabolic Incorporation in a Single Bacterium. *Advanced Science* **2020**, *7* (19), 2001452. https://doi.org/10.1002/advs.202001452.

(175) Zhang, M.; Seleem, M. N.; Cheng, J.-X. Rapid Antimicrobial Susceptibility Testing by Stimulated Raman Scattering Imaging of Deuterium Incorporation in a Single Bacterium. *J Vis Exp* **2022**, No. 180, 10.3791/62398. https://doi.org/10.3791/62398.

(176) Sun, B.; Wang, Z.; Lin, J.; Chen, C.; Zheng, G.; Yue, S.; Wang, H.; Kang, X.; Chen, X.; Hong, W.; Wang, P. Automatic Quantitative Analysis of Metabolism Inactivation Concentration in Single Bacterium Using Stimulated Raman Scattering Microscopy with Deep Learning Image Segmentation. *Medicine in Novel Technology and Devices* **2022**, *14*, 100114. https://doi.org/10.1016/j.medntd.2022.100114.

(177) Ge, X.; Pereira, F. C.; Mitteregger, M.; Berry, D.; Zhang, M.; Hausmann, B.; Zhang, J.; Schintlmeister, A.; Wagner, M.; Cheng, J.-X. SRS-FISH: A High-Throughput Platform Linking Microbiome Metabolism to Identity at the Single-Cell Level. *Proceedings of the National Academy of Sciences* **2022**, *119* (26), e2203519119. https://doi.org/10.1073/pnas.2203519119.

(178) Zhang, W.; Sun, H.; He, S.; Chen, X.; Yao, L.; Zhou, L.; Wang, Y.; Wang, P.; Hong, W. Compound Raman Microscopy for Rapid Diagnosis and Antimicrobial Susceptibility Testing of Pathogenic Bacteria in Urine. *Frontiers in Microbiology* **2022**, *13*.

(179) Okayasu, T.; Ikeda, M.; Akimoto, K.; Sorimachi, K. The Amino Acid Composition of Mammalian and Bacterial Cells. *Amino Acids* **1997**, *13* (3), 379–391. https://doi.org/10.1007/BF01372601.

(180) Hill, A. H.; Munger, E.; Francis, A. T.; Manifold, B.; Fu, D. Frequency Modulation Stimulated Raman Scattering Microscopy through Polarization Encoding. *J. Phys. Chem. B* **2019**, *123* (40), 8397–8404. https://doi.org/10.1021/acs.jpcb.9b07075.

(181) Jiang, J.; Greulich, H.; Jänne, P. A.; Sellers, W. R.; Meyerson, M.; Griffin, J. D. Epidermal Growth Factor–Independent Transformation of Ba/F3 Cells with Cancer-Derived Epidermal Growth Factor Receptor Mutants Induces Gefitinib-Sensitive Cell Cycle Progression. *Cancer Research* **2005**, *65* (19), 8968–8974. https://doi.org/10.1158/0008-5472.CAN-05-1829.

(182) Araki, T.; Yashima, H.; Shimizu, K.; Aomori, T.; Hashita, T.; Kaira, K.; Nakamura, T.; Yamamoto, K. Review of the Treatment of Non-Small Cell Lung Cancer with Gefitinib. *Clin Med Insights Oncol* **2012**, *6*, 407–421. https://doi.org/10.4137/CMO.S7340.

(183) Dey, P. Cancer Nucleus: Morphology and Beyond. *Diagnostic Cytopathology* **2010**, *38* (5), 382–390. https://doi.org/10.1002/dc.21234.

(184) Hasan, M. R.; Hassan, N.; Khan, R.; Kim, Y.-T.; Iqbal, S. M. Classification of Cancer Cells Using Computational Analysis of Dynamic Morphology. *Computer Methods and Programs in Biomedicine* **2018**, *156*, 105–112. https://doi.org/10.1016/j.cmpb.2017.12.003.

(185) Li, Y.; Nowak, C. M.; Pham, U.; Nguyen, K.; Bleris, L. Cell Morphology-Based Machine Learning Models for Human Cell State Classification. *npj Syst Biol Appl* **2021**, *7* (1), 1–9. https://doi.org/10.1038/s41540-021-00180-y.

(186) Dai, X.; Cheng, H.; Bai, Z.; Li, J. Breast Cancer Cell Line Classification and Its Relevance with Breast Tumor Subtyping. *J Cancer* **2017**, *8* (16), 3131–3141. https://doi.org/10.7150/jca.18457.

(187) Hoque, M.; Abbassi, R. H.; Froio, D.; Man, J.; Johns, T. G.; Stringer, B. W.; Day, B. W.; Pajic, M.; Kassiou, M.; Munoz, L. Changes in Cell Morphology Guide Identification of Tubulin as the Off-Target for Protein Kinase Inhibitors. *Pharmacological Research* **2018**, *134*, 166–178. https://doi.org/10.1016/j.phrs.2018.06.023.

(188) Ghelli, A.; Giovanni, M.; Simonetti, G. The Balance between Mitotic Death and Mitotic Slippage in Acute Leukemia: A New Therapeutic Window? *Journal of Hematology & Oncology* **2019**, *12*. https://doi.org/10.1186/s13045-019-0808-4.

(189) Bischoff, R.; Holtzer, H. THE EFFECT OF MITOTIC INHIBITORS ON MYOGENESIS IN VITRO. *Journal of Cell Biology* **1968**, *36* (1), 111–127. https://doi.org/10.1083/jcb.36.1.111.

(190) Vakifahmetoglu, H.; Olsson, M.; Zhivotovsky, B. Death through a Tragedy: Mitotic Catastrophe. *Cell Death Differ* **2008**, *15* (7), 1153–1162. https://doi.org/10.1038/cdd.2008.47.

(191) Sleiman, R. J.; Catchpoole, D. R.; Stewart, B. W. Drug-Induced Death of Leukaemic Cells after G2/M Arrest: Higher Order DNA Fragmentation as an Indicator of Mechanism. *Br J Cancer* **1998**, *77* (1), 40–50. https://doi.org/10.1038/bjc.1998.7.

(192) Montecucco, A.; Zanetta, F.; Biamonti, G. Molecular Mechanisms of Etoposide. *EXCLI J* **2015**, *14*, 95–108. https://doi.org/10.17179/excli2015-561.

(193) Griffith, L. G.; Swartz, M. A. Capturing Complex 3D Tissue Physiology in Vitro. *Nat Rev Mol Cell Biol* **2006**, *7* (3), 211–224. https://doi.org/10.1038/nrm1858.

(194) Abbott, A. Cell Culture: Biology's New Dimension. *Nature* **2003**, *424* (6951), 870–873. https://doi.org/10.1038/424870a.

(195) Ravi, M.; Paramesh, V.; Kaviya, S. r.; Anuradha, E.; Solomon, F. D. P. 3D Cell Culture Systems: Advantages and Applications. *Journal of Cellular Physiology* **2015**, *230* (1), 16–26. https://doi.org/10.1002/jcp.24683.

(196) Edmondson, R.; Broglie, J. J.; Adcock, A. F.; Yang, L. Three-Dimensional Cell Culture Systems and Their Applications in Drug Discovery and Cell-Based Biosensors. *Assay Drug Dev Technol* **2014**, *12* (4), 207–218. https://doi.org/10.1089/adt.2014.573.

(197) Lv, D.; Hu, Z.; Lu, L.; Lu, H.; Xu, X. Three-dimensional Cell Culture: A Powerful Tool in Tumor Research and Drug Discovery (Review). *Oncology Letters* **2017**, *14* (6), 6999–7010. https://doi.org/10.3892/ol.2017.7134.

(198) Langhans, S. A. Three-Dimensional in Vitro Cell Culture Models in Drug Discovery and Drug Repositioning. *Frontiers in Pharmacology* **2018**, *9*.

(199) Hill, A. H.; Manifold, B.; Fu, D. Tissue Imaging Depth Limit of Stimulated Raman Scattering Microscopy. *Biomed. Opt. Express, BOE* **2020**, *11* (2), 762–774. https://doi.org/10.1364/BOE.382396.

(200) Chitcholtan, K.; Asselin, E.; Parent, S.; Sykes, P. H.; Evans, J. J. Differences in Growth Properties of Endometrial Cancer in Three Dimensional (3D) Culture and 2D Cell Monolayer. *Experimental Cell Research* **2013**, *319* (1), 75–87. https://doi.org/10.1016/j.yexcr.2012.09.012.

(201) Duval, K.; Grover, H.; Han, L.-H.; Mou, Y.; Pegoraro, A. F.; Fredberg, J.; Chen, Z. Modeling Physiological Events in 2D vs. 3D Cell Culture. *Physiology* **2017**, *32* (4), 266–277. https://doi.org/10.1152/physiol.00036.2016.

(202) Breslin, S.; O'Driscoll, L. The Relevance of Using 3D Cell Cultures, in Addition to 2D Monolayer Cultures, When Evaluating Breast Cancer Drug Sensitivity and Resistance. *Oncotarget* **2016**, *7* (29), 45745–45756. https://doi.org/10.18632/oncotarget.9935.

(203) Riedl, A.; Schlederer, M.; Pudelko, K.; Stadler, M.; Walter, S.; Unterleuthner, D.; Unger, C.; Kramer, N.; Hengstschläger, M.; Kenner, L.; Pfeiffer, D.; Krupitza, G.; Dolznig, H. Comparison of Cancer Cells in 2D vs 3D Culture Reveals Differences in AKT–mTOR–S6K Signaling and Drug Responses. *Journal of Cell Science* **2017**, *130* (1), 203–218. https://doi.org/10.1242/jcs.188102.

(204) Melissaridou, S.; Wiechec, E.; Magan, M.; Jain, M. V.; Chung, M. K.; Farnebo, L.; Roberg, K. The Effect of 2D and 3D Cell Cultures on Treatment Response, EMT Profile and Stem Cell Features in Head and Neck Cancer. *Cancer Cell International* **2019**, *19* (1), 16. https://doi.org/10.1186/s12935-019-0733-1.

(205) Zlatska, A. V.; Vasyliev, R. G.; Gordiienko, I. M.; Rodnichenko, A. E.; Morozova, M. A.; Vulf, M. A.; Zubov, D. O.; Novikova, S. N.; Litvinova, L. S.; Grebennikova, T. V.; Zlatskiy, I. A.; Syroeshkin, A. V. Effect of the Deuterium on Efficiency and Type of Adipogenic Differentiation of Human Adipose-Derived Stem Cells in Vitro. *Sci Rep* **2020**, *10* (1), 5217. https://doi.org/10.1038/s41598-020-61983-3.

(206) Goers, L.; Freemont, P.; Polizzi, K. M. Co-Culture Systems and Technologies: Taking Synthetic Biology to the next Level. *J R Soc Interface* **2014**, *11* (96), 20140065. https://doi.org/10.1098/rsif.2014.0065.

(207) Fischer, C. L.; Bates, A. M.; Lanzel, E. A.; Guthmiller, J. M.; Johnson, G. K.; Singh, N. K.; Kumar, A.; Vidva, R.; Abbasi, T.; Vali, S.; Xie, X. J.; Zeng, E.; Brogden, K. A.

Computational Models Accurately Predict Multi-Cell Biomarker Profiles in Inflammation and Cancer. *Sci Rep* **2019**, *9* (1), 10877. https://doi.org/10.1038/s41598-019-47381-4.

(208) Wei, M.; Shi, L.; Shen, Y.; Zhao, Z.; Guzman, A.; Kaufman, L. J.; Wei, L.; Min, W. Volumetric Chemical Imaging by Clearing-Enhanced Stimulated Raman Scattering Microscopy. *Proceedings of the National Academy of Sciences* **2019**, *116* (14), 6608–6617. https://doi.org/10.1073/pnas.1813044116.

(209) Xu, F. X.; Sun, R.; Owens, R.; Hu, K.; Fu, D. Assessing Drug Uptake and Response Differences in 2D and 3D Cellular Environments Using Stimulated Raman Scattering Microscopy. *Anal. Chem.* **2024**, *96* (36), 14480–14489. https://doi.org/10.1021/acs.analchem.4c02592.

(210) Kapałczyńska, M.; Kolenda, T.; Przybyła, W.; Zajączkowska, M.; Teresiak, A.; Filas, V.; Ibbs, M.; Bliźniak, R.; Łuczewski, Ł.; Lamperska, K. 2D and 3D Cell Cultures – a Comparison of Different Types of Cancer Cell Cultures. *Arch Med Sci* **2018**, *14* (4), 910–919. https://doi.org/10.5114/aoms.2016.63743.

(211) Kim, J. B. Three-Dimensional Tissue Culture Models in Cancer Biology. *Seminars in Cancer Biology* **2005**, *15* (5), 365–377. https://doi.org/10.1016/j.semcancer.2005.05.002.

(212) Ghosh, S.; Spagnoli, G. C.; Martin, I.; Ploegert, S.; Demougin, P.; Heberer, M.; Reschner, A. Three-Dimensional Culture of Melanoma Cells Profoundly Affects Gene Expression Profile: A High Density Oligonucleotide Array Study. *Journal of Cellular Physiology* **2005**, *204* (2), 522–531. https://doi.org/10.1002/jcp.20320.

(213) Chignola, R.; Schenetti, A.; Andrighetto, G.; Chiesa, E.; Foroni, R.; Sartoris, S.; Tridente, G.; Liberati, D. Forecasting the Growth of Multicell Tumour Spheroids: Implications for the Dynamic Growth of Solid Tumours. *Cell Proliferation* **2000**, *33* (4), 219–229. https://doi.org/10.1046/j.1365-2184.2000.00174.x.

(214) Tang, J.; Shi, J.; Liu, J. Editorial: Advances in 3D Cell Culture for Drug Screening and Toxicology Evaluation. *Front Bioeng Biotechnol* **2023**, *11*, 1266506. https://doi.org/10.3389/fbioe.2023.1266506.

(215) Baker, B. M.; Chen, C. S. Deconstructing the Third Dimension – How 3D Culture Microenvironments Alter Cellular Cues. *J Cell Sci* **2012**, *125* (13), 3015–3024. https://doi.org/10.1242/jcs.079509.

(216) Weiswald, L.-B.; Bellet, D.; Dangles-Marie, V. Spherical Cancer Models in Tumor Biology. *Neoplasia* **2015**, *17* (1), 1–15. https://doi.org/10.1016/j.neo.2014.12.004.

(217) Primeau, A. J.; Rendon, A.; Hedley, D.; Lilge, L.; Tannock, I. F. The Distribution of the Anticancer Drug Doxorubicin in Relation to Blood Vessels in Solid Tumors. *Clinical Cancer Research* **2005**, *11* (24), 8782–8788. https://doi.org/10.1158/1078-0432.CCR-05-1664.

(218) Ardakani, A. G.; Cheema, U.; Brown, R. A.; Shipley, R. J. Quantifying the Correlation between Spatially Defined Oxygen Gradients and Cell Fate in an Engineered Three-Dimensional Culture Model. *Journal of The Royal Society Interface* **2014**, *11* (98), 20140501. https://doi.org/10.1098/rsif.2014.0501.

(219) Moran-Alvarez, A.; Gonzalez-Menendez, P.; Mayo, J. C.; Sainz, R. M. Reflections on the Biology of Cell Culture Models: Living on the Edge of Oxidative Metabolism in Cancer Cells. *International Journal of Molecular Sciences* **2023**, *24* (3), 2717. https://doi.org/10.3390/ijms24032717.

(220) Junttila, M. R.; de Sauvage, F. J. Influence of Tumour Micro-Environment Heterogeneity on Therapeutic Response. *Nature* **2013**, *501* (7467), 346–354. https://doi.org/10.1038/nature12626.

(221) Thoma, C. R.; Zimmermann, M.; Agarkova, I.; Kelm, J. M.; Krek, W. 3D Cell Culture Systems Modeling Tumor Growth Determinants in Cancer Target Discovery. *Advanced Drug Delivery Reviews* **2014**, *69–70*, 29–41. https://doi.org/10.1016/j.addr.2014.03.001.

(222) Nunes, A. S.; Barros, A. S.; Costa, E. C.; Moreira, A. F.; Correia, I. J. 3D Tumor Spheroids as in Vitro Models to Mimic in Vivo Human Solid Tumors Resistance to Therapeutic Drugs. *Biotechnology and Bioengineering* **2019**, *116* (1), 206–226. https://doi.org/10.1002/bit.26845.

(223) Fisher, M. F.; Rao, S. S. Three-Dimensional Culture Models to Study Drug Resistance in Breast Cancer. *Biotechnology and Bioengineering* **2020**, *117* (7), 2262–2278. https://doi.org/10.1002/bit.27356.

(224) Aissa, A. F.; Islam, A. B. M. M. K.; Ariss, M. M.; Go, C. C.; Rader, A. E.; Conrardy, R. D.; Gajda, A. M.; Rubio-Perez, C.; Valyi-Nagy, K.; Pasquinelli, M.; Feldman, L. E.; Green, S. J.; Lopez-Bigas, N.; Frolov, M. V.; Benevolenskaya, E. V. Single-Cell Transcriptional Changes Associated with Drug Tolerance and Response to Combination Therapies in Cancer. *Nature Communications* **2021**, *12* (1), 1628. https://doi.org/10.1038/s41467-021-21884-z.

(225) Wang, F.; Weaver, V. M.; Petersen, O. W.; Larabell, C. A.; Dedhar, S.; Briand, P.; Lupu, R.; Bissell, M. J. Reciprocal Interactions between Β1-Integrin and Epidermal Growth Factor Receptor in Three-Dimensional Basement Membrane Breast Cultures: A Different Perspective in Epithelial Biology. *Proceedings of the National Academy of Sciences* **1998**, *95* (25), 14821–14826. https://doi.org/10.1073/pnas.95.25.14821.

(226) Nowacka, M.; Sterzynska, K.; Andrzejewska, M.; Nowicki, M.; Januchowski, R. Drug Resistance Evaluation in Novel 3D in Vitro Model. *Biomedicine & Pharmacotherapy* **2021**, *138*, 111536. https://doi.org/10.1016/j.biopha.2021.111536.

(227) Dittmer, A.; Fuchs, A.; Oerlecke, I.; Leyh, B.; Kaiser, S.; Martens, J. W. M.; Lützkendorf, J.; Müller, L.; Dittmer, J. Mesenchymal Stem Cells and Carcinoma-Associated Fibroblasts Sensitize Breast Cancer Cells in 3D Cultures to Kinase Inhibitors. *International Journal of Oncology* **2011**, *39* (3), 689–696. https://doi.org/10.3892/ijo.2011.1073.

(228) De Witt Hamer, P. C.; Van Tilborg, A. a. G.; Eijk, P. P.; Sminia, P.; Troost, D.; Van Noorden, C. J. F.; Ylstra, B.; Leenstra, S. The Genomic Profile of Human Malignant Glioma Is Altered Early in Primary Cell Culture and Preserved in Spheroids. *Oncogene* **2008**, *27* (14), 2091–2096. https://doi.org/10.1038/sj.onc.1210850.

(229) Qosa, H.; Avaritt, B. R.; Hartman, N. R.; Volpe, D. A. In Vitro UGT1A1 Inhibition by Tyrosine Kinase Inhibitors and Association with Drug-Induced Hyperbilirubinemia. *Cancer Chemother Pharmacol* **2018**, *82* (5), 795–802. https://doi.org/10.1007/s00280-018-3665-x.

(230) Sandström, N.; Carannante, V.; Olofsson, K.; Sandoz, P. A.; Moussaud-Lamodière, E. L.; Seashore-Ludlow, B.; Van Ooijen, H.; Verron, Q.; Frisk, T.; Takai, M.; Wiklund, M.; Östling, P.; Önfelt, B. Miniaturized and Multiplexed High-Content Screening of Drug and Immune Sensitivity in a Multichambered Microwell Chip. *Cell Reports Methods* **2022**, *2* (7), 100256. https://doi.org/10.1016/j.crmeth.2022.100256.

(231) Tchoryk, A.; Taresco, V.; Argent, R. H.; Ashford, M.; Gellert, P. R.; Stolnik, S.; Grabowska, A.; Garnett, M. C. Penetration and Uptake of Nanoparticles in 3D Tumor

Spheroids. *Bioconjugate Chem.* **2019**, *30* (5), 1371–1384. https://doi.org/10.1021/acs.bioconjchem.9b00136.

(232) Lukowski, J. K.; Hummon, A. B. Quantitative Evaluation of Liposomal Doxorubicin and Its Metabolites in Spheroids. *Anal Bioanal Chem* **2019**, *411* (27), 7087–7094. https://doi.org/10.1007/s00216-019-02084-7.

(233) Liu, X.; Flinders, C.; Mumenthaler, S. M.; Hummon, A. B. MALDI Mass Spectrometry Imaging for Evaluation of Therapeutics in Colorectal Tumor Organoids. *J Am Soc Mass Spectrom* **2018**, *29* (3), 516–526. https://doi.org/10.1007/s13361-017-1851-4.

(234) Wang, Y.; Hummon, A. B. MS Imaging of Multicellular Tumor Spheroids and Organoids as an Emerging Tool for Personalized Medicine and Drug Discovery. *J Biol Chem* **2021**, *297* (4), 101139. https://doi.org/10.1016/j.jbc.2021.101139.

(235) Liu, X.; Hummon, A. B. Mass Spectrometry Imaging of Therapeutics from Animal Models to Three-Dimensional Cell Cultures. *Anal. Chem.* **2015**, *87* (19), 9508–9519. https://doi.org/10.1021/acs.analchem.5b00419.

(236) Bartelink, I. H.; Jones, E. F.; Shahidi-Latham, S. K.; Lee, P. R. E.; Zheng, Y.; Vicini, P.; van ‘t Veer, L.; Wolf, D.; Iagaru, A.; Kroetz, D. L.; Prideaux, B.; Cilliers, C.; Thurber, G. M.; Wimana, Z.; Gebhart, G. Tumor Drug Penetration Measurements Could Be the Neglected Piece of the Personalized Cancer Treatment Puzzle. *Clin Pharmacol Ther* **2019**, *106* (1), 148–163. https://doi.org/10.1002/cpt.1211.

(237) Zhang, D.; Hop, C. E. C. A.; Patilea-Vrana, G.; Gampa, G.; Seneviratne, H. K.; Unadkat, J. D.; Kenny, J. R.; Nagapudi, K.; Di, L.; Zhou, L.; Zak, M.; Wright, M. R.; Bumpus, N. N.; Zang, R.; Liu, X.; Lai, Y.; Khojasteh, S. C. Drug Concentration Asymmetry in Tissues and Plasma for Small Molecule–Related Therapeutic Modalities. *Drug Metab Dispos* **2019**, *47* (10), 1122–1135. https://doi.org/10.1124/dmd.119.086744.

(238) Ray, S.; Das, S.; Suar, M. Molecular Mechanism of Drug Resistance. *Drug Resistance in Bacteria, Fungi, Malaria, and Cancer* **2017**, 47–110. https://doi.org/10.1007/978-3-319-48683-3_3.

(239) Wong, B. S.; Dunnington, E. L.; Wu, R.; Kim, J. I.; Hu, K.; Ro, T. H.; Fu, D. Facilitated Transport of EGFR Inhibitors Plays an Important Role in Their Cellular Uptake. *Anal. Chem.* **2024**, *96* (4), 1547–1555. https://doi.org/10.1021/acs.analchem.3c04242.

(240) Diaz, R.; Nguewa, P. A.; Parrondo, R.; Perez-Stable, C.; Manrique, I.; Redrado, M.; Catena, R.; Collantes, M.; Peñuelas, I.; Díaz-González, J. A.; Calvo, A. Antitumor and Antiangiogenic Effect of the Dual EGFR and HER-2 Tyrosine Kinase Inhibitor Lapatinib in a Lung Cancer Model. *BMC Cancer* **2010**, *10* (1), 188. https://doi.org/10.1186/1471-2407-10-188.

(241) Chu, X.; Korzekwa, K.; Elsby, R.; Fenner, K.; Galetin, A.; Lai, Y.; Matsson, P.; Moss, A.; Nagar, S.; Rosania, G. R.; Bai, J. P. F.; Polli, J. W.; Sugiyama, Y.; Brouwer, K. L. R.; International Transporter Consortium. Intracellular Drug Concentrations and Transporters: Measurement, Modeling, and Implications for the Liver. *Clin Pharmacol Ther* **2013**, *94* (1), 126–141. https://doi.org/10.1038/clpt.2013.78.

(242) Barisam, M.; Saidi, M. S.; Kashaninejad, N.; Nguyen, N.-T. Prediction of Necrotic Core and Hypoxic Zone of Multicellular Spheroids in a Microbioreactor with a U-Shaped Barrier. *Micromachines (Basel)* **2018**, *9* (3), 94. https://doi.org/10.3390/mi9030094.

(243) Carcereri de Prati, A.; Butturini, E.; Rigo, A.; Oppici, E.; Rossin, M.; Boriero, D.; Mariotto, S. Metastatic Breast Cancer Cells Enter Into Dormant State and Express Cancer

Stem Cells Phenotype Under Chronic Hypoxia. *Journal of Cellular Biochemistry* **2017**, *118* (10), 3237–3248. https://doi.org/10.1002/jcb.25972.

(244) Emami Nejad, A.; Najafgholian, S.; Rostami, A.; Sistani, A.; Shojaeifar, S.; Esparvarinha, M.; Nedaeinia, R.; Haghjooy Javanmard, S.; Taherian, M.; Ahmadlou, M.; Salehi, R.; Sadeghi, B.; Manian, M. The Role of Hypoxia in the Tumor Microenvironment and Development of Cancer Stem Cell: A Novel Approach to Developing Treatment. *Cancer Cell International* **2021**, *21* (1), 62. https://doi.org/10.1186/s12935-020-01719-5.

(245) Ahmed, M. A. M.; Nagelkerke, A. Current Developments in Modelling the Tumour Microenvironment *in Vitro*: Incorporation of Biochemical and Physical Gradients. *Organs-on-a-Chip* **2021**, *3*, 100012. https://doi.org/10.1016/j.ooc.2021.100012.

(246) Park, S.-Y.; Nam, J.-S. The Force Awakens: Metastatic Dormant Cancer Cells. *Exp Mol Med* **2020**, *52* (4), 569–581. https://doi.org/10.1038/s12276-020-0423-z.

(247) Lindell, E.; Zhong, L.; Zhang, X. Quiescent Cancer Cells-A Potential Therapeutic Target to Overcome Tumor Resistance and Relapse. *Int J Mol Sci* **2023**, *24* (4), 3762. https://doi.org/10.3390/ijms24043762.

(248) Hughes, C. S.; Postovit, L. M.; Lajoie, G. A. Matrigel: A Complex Protein Mixture Required for Optimal Growth of Cell Culture. *PROTEOMICS* **2010**, *10* (9), 1886–1890. https://doi.org/10.1002/pmic.200900758.

(249) Benton, G.; Arnaoutova, I.; George, J.; Kleinman, H. K.; Koblinski, J. Matrigel: From Discovery and ECM Mimicry to Assays and Models for Cancer Research. *Advanced Drug Delivery Reviews* **2014**, *79–80*, 3–18. https://doi.org/10.1016/j.addr.2014.06.005.

(250) Alberts, B.; Johnson, A.; Lewis, J.; Raff, M.; Roberts, K.; Walter, P. Cell-Cell Adhesion. In *Molecular Biology of the Cell. 4th edition*; Garland Science, 2002.

(251) Achilli, T.-M.; Meyer, J.; Morgan, J. R. Advances in the Formation, Use and Understanding of Multi-Cellular Spheroids. *Expert Opinion on Biological Therapy* **2012**, *12* (10), 1347–1360. https://doi.org/10.1517/14712598.2012.707181.

(252) Ryu, N.-E.; Lee, S.-H.; Park, H. Spheroid Culture System Methods and Applications for Mesenchymal Stem Cells. *Cells* **2019**, *8* (12), 1620. https://doi.org/10.3390/cells8121620.

(253) Cheng, B.; Crasta, K. Consequences of Mitotic Slippage for Antimicrotubule Drug Therapy. *Endocrine-Related Cancer* **2017**, *24* (9), T97–T106. https://doi.org/10.1530/ERC-17-0147.

(254) Xu, F. X.; Ioannou, G. N.; Lee, S. P.; Savard, C.; Horn, C. L.; Fu, D. Discrimination of Lipid Composition and Cellular Localization in Human Liver Tissues by Stimulated Raman Scattering Microscopy. *J Biomed Opt* **2024**, *29* (1), 016008. https://doi.org/10.1117/1.JBO.29.1.016008.

(255) Ioannou, G. N. The Role of Cholesterol in the Pathogenesis of NASH. *Trends Endocrinol Metab* **2016**, *27* (2), 84–95. https://doi.org/10.1016/j.tem.2015.11.008.

(256) Ioannou, G. N.; Subramanian, S.; Chait, A.; Haigh, W. G.; Yeh, M. M.; Farrell, G. C.; Lee, S. P.; Savard, C. Cholesterol Crystallization within Hepatocyte Lipid Droplets and Its Role in Murine NASH. *J Lipid Res* **2017**, *58* (6), 1067–1079. https://doi.org/10.1194/jlr.M072454.

(257) Liang, J. Q.; Teoh, N.; Xu, L.; Pok, S.; Li, X.; Chu, E. S. H.; Chiu, J.; Dong, L.; Arfianti, E.; Haigh, W. G.; Yeh, M. M.; Ioannou, G. N.; Sung, J. J. Y.; Farrell, G.; Yu, J. Dietary Cholesterol Promotes Steatohepatitis Related Hepatocellular Carcinoma through Dysregulated Metabolism and Calcium Signaling. *Nat Commun* **2018**, *9* (1), 4490. https://doi.org/10.1038/s41467-018-06931-6.

(258) Ioannou, G. N.; Landis, C. S.; Jin, G.-Y.; Haigh, W. G.; Farrell, G. C.; Kuver, R.; Lee, S. P.; Savard, C. Cholesterol Crystals in Hepatocyte Lipid Droplets Are Strongly Associated With Human Nonalcoholic Steatohepatitis. *Hepatology Communications* **2019**, *3* (6), 776–791. https://doi.org/10.1002/hep4.1348.

(259) Horn, C. L.; Morales, A. L.; Savard, C.; Farrell, G. C.; Ioannou, G. N. Role of Cholesterol-Associated Steatohepatitis in the Development of NASH. *Hepatol Commun* **2022**, *6* (1), 12–35. https://doi.org/10.1002/hep4.1801.

(260) Minamikawa, T.; Ichimura-Shimizu, M.; Takanari, H.; Morimoto, Y.; Shiomi, R.; Tanioka, H.; Hase, E.; Yasui, T.; Tsuneyama, K. Molecular Imaging Analysis of Microvesicular and Macrovesicular Lipid Droplets in Non-Alcoholic Fatty Liver Disease by Raman Microscopy. *Sci Rep* **2020**, *10* (1), 18548. https://doi.org/10.1038/s41598-020-75604-6.

(261) Takemura, M.; Mochizuki, K.; Harada, Y.; Okajima, A.; Hayakawa, M.; Dai, P.; Itoh, Y.; Tanaka, H. Label-Free Assessment of the Nascent State of Rat Non-Alcoholic Fatty Liver Disease Using Spontaneous Raman Microscopy. *Acta Histochemica Et Cytochemica* **2022**, *55* (2), 57–66. https://doi.org/10.1267/ahc.22-00013.

(262) Yan, J.; Yu, Y.; Kang, J. W.; Tam, Z. Y.; Xu, S.; Fong, E. L. S.; Singh, S. P.; Song, Z.; Tucker-Kellogg, L.; So, P. T. C.; Yu, H. Development of a Classification Model for Non-Alcoholic Steatohepatitis (NASH) Using Confocal Raman Micro-Spectroscopy. *Journal of Biophotonics* **2017**, *10* (12), 1703–1713. https://doi.org/10.1002/jbio.201600303.

(263) Helal, K. M.; Cahyadi, H.; Taylor, J. N.; Okajima, A.; Tabata, K.; Kumamoto, Y.; Mochizuki, K.; Itoh, Y.; Takamatsu, T.; Tanaka, H.; Fujita, K.; Komatsuzaki, T.; Harada, Y. Raman Imaging of Rat Nonalcoholic Fatty Liver Tissues Reveals Distinct Biomolecular States. *FEBS Letters* **2023**, *597* (11), 1517–1527. https://doi.org/10.1002/1873-3468.14600.

(264) Helal, K. M.; Taylor, J. N.; Cahyadi, H.; Okajima, A.; Tabata, K.; Itoh, Y.; Tanaka, H.; Fujita, K.; Harada, Y.; Komatsuzaki, T. Raman Spectroscopic Histology Using Machine Learning for Nonalcoholic Fatty Liver Disease. *FEBS Letters* **2019**, *593* (18), 2535–2544. https://doi.org/10.1002/1873-3468.13520.

(265) Ozeki, Y.; Dake, F.; Kajiyama, S.; Fukui, K.; Itoh, K. Analysis and Experimental Assessment of the Sensitivity of Stimulated Raman Scattering Microscopy. *Opt. Express, OE* **2009**, *17* (5), 3651–3658. https://doi.org/10.1364/OE.17.003651.

(266) Nandakumar, P.; Kovalev, A.; Volkmer, A. Vibrational Imaging Based on Stimulated Raman Scattering Microscopy. *New J. Phys.* **2009**, *11* (3), 033026. https://doi.org/10.1088/1367-2630/11/3/033026.

(267) Wang, P.; Liu, B.; Zhang, D.; Belew, M. Y.; Tissenbaum, H. A.; Cheng, J.-X. Imaging Lipid Metabolism in Live Caenorhabditis Elegans Using Fingerprint Vibrations. *Angew Chem Int Ed Engl* **2014**, *53* (44), 11787–11792. https://doi.org/10.1002/anie.201406029.

(268) Zhang, C.; Li, J.; Lan, L.; Cheng, J.-X. Quantification of Lipid Metabolism in Living Cells through the Dynamics of Lipid Droplets Measured by Stimulated Raman Scattering Imaging. *Anal. Chem.* **2017**, *89* (8), 4502–4507. https://doi.org/10.1021/acs.analchem.6b04699.

(269) Li, Y.; Bagheri, P.; Chang, P.; Zeng, A.; Hao, J.; Fung, A.; Wu, J. Y.; Shi, L. Direct Imaging of Lipid Metabolic Changes in Drosophila Ovary During Aging Using DO-SRS Microscopy. *Frontiers in Aging* **2022**, *2*.

(270) Hislop, E. W.; Tipping, W. J.; Faulds, K.; Graham, D. Label-Free Imaging of Lipid Droplets in Prostate Cells Using Stimulated Raman Scattering Microscopy and Multivariate

Analysis. *Anal. Chem.* **2022**, *94* (25), 8899–8908. https://doi.org/10.1021/acs.analchem.2c00236.

(271) Jia, H.; Liu, J.; Fang, T.; Zhou, Z.; Li, R.; Yin, W.; Qian, Y.; Wang, Q.; Zhou, W.; Liu, C.; Sun, D.; Chen, X.; Ouyang, Z.; Dong, J.; Wang, Y.; Yue, S. The Role of Altered Lipid Composition and Distribution in Liver Fibrosis Revealed by Multimodal Nonlinear Optical Microscopy. *Science Advances* **2023**, *9* (2), eabq2937. https://doi.org/10.1126/sciadv.abq2937.

(272) Kleiner, D. E.; Brunt, E. M.; Van Natta, M.; Behling, C.; Contos, M. J.; Cummings, O. W.; Ferrell, L. D.; Liu, Y.-C.; Torbenson, M. S.; Unalp-Arida, A.; Yeh, M.; McCullough, A. J.; Sanyal, A. J.; Nonalcoholic Steatohepatitis Clinical Research Network. Design and Validation of a Histological Scoring System for Nonalcoholic Fatty Liver Disease. *Hepatology* **2005**, *41* (6), 1313–1321. https://doi.org/10.1002/hep.20701.

(273) Chalasani, N.; Younossi, Z.; Lavine, J. E.; Charlton, M.; Cusi, K.; Rinella, M.; Harrison, S. A.; Brunt, E. M.; Sanyal, A. J. The Diagnosis and Management of Nonalcoholic Fatty Liver Disease: Practice Guidance from the American Association for the Study of Liver Diseases. *Hepatology* **2018**, *67* (1), 328–357. https://doi.org/10.1002/hep.29367.

(274) Angulo, P.; Kleiner, D. E.; Dam-Larsen, S.; Adams, L. A.; Bjornsson, E. S.; Charatcharoenwitthaya, P.; Mills, P. R.; Keach, J. C.; Lafferty, H. D.; Stahler, A.; Haflidadottir, S.; Bendtsen, F. Liver Fibrosis, but No Other Histologic Features, Is Associated With Long-Term Outcomes of Patients With Nonalcoholic Fatty Liver Disease. *Gastroenterology* **2015**, *149* (2), 389-397.e10. https://doi.org/10.1053/j.gastro.2015.04.043.

(275) Ekstedt, M.; Hagström, H.; Nasr, P.; Fredrikson, M.; Stål, P.; Kechagias, S.; Hultcrantz, R. Fibrosis Stage Is the Strongest Predictor for Disease-Specific Mortality in NAFLD after up to 33 Years of Follow-Up. *Hepatology* **2015**, *61* (5), 1547–1554. https://doi.org/10.1002/hep.27368.

(276) Kruth, H. S.; Fry, D. L. Histochemical Detection and Differentiation of Free and Esterified Cholesterol in Swine Atherosclerosis Using Filipin. *Experimental and Molecular Pathology* **1984**, *40* (3), 288–294. https://doi.org/10.1016/0014-4800(84)90046-7.

(277) Silveira, S. R.; Hadler, W. A. Histochemical Aspects Concerning the Synthesis and the Fate of Cholesterol into the Epidermis. *Acta Histochemica* **1984**, *74* (2), 145–155. https://doi.org/10.1016/S0065-1281(84)80001-X.

(278) Ioannou, G. N.; Haigh, W. G.; Thorning, D.; Savard, C. Hepatic Cholesterol Crystals and Crown-like Structures Distinguish NASH from Simple Steatosis. *J Lipid Res* **2013**, *54* (5), 1326–1334. https://doi.org/10.1194/jlr.M034876.

(279) Dumesnil, C.; Vanharanta, L.; Prasanna, X.; Omrane, M.; Carpentier, M.; Bhapkar, A.; Enkavi, G.; Salo, V. T.; Vattulainen, I.; Ikonen, E.; Thiam, A. R. Cholesterol Esters Form Supercooled Lipid Droplets Whose Nucleation Is Facilitated by Triacylglycerols. *Nat Commun* **2023**, *14* (1), 915. https://doi.org/10.1038/s41467-023-36375-6.

(280) Czamara, K.; Majzner, K.; Pacia, M. Z.; Kochan, K.; Kaczor, A.; Baranska, M. Raman Spectroscopy of Lipids: A Review. *Journal of Raman Spectroscopy* **2015**, *46* (1), 4–20. https://doi.org/10.1002/jrs.4607.

(281) Dixon, S. J.; Lemberg, K. M.; Lamprecht, M. R.; Skouta, R.; Zaitsev, E. M.; Gleason, C. E.; Patel, D. N.; Bauer, A. J.; Cantley, A. M.; Yang, W. S.; Morrison, B.; Stockwell, B. R. Ferroptosis: An Iron-Dependent Form of Nonapoptotic Cell Death. *Cell* **2012**, *149* (5), 1060–1072. https://doi.org/10.1016/j.cell.2012.03.042.

(282) Tang, D.; Chen, X.; Kang, R.; Kroemer, G. Ferroptosis: Molecular Mechanisms and Health Implications. *Cell Res* **2021**, *31* (2), 107–125. https://doi.org/10.1038/s41422-020-00441-1.

(283) Pu, F.; Chen, F.; Zhang, Z.; Shi, D.; Zhong, B.; Lv, X.; Tucker, A. B.; Fan, J.; Li, A. J.; Qin, K.; Hu, D.; Chen, C.; Wang, H.; He, F.; Ni, N.; Huang, L.; Liu, Q.; Wagstaff, W.; Luu, H. H.; Haydon, R. C.; Shen, L.; He, T.-C.; Liu, J.; Shao, Z. Ferroptosis as a Novel Form of Regulated Cell Death: Implications in the Pathogenesis, Oncometabolism and Treatment of Human Cancer. *Genes & Diseases* **2020**, *9* (2), 347. https://doi.org/10.1016/j.gendis.2020.11.019.

(284) Zhang, C.; Liu, X.; Jin, S.; Chen, Y.; Guo, R. Ferroptosis in Cancer Therapy: A Novel Approach to Reversing Drug Resistance. *Molecular Cancer* **2022**, *21* (1), 47. https://doi.org/10.1186/s12943-022-01530-y.

(285) Li, J.; Cao, F.; Yin, H.; Huang, Z.; Lin, Z.; Mao, N.; Sun, B.; Wang, G. Ferroptosis: Past, Present and Future. *Cell Death Dis* **2020**, *11* (2), 1–13. https://doi.org/10.1038/s41419-020-2298-2.

(286) Yu, Y.; Yan, Y.; Niu, F.; Wang, Y.; Chen, X.; Su, G.; Liu, Y.; Zhao, X.; Qian, L.; Liu, P.; Xiong, Y. Ferroptosis: A Cell Death Connecting Oxidative Stress, Inflammation and Cardiovascular Diseases. *Cell Death Discov.* **2021**, *7* (1), 1–10. https://doi.org/10.1038/s41420-021-00579-w.

(287) Yang, W. S.; SriRamaratnam, R.; Welsch, M. E.; Shimada, K.; Skouta, R.; Viswanathan, V. S.; Cheah, J. H.; Clemons, P. A.; Shamji, A. F.; Clish, C. B.; Brown, L. M.; Girotti, A. W.; Cornish, V. W.; Schreiber, S. L.; Stockwell, B. R. Regulation of Ferroptotic Cancer Cell Death by GPX4. *Cell* **2014**, *156* (1), 317–331. https://doi.org/10.1016/j.cell.2013.12.010.

(288) Yang, W. S.; Stockwell, B. R. Synthetic Lethal Screening Identifies Compounds Activating Iron-Dependent, Nonapoptotic Cell Death in Oncogenic-RAS-Harboring Cancer Cells. *Chemistry & Biology* **2008**, *15* (3), 234–245. https://doi.org/10.1016/j.chembiol.2008.02.010.

(289) Yin, H.; Xu, L.; Porter, N. A. Free Radical Lipid Peroxidation: Mechanisms and Analysis. *Chem. Rev.* **2011**, *111* (10), 5944–5972. https://doi.org/10.1021/cr200084z.

(290) Jahn, U.; Galano, J.-M.; Durand, T. Beyond Prostaglandins—Chemistry and Biology of Cyclic Oxygenated Metabolites Formed by Free-Radical Pathways from Polyunsaturated Fatty Acids. *Angewandte Chemie International Edition* **2008**, *47* (32), 5894–5955. https://doi.org/10.1002/anie.200705122.

(291) Niki, E. Lipid Peroxidation: Physiological Levels and Dual Biological Effects. *Free Radical Biology and Medicine* **2009**, *47* (5), 469–484. https://doi.org/10.1016/j.freeradbiomed.2009.05.032.

(292) Bochkov, V. N.; Oskolkova, O. V.; Birukov, K. G.; Levonen, A.-L.; Binder, C. J.; Stöckl, J. Generation and Biological Activities of Oxidized Phospholipids. *Antioxidants & Redox Signaling* **2010**, *12* (8), 1009. https://doi.org/10.1089/ars.2009.2597.

(293) Do, Q.; Xu, L. How Do Different Lipid Peroxidation Mechanisms Contribute to Ferroptosis? *Cell Reports Physical Science* **2023**, *4* (12), 101683. https://doi.org/10.1016/j.xcrp.2023.101683.

(294) Do, Q.; Zhang, R.; Hooper, G.; Xu, L. Differential Contributions of Distinct Free Radical Peroxidation Mechanisms to the Induction of Ferroptosis. *JACS Au* **2023**, *3* (4), 1100. https://doi.org/10.1021/jacsau.2c00681.

(295) Do, Q.; Lee, D. D.; Dinh, A. N.; Seguin, R. P.; Zhang, R.; Xu, L. Development and Application of a Peroxyl Radical Clock Approach for Measuring Both Hydrogen-Atom Transfer and Peroxyl Radical Addition Rate Constants. *J. Org. Chem.* **2021**, *86* (1), 153–168. https://doi.org/10.1021/acs.joc.0c01920.

(296) Conrad, M.; Kagan, V. E.; Bayir, H.; Pagnussat, G. C.; Head, B.; Traber, M. G.; Stockwell, B. R. Regulation of Lipid Peroxidation and Ferroptosis in Diverse Species. *Genes & Development* **2018**, *32* (9–10), 602. https://doi.org/10.1101/gad.314674.118.

(297) Magtanong, L.; Ko, P.-J.; To, M.; Cao, J. Y.; Forcina, G. C.; Tarangelo, A.; Ward, C. C.; Cho, K.; Patti, G. J.; Nomura, D. K.; Olzmann, J. A.; Dixon, S. J. Exogenous Monounsaturated Fatty Acids Promote a Ferroptosis-Resistant Cell State. *Cell Chemical Biology* **2019**, *26* (3), 420-432.e9. https://doi.org/10.1016/j.chembiol.2018.11.016.

(298) Liang, D.; Minikes, A. M.; Jiang, X. Ferroptosis at the Intersection of Lipid Metabolism and Cellular Signaling. *Molecular cell* **2022**, *82* (12), 2215. https://doi.org/10.1016/j.molcel.2022.03.022.

(299) Kodali, S. T.; Kauffman, P.; Kotha, S. R.; Yenigalla, A.; Veeraraghavan, R.; Pannu, S. R.; Hund, T. J.; Satoskar, A. R.; McDaniel, J. C.; Maddipati, R. K.; Parinandi, N. L. Oxidative Lipidomics: Analysis of Oxidized Lipids and Lipid Peroxidation in Biological Systems with Relevance to Health and Disease. In *Measuring Oxidants and Oxidative Stress in Biological Systems*; Berliner, L. J., Parinandi, N. L., Eds.; Springer International Publishing: Cham, 2020; pp 61–92. https://doi.org/10.1007/978-3-030-47318-1_5.

(300) Su, D.; Wang, X.; Zhang, W.; Li, P.; Tang, B. Fluorescence Imaging for Visualizing the Bioactive Molecules of Lipid Peroxidation within Biological Systems. *TrAC Trends in Analytical Chemistry* **2022**, *146*, 116484. https://doi.org/10.1016/j.trac.2021.116484.

(301) von Krusenstiern, A. N.; Robson, R. N.; Qian, N.; Qiu, B.; Hu, F.; Reznik, E.; Smith, N.; Zandkarimi, F.; Estes, V. M.; Dupont, M.; Hirschhorn, T.; Shchepinov, M. S.; Min, W.; Woerpel, K. A.; Stockwell, B. R. Identification of Essential Sites of Lipid Peroxidation in Ferroptosis. *Nat Chem Biol* **2023**, 1–12. https://doi.org/10.1038/s41589-022-01249-3.

(302) Xie, Y.; Hou, W.; Song, X.; Yu, Y.; Huang, J.; Sun, X.; Kang, R.; Tang, D. Ferroptosis: Process and Function. *Cell Death and Differentiation* **2016**, *23* (3), 369. https://doi.org/10.1038/cdd.2015.158.

(303) Bai, Y.; Meng, L.; Han, L.; Jia, Y.; Zhao, Y.; Gao, H.; Kang, R.; Wang, X.; Tang, D.; Dai, E. Lipid Storage and Lipophagy Regulates Ferroptosis. *Biochemical and Biophysical Research Communications* **2019**, *508* (4), 997–1003. https://doi.org/10.1016/j.bbrc.2018.12.039.

(304) Kim, J.; Koo, B.-K.; Knoblich, J. A. Human Organoids: Model Systems for Human Biology and Medicine. *Nat Rev Mol Cell Biol* **2020**, *21* (10), 571–584. https://doi.org/10.1038/s41580-020-0259-3.

(305) Thorel, L.; Perréard, M.; Florent, R.; Divoux, J.; Coffy, S.; Vincent, A.; Gaggioli, C.; Guasch, G.; Gidrol, X.; Weiswald, L.-B.; Poulain, L. Patient-Derived Tumor Organoids: A New Avenue for Preclinical Research and Precision Medicine in Oncology. *Exp Mol Med* **2024**, *56* (7), 1531–1551. https://doi.org/10.1038/s12276-024-01272-5.

(306) Du, J.; Su, Y.; Qian, C.; Yuan, D.; Miao, K.; Lee, D.; Ng, A. H. C.; Wijker, R. S.; Ribas, A.; Levine, R. D.; Heath, J. R.; Wei, L. Raman-Guided Subcellular Pharmaco-Metabolomics for Metastatic Melanoma Cells. *Nat Commun* **2020**, *11* (1), 4830. https://doi.org/10.1038/s41467-020-18376-x.

(307) Tan, Y.; Lin, H.; Cheng, J.-X. Profiling Single Cancer Cell Metabolism via High-Content SRS Imaging with Chemical Sparsity. *Science Advances* **2023**, *9* (33), eadg6061. https://doi.org/10.1126/sciadv.adg6061.

APPENDIX A

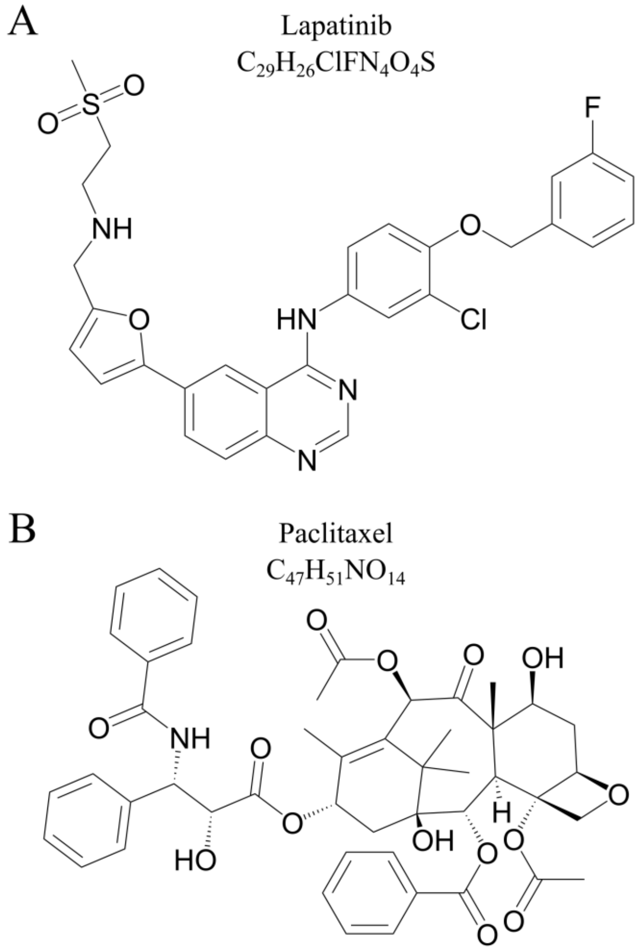

Lapatinib
$C_{29}H_{26}ClFN_4O_4S$

Paclitaxel
$C_{47}H_{51}NO_{14}$

Figure A.1. Molecular formulas and structures of (A) lapatinib and (B) paclitaxel, drugs used in this study.

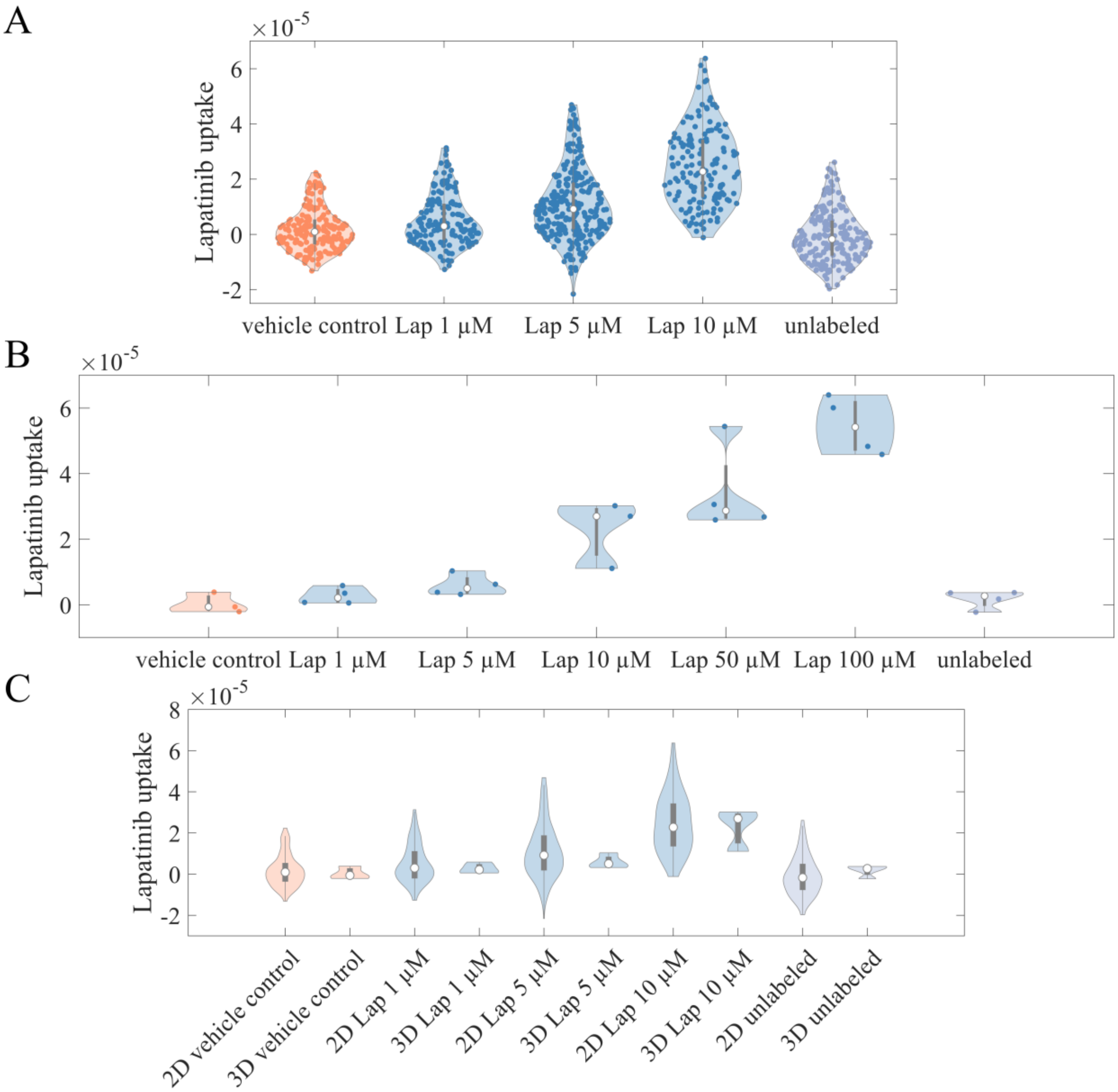

Figure A.2. Intracellular drug uptake measurements with normalization using the C–H peak intensity at 2930 cm^{-1}. (A) 2D A549 cells treated with lapatinib (Lap) of 1–10 µM. (B) 3D A549 spheroids treated with Lap of 1–100 µM. (C) Comparison of 2D and 3D cellular drug uptake.

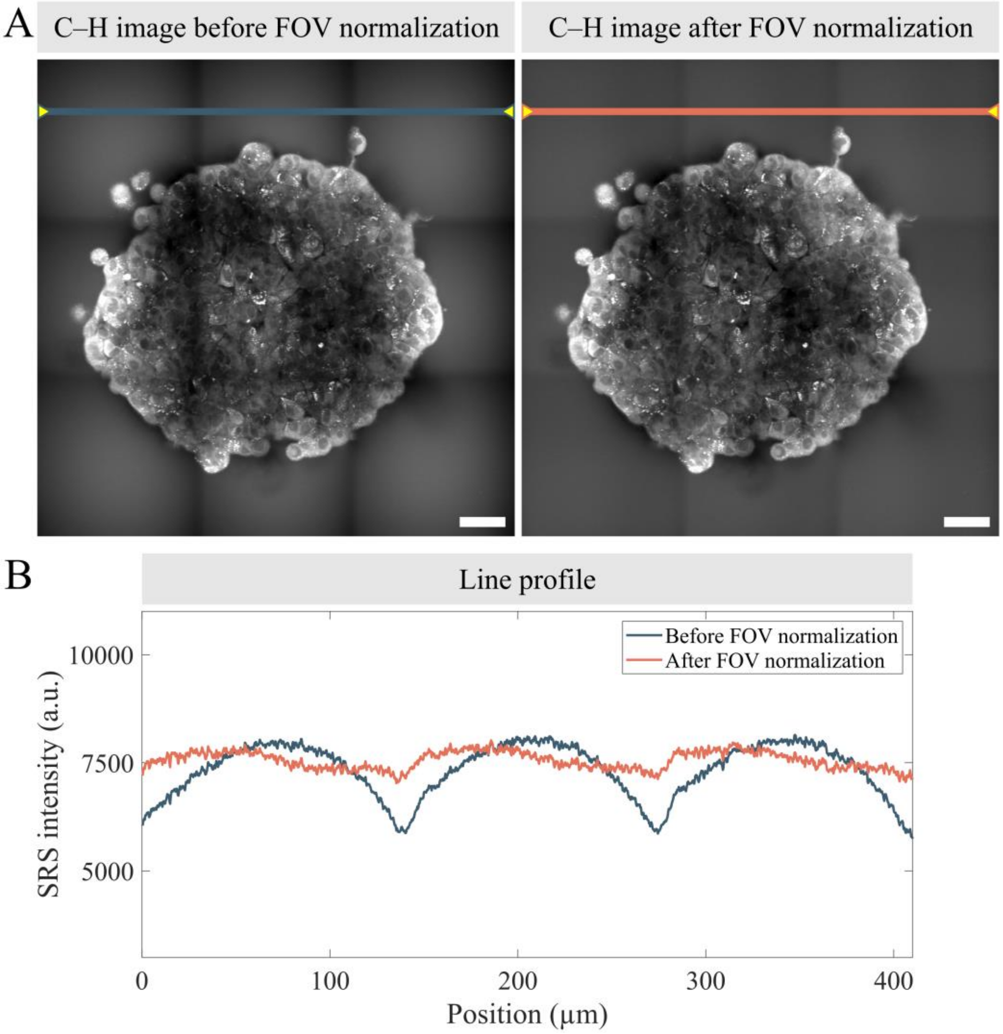

Figure A.3. Field-of-view (FOV) normalization for spheroid imaging. The natural curvature of each FOV can result in severe stitching artifacts (left in A). We generated FOV normalization masks using cell-free regions and normalized them to have an intensity ranging from 0 to 1. Each SRS image was divided by the FOV mask before stitching. The stitching artifacts were significantly reduced (right in A). (B) Signal intensity profiles before and after FOV normalization. Scale bars: 40 µm.

APPENDIX B

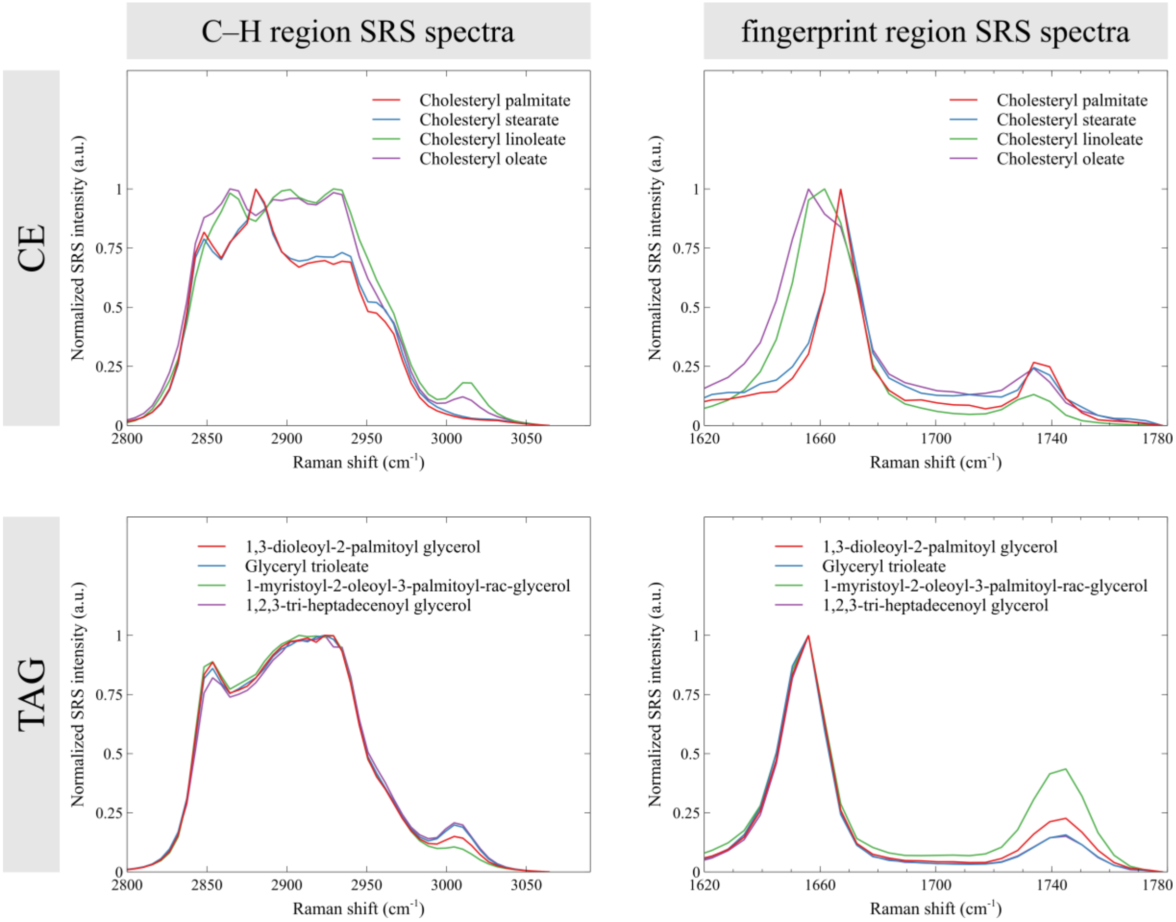

Figure B.1. C–H region and fingerprint region SRS spectra of cholesteryl esters (CE) and triglycerides (TAG) of different saturation levels.

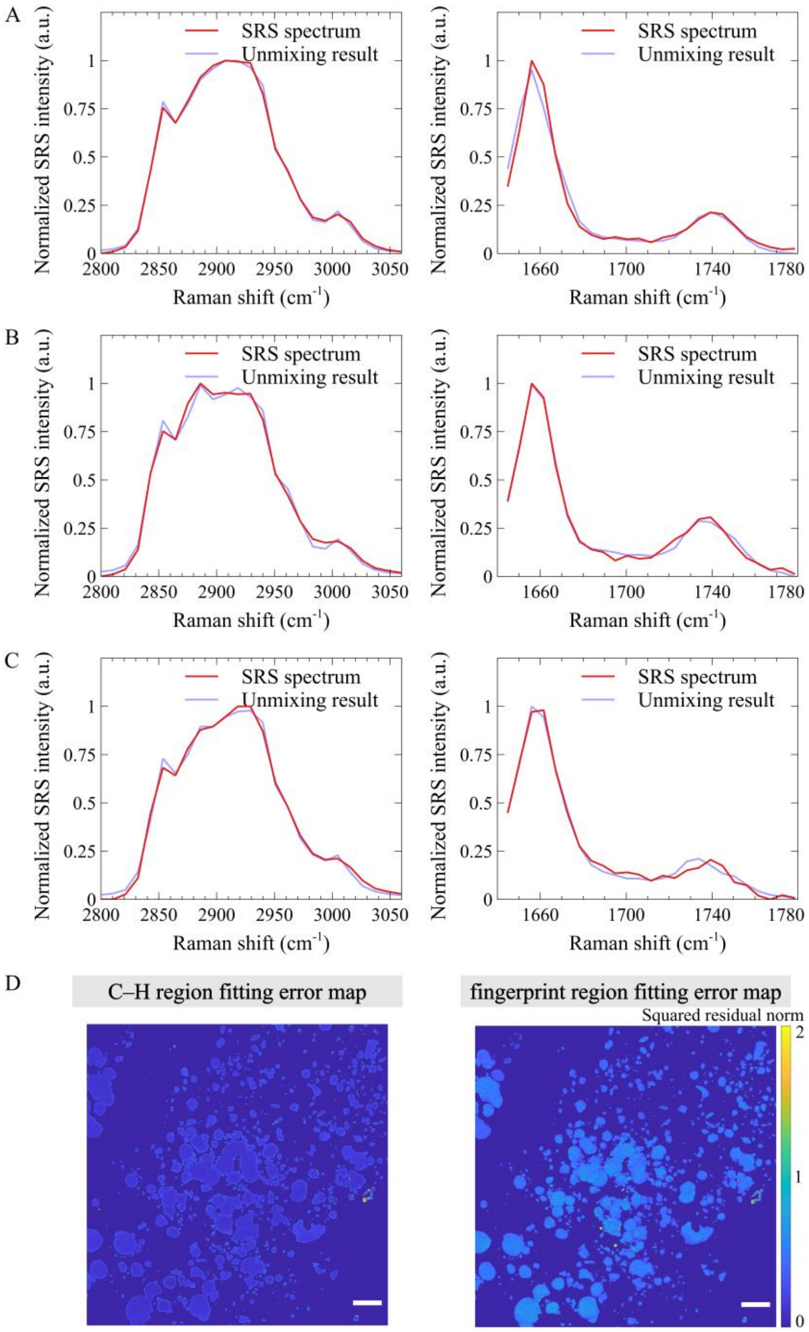

Figure B. 2. Representative pixel SRS spectra and corresponding spectral unmixing algorithm fitting results (A-C) and fitting error maps (D) of a representative liver tissue section from a patient with NASH. The corresponding free cholesterol, saturated CE, unsaturated CE, and total TAG percentage maps are shown in Figure 5.3F - I. (A) SRS spectra of a pixel selected from a TAG-dominated region. (B) SRS spectra of a pixel selected from a saturated CE-dominated region. (C) SRS spectra of a pixel selected from a high cholesterol percentage region. The intensity of each pixel in the fitting error maps (D) represents the square of the fitting residual norm. A lower square residual norm value means more accurate fitting. Scale bar: 50 µm.

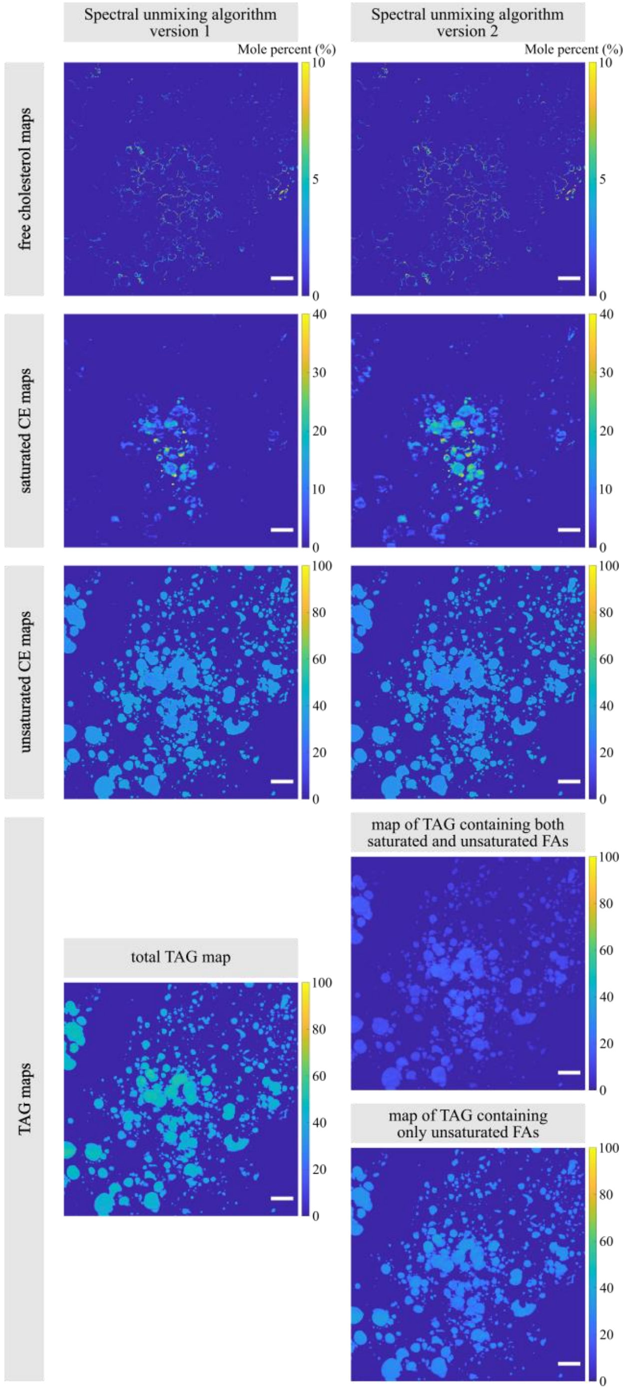

Figure B.3. Comparison of two spectral unmixing algorithm versions with a representative liver tissue section from a patient with NASH. Spectral unmixing algorithm version 1: SRS spectra of free cholesterol, saturated CE, unsaturated CE, and average TAG (Figure 5.2) were used for spectral unmixing. Spectral unmixing algorithm version 2: spectra of free cholesterol, saturated

CE, unsaturated CE, and two TAG of different unsaturation levels (Figure B.1, 1-Myristoyl-2-Oleoyl-3-Palmitoyl-rac-glycerol as TAG containing both saturated and unsaturated FAs, and 1,2,3-Tri-Heptadecenoyl Glycerol as TAG containing only unsaturated FAs) were used for spectral unmixing. Scale bar: 50 µm.

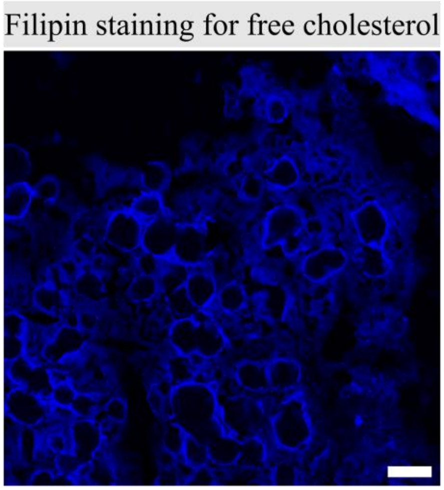

Figure B.4. Filipin staining for free cholesterols in the same liver tissue (different section) as Figure 5.3 from a patient with NASH. Free cholesterol tends to localize around the outer periphery of lipid droplets. Scale bar: 50 µm.

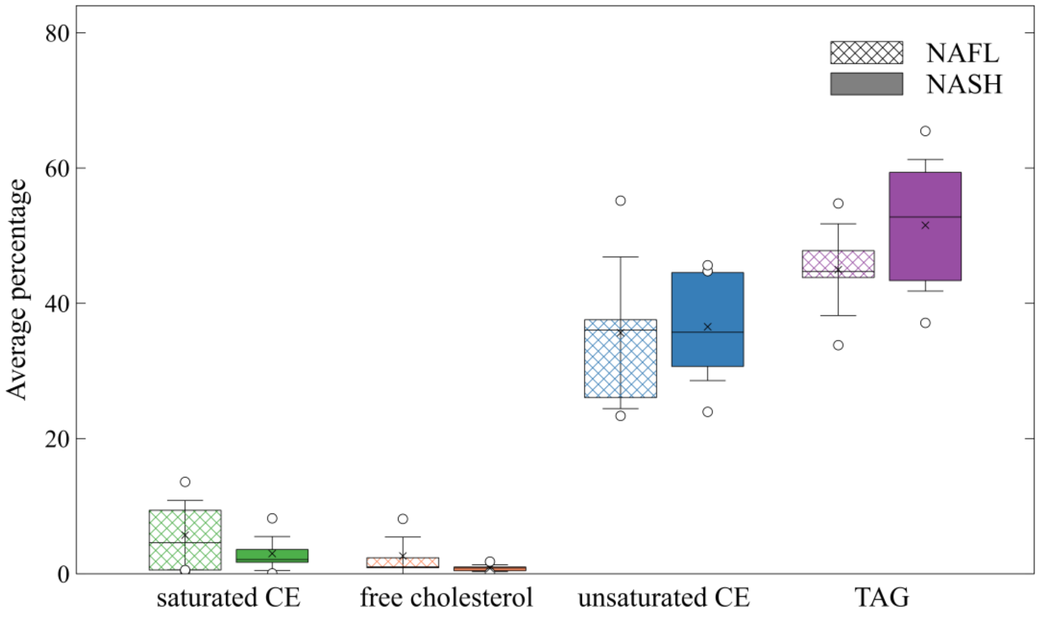

Figure B.5. Average percentages of different lipid species in the imaged regions of liver tissue sections from patients diagnosed with NAFL versus NASH.

Group	**CE**	**Free Cholesterol**	**TAG**	**DAG**	**FFA**
	nmol/ mg liver	nmol/ mg liver	nmol/ mg liver	nmol/ mg liver	nmol/ mg liver
NAFL					
Average	2065.303	1.297	54328.152	5679.604	22542.003
St Dev	1108.389	0.810	38711.715	3727.636	8573.912
% of total lipids	1.847	0.001	48.581	5.079	20.157
NASH					
Average	3040.530	1.179	92521.356	9542.998	31285.772
St Dev	1753.570	0.578	49763.588	5249.500	14950.443
% of total lipids	1.831	0.0007	55.708	5.746	18.838
Ratio of NASH/NAFL	1.472	0.909	1.703	1.680	1.388
t-test	0.104	0.663	0.035	0.039	0.084

Table B.1. Average NAFL and NASH human liver biopsy hepatic lipid composition measured by lipidomics analysis.

Statistical analysis was performed using the Student t-test. CE: cholesteryl ester; TAG: triglyceride; DAG: diglyceride; FFA: free fatty acid.

Fiona Xi Xu

University of Washington – Seattle, WA – 98195
☎ (508) 369-2011 • ✉ fionaxixu@gmail.edu

Education

University of Washington, Seattle, WA **2019 — 2024**
Doctor of Philosophy in Chemistry GPA: 3.88/4.0
Research Advisor: Dr. Dan Fu

- Honor: Excellence in Chemistry Fellowship (2019).

Wheaton College, Norton, MA **2014 — 2018**
Bachelor of Arts in Chemistry, Bachelor of Arts in Mathematics GPA: 3.97/4.0

- Honors: Summa Cum Laude, Phi Beta Kappa Society (2017 — present), The Undergraduate Award in Analytical Chemistry (2017), The A. Howard Meneely Prize (2018), Fred Kollett Prize in Mathematics & Computer Science (2018), Villars Prize in Science (2018), Madeleine F. Clark Wallace Mathematics Prize (2018), Dean's List (2014 — 2018).

Research Experience

University of Washington, Department of Chemistry, Seattle, WA **2019 — 2024**
Graduate Research Assistant

- Conducted various biomedical research with precision chemical imaging techniques, including dual-band hyperspectral stimulated Raman scattering (SRS), second-harmonic generation (SHG), multiphoton fluorescence, and phosphorescence lifetime imaging microscopy (PLIM).
- Constructed and maintained optical parametric oscillators (OPOs), ultrafast laser system, SRS, and quantitative phase microscopy system.
- Developed and integrated SRS-based techniques for 2D and 3D cell drug uptake and growth response measurements.
- Investigated protein and lipid metabolism changes in cells and tissues during various disease and treatments.

Wheaton College, Department of Chemistry, Norton, MA **2017 — 2018**
Laboratory Researcher

- Co-designed and executed experiments to investigate the impact of inundation on methylmercury production in leaf litter.
- Utilized distillations, acid digestions, and gas chromatography for methylmercury and total mercury concentration detection in samples.

Wheaton College, Department of Mathematics, Norton, MA **2017 — 2018**

- Completed a thesis on Perfect Colorings of a Design With 2-Dimensional Euclidean Crystallographic Symmetry Group.

Professional Experience

Wheaton College Chemistry Department, Norton, MA **2018 — 2019**
Teaching Assistant

- Developed new lab experiments including air-free Schlenk techniques and electrochemistry for Advanced Inorganic Chemistry labs.
- Guided students in chemical compound synthesis and analysis.

Xian Janssen Pharmaceutical Ltd., Beijing, China **Summer 2016**
OTC Medical Education Department Intern

- Designed questionnaires and interviewed physicians about their prescribing habits for common illnesses.
- Assisted in the planning and hosting Respiratory Medicine Conferences.

Technical Skills

- **Software Skills**: MATLAB, LabVIEW, Python, Fusion 360, ImageJ, Cellpose, Inkscape, Zotero, LaTeX, Word, Excel, PowerPoint, Mathematica.
- **Applied Research Skills**: Spectral focusing SRS microscopy, Raman spectroscopy, quantitative phase microscopy, multiphoton fluorescence, PLIM, SHG, phase-contrast, and brightfield microscopy, optical coherence microscopy (OCM), optical parametric oscillator, 2D and 3D cell culture techniques, MTT assay.

Conference Presentations

- **ACS Spring**, *Quantification of cell growth rates by ratiometric stimulated Raman scattering microscopy*, Indianapolis, IN, March 2023.
- **SPIE Photonics West**, *Characterization of lipid composition and localization at different stages of nonalcoholic fatty liver disease using stimulated Raman scattering microscopy*, San Francisco, CA, January 2023.
- **SPIE Photonics West**, *High-throughput, single-cell drug response measurement using quantitative phase microscopy*, poster presentation, San Francisco, CA, January 2023.
- **Summit for Women in STEM**, *Perfect Colorings of Polygons*, Norton, MA, March 2018.

Peer-Reviewed Publications

- **Xu, F. X.**; Sun, R.; Owens, R.; Hu, K.; Fu, D. Assessing Drug Uptake and Response Differences in 2D and 3D Cellular Environments Using Stimulated Raman Scattering Microscopy. *Anal. Chem.* in press. 2024, 96 (36), 14480–14489.
- **Xu, F. X.**; Ioannou, G. N.; Lee, S. P.; Savard, C.; Horn, C. L.; Fu, D. Discrimination of lipid composition and cellular localization in human liver tissues by stimulated Raman scattering microscopy. *J. Biomed. Opt.* 2024, 29 (1), 016008.
- **Xu, F. X.**; Wu, R.; Hu, K.; Fu, D. Measuring drug response with single-cell growth rate quantification. *Anal. Chem.* 2023, 95 (49), 18114–18121.
- **Xu, F. X.**; Rathbone, E. G.; Fu, D. Simultaneous Dual-Band Hyperspectral Stimulated Raman Scattering Microscopy with Femtosecond Optical Parametric Oscillators. *J. Phys. Chem. B* 2023, 127 (10), 2187–2197.
- Figueroa, B.; **Xu, F. X.**; Hu, R.; Men, S.; Fu, D. Quantitative Imaging of Intracellular Density with Ratiometric Stimulated Raman Scattering Microscopy. *J. Phys. Chem. B* 2022, 126 (39), 7595–7603.